Nano-Engineering the Boiling Surface for Optimal Heat Transfer Rate and Critical Heat Flux

By

Bren Andrew Phillips

B.S., Nuclear Engineering
University of Missouri-Rolla, 2005

SUBMITTED TO THE DEPARTMENT OF NUCLEAR SCIENCE AND ENGINEERING IN PARTIAL FULFILLMENT OF THE REQUIREMENTS FOR THE DEGREES OF

MASTER OF SCIENCE IN NUCLEAR SCIENCE AND ENGINEERING

AT THE

MASSACHUSETTS INSTITUTE OF TECHNOLOGY

February 2011

Signature of Author:_____
Department of Nuclear Science and Engineering
January 14, 2011

Certified by:_____
Jacopo Buongiorno
Associate Professor of Nuclear Science and Engineering
Thesis Supervisor

Certified by:_____
Michael Rubner
Professor/Director of Center for Materials Science and Engineering
Thesis Supervisor

Certified by:_____
Robert Cohen
St. Laurent Professor of Chemical Engineering
Thesis Supervisor

Certified by:_____
Lin-Wen Hu
Associate Director, MIT Nuclear Reactor Laboratory
Thesis Supervisor

Certified by:_____
Tom McKrell
Research Scientist for Nuclear Science and Engineering
Thesis Supervisor

Accepted by:_____
Mujid Kazimi
Professor of Nuclear Science and Engineering
Chair, Department Committee on Graduate Students

Nano-Engineering the Boiling Surface for Optimal Heat Transfer Rate and Critical Heat Flux

by

Bren Andrew Phillips

Submitted to the Department of Nuclear Science and Engineering on January 14, 2011 in partial fulfillment for the requirements of the degrees of

MASTER OF SCIENCE
in NUCLEAR SCIENCE AND ENGINEERING

ABSTRACT

The effects on pool boiling characteristics such as critical heat flux and the heat transfer coefficient of different surface characteristics such as surface wettability, roughness, morphology, and porosity are not well understood. Layer-by-layer nanoparticle coatings were used to modify the surface of a sapphire heater to control the surface roughness, the layer thickness, and the surface chemistry. The surface was then tested in a water boiling test at atmospheric pressure while imaging the surface with high speed infrared thermography yielding a 2D time dependent temperature profile. The critical heat flux and heat transfer coefficient were enhanced by over 100% by optimizing the surface parameters. It was found that particle size of the nanoparticles in coating, the coating thickness, and the wettability of the surface have a large impact on CHF and the heat transfer coefficient.

Surfaces were also patterned with hydrophobic "islands" within a hydrophilic "sea" by coupling the Layer-by-layer nanoparticle coatings with an ultraviolet ozone technique that patterned the wettability of the surface. The patterning was an attempt to increase the nucleation site density with hydrophobic dots while still maintaining a large hydrophilic region to allow for rewetting of the surface during the ebullition cycle and thus maintaining a high critical heat flux. The patterned surfaces exhibited similar critical heat fluxes and heat transfer coefficients to the surfaces that were only modified with layer-by-layer nanoparticle coatings. However, the patterned surfaces also exhibited highly preferential nucleation from the hydrophobic regions demonstrating an ability to control the nucleation site layout of a surface and opening an avenue for further study.

THESIS SUPERVISOR: Jacopo Buongiorno, Ph.D.
TITLE: Associate Professor of Nuclear Science and Engineering

THESIS SUPERVISOR: Michael Rubner, Ph.D.
TITLE: Professor/Director of Center for Materials Science and Engineering

THESIS SUPERVISOR: Robert Cohen, Ph.D.
TITLE: St. Laurent Professor of Chemical Engineering

THESIS SUPERVISOR: Lin-Wen Hu, Ph.D., PE
TITLE: Associate Director and Principal Research Scientist, MIT Nuclear Reactor Laboratory

THESIS SUPERVISOR: Tom McKrell, Ph.D.
TITLE: Research Scientist for Nuclear Science and Engineering

ACKNOWLEDGEMENTS

I first of all want to thank my thesis supervisor Professor Jacopo Buongiorno for all of his support, help, and patience throughout this project. Also, I would like to extend thanks Dr. Lin-Wen Hu for all of her input and help with the project.

I would like to extend my personal gratitude to Dr. Tom McKrell, who spent hours helping me with a myriad of experimental details. I also want to thank Professors Michael Rubner and Robert Cohen for their expertise and use of their facilities for the fabrication of the multilayers. I also want to extend my gratitude to Erik Williamson for all of his help on teaching me how to make the multilayers and his suggestions on patterning the surface. My thanks are also extended to professor Vladimir Bulovic for him allowing me to use his UV ozone chamber. I owe many thanks to the research group who provided me with help, feedback, and suggestions including Eric Forrest, Bao Truong, Vivek Sharma, Greg Dewitt, and others. I want to acknowledge Dr. Craig Gerardi for all of his previous IR work and thank him for getting me started with this work.

I want to acknowledge the National Science Foundation for financially supporting me through their graduate research fellowship program. Also, thank you to the King Abdulaziz City of Science and Technology (KACST) for their financial support.

I owe a great thanks to Schlumberger-Doll Research Center and Albert Perez for kindly letting me use their confocal microscope.

My friends and family have put up with a lot during my time at MIT and I want to thank them for their support and guidance.

I want to wish the best of luck to Harry O'Hanley and the others that continue this work.

Table of Contents

List of Figures

List of Tables

1 Introduction

1.1 Motivation

Nucleate boiling is an important heat transfer mechanism for many engineering applications. However, as the heat flux is increased eventually a critical heat flux (CHF) is reached where the boiling mechanism changes from nucleate boiling to film boiling; known as the boiling crisis. Film boiling has drastically lower heat transfer characteristics than nucleate boiling. Therefore, when the transition occurs in a heat-flux-controlled situation usually the heat transfer surface cannot handle the accompanying dramatic increase in temperatures and it leads to the destruction of the surface, which is referred to as burnout [1].

One method of increasing the CHF and, to a lesser extent, the heat transfer coefficient of fluids is to seed fluids with low concentrations of small particles on the order of nanometers and create a suspension known as a nanofluid. Using nanofluids experimentalists have been able to enhance the CHF by up to 200% with low concentrations (~1% by volume or less). During nucleate boiling the nanoparticles deposit on the heat transfer surface and make the surface more hydrophilic [2]. However, the deposition is a random process since it is driven by boiling and the question exists of whether creating a surface with specific controlled characteristics could achieve an even higher enhancement in boiling heat transfer.

1.2 Objective

The objective of this research project is to gain a basic understanding of how surface parameters such as wettability, roughness, and nanoparticle layer thickness affect boiling heat transfer and CHF. This information will then be utilized to attempt to gain a dramatic increase in both critical heat flux and heat transfer coefficient during pool boiling. A surface will be

engineered to have the correct mix of hydrophobic and hydrophilic surface characteristics on the appropriate size scale to create the ideal mix of nucleation sites (which govern nucleate boiling) and surface wettability (which strongly affects critical heat flux).

The resulting surface technology could then be applied to new heat transfer systems of lower mass and cost. These systems would include electronic cooling systems, refrigeration systems, nuclear and chemical reactors. In light water nuclear reactors CHF is often the limiting design criteria and a higher critical heat flux leads to a higher power density that reduces the size and/or cost of a reactor.

2 Boiling Background Information

2.1 Traditional Boiling Nucleation Theory

Vapor formation usually begins at a nucleation site that reduces the free energy required to create a stable vapor bubble. This site is usually a small indentation on the heat transfer surface that contains a small gas pocket as shown in Figure 2-1. The site will grow a vapor bubble that then detaches from the surface and carries away a large quantity of heat through agitation, evaporation, and removal of the thermal boundary layer. When nucleation occurs heterogeneously in this manner only a few degrees of superheat are required for the onset of boiling (ONB). These nucleation sites and their number are related to the heat transfer coefficient and indirectly to the critical heat flux [1].

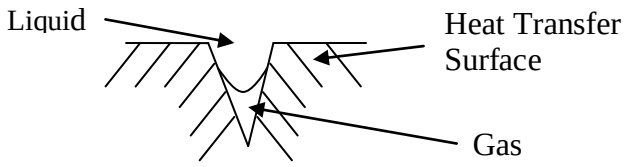

Figure 2-1: Active nucleation site with trapped gas.

The surface wettability determines how much contact the fluid has with the heat transfer surface. Wettability is measured by the contact angle θ and is visualized in Figure 2-2, and is the angle that a drop of liquid makes with the surface [2].

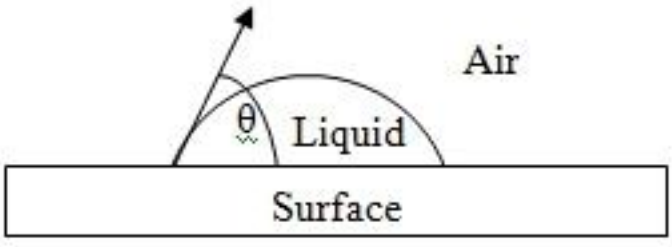

Figure 2-2: Schematic of a Liquid Droplet on a flat Solid Surface.

A lower contact angle means a higher surface wettability, which in general increases the critical heat flux. However, a high surface wettability also can have the effect of deactivating nucleation sites and thereby decreasing the boiling heat transfer coefficient [1][2].

Heterogeneous nucleation can also occur at a smooth interface, and the energy required is a function of the contact angle of the surface. The rate of vapor embryo formation on a smooth surface is given by the following equation [3].

$$J = \frac{\rho_{N,l}^{2/3}(1+\cos\theta)}{2F}\left(\frac{3F\sigma}{\pi m}\right)^{1/2}\exp\left(\frac{-16\pi F\sigma^3}{3k_B T_l\left[\eta P_{sat}(T_l)-P_l\right]^2}\right) \qquad \textbf{Eq. 2-1}$$

where

$$F = F(\theta) = \frac{1}{2}+\frac{3}{4}\cos(\theta)-\frac{1}{4}\cos^3(\theta) \qquad \textbf{Eq. 2-2}$$

$$\eta = \exp\left(\frac{\upsilon_l\left[P_l - P_{sat}(T_l)\right]}{RT_l}\right) \qquad \textbf{Eq. 2-3}$$

J is the rate of embryo formation (m^{-2}-s^{-1}), F is a dimensionless parameter that is a function of contact angle, $\rho_{N,l}$ is the atom density of the fluid (atoms/m^3), θ is the static contact angle of the fluid on the surface, σ is the surface tension of the liquid vapor interface (N/m), m is the molecular mass of the fluid (kg/mol), k_B is the Boltzmann constant (J/K), T_l is the liquid temperature (K), P_{sat} is the saturation pressure at T_l (Pa), P_l is the pressure (Pa), υ_l is the liquid specific volume (m^3/kg), and R is the gas constant (J/(K-mol)).

Nucleation can also occur homogenously in a medium, that is, in the absence of a solid surface. Since in this situation there is no nucleation site such as shown in Figure 2-1, the free

energy to form the new phase is much larger, and therefore the superheat of the fluid has to be much higher.

Figure 2-3 shows a plot of Eq. 2-1 for various contact angles for water at atmospheric pressure. Also, the temperature for homogenous nucleation is shown as a vertical line for the case where there is no nucleation surface. This shows that the superheat required for nucleation at a smooth surface is expected to be high (i.e. >60°C). The point at which the embryo formation rate is high enough to be considered bubble nucleation is somewhat subjective. However, a couple of simple calculations can put the embryo formation rates into perspective. For example, if a $1cm^2$ has a single bubble forming every 10 seconds yields an embryo formation rate of 10^3 $(m^2\text{-}s)^{-1}$, practically this is a very slow nucleation rate at the very cusp at the ONB where the boiling would not have a large influence on the heat transfer coefficient. A bubble forming every 10^{-4} seconds in $1cm^2$, which would represent 4 sites nucleating at 10Hz that is clearly a boiling situation, would be an embryo formation rate of 10^8 $(m^2\text{-}s)^{-1}$. Examining the two embryo formation rates on Figure 2-3, it can be seen that the difference in these rates results in a change of less than 5°C because of the steep slopes of the embryo formation rate curves. Therefore, regardless of the exact choice for the cutoff criteria used for bubble nucleation, the temperature at which it occurs is bounded by less than 5°C.

Traditionally, the nucleation sites shown in Figure 2-1 are on the order of 0.1-10 microns, act as storage volumes for gas, and give a large reduction in free energy for bubble formation [4]. The Young-Laplace equation relates a critical radius to the temperature of the fluid by a balance of forces on a bubble and is shown in Eq. 2-4 [3].

$$r^* = \frac{2\sigma}{P_v - P_l} \qquad \textbf{Eq. 2-4}$$

Where r^* is the critical radius (m), σ is the surface tension (N/m) and P_v is the saturation pressure at the wall temperature (Pa), and P_l is the saturation pressure of the bulk fluid (Pa). Eq. 2-4 is plotted in Figure 2-4.

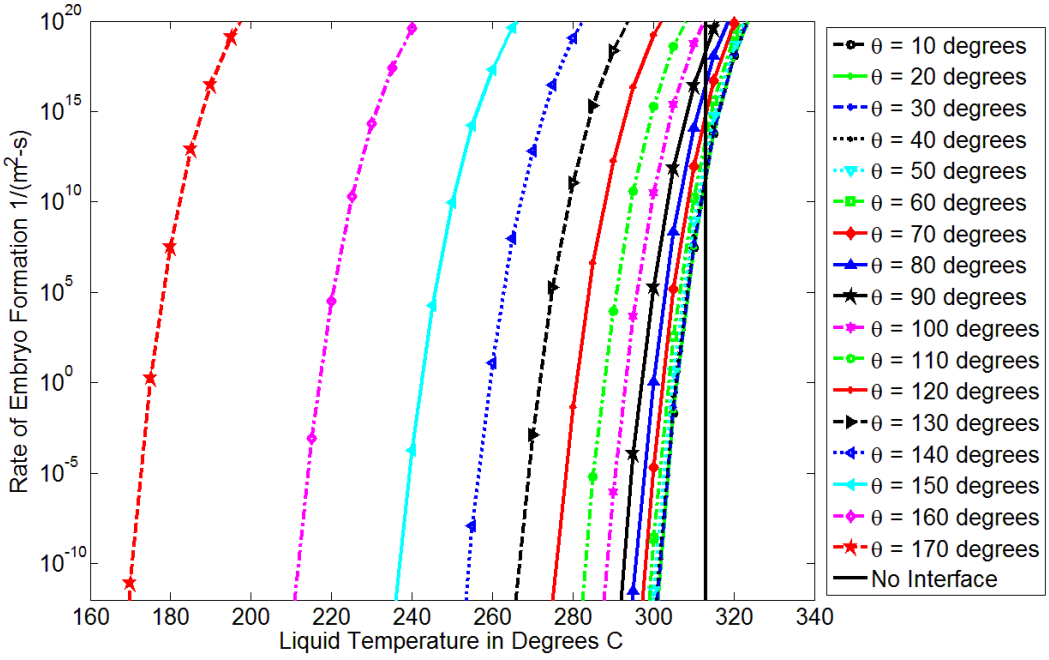

Figure 2-3: Rate of embryo formation on a smooth surface as a function of liquid temperature for various contact angles.

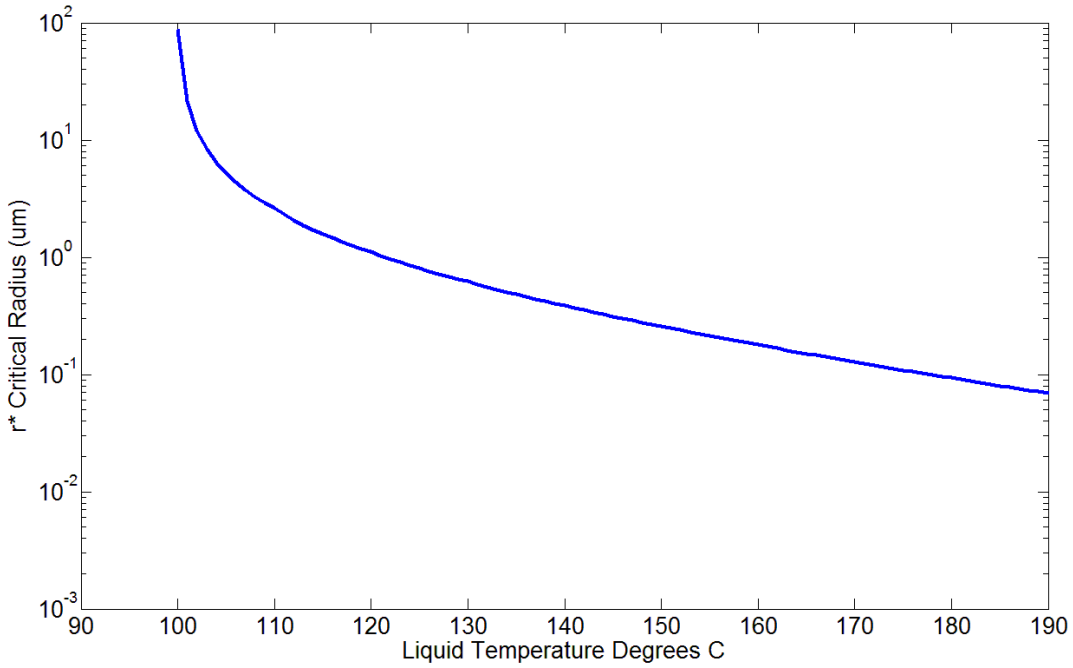

Figure 2-4: Young-Laplace equation plotted for water for various temperatures.

However, for nano-structured surfaces defects of this size do not exist and superheats calculated using the microscale boiling theory should approach those shown in Figure 2-3.

Using Molecular Dynamics simulations with a Lennard-Jones potential, Novak et al. [5] demonstrated that nanometer scale structures could be used to exert some influence over bubble nucleation rate and location. Defects on the order of the critical nucleus did not change the rate of nucleation, while defects much larger than the critical radius increased nucleation rates by two orders of magnitude. The affinity of the fluid for the surface played a large role and nucleation was much more likely at nanostructures with a weaker attraction of the fluid to the surface which yield a higher contact angle. Novak et al. also demonstrated that dissolved gas is not necessary to increase nucleation on the nanometer scale [5].

2.2 Pool Boiling Heat Transfer

Pool boiling refers to boiling from a heated surface with a fluid at rest. The fluid may be either at saturation or subcooled. At low heat flux, the surface first transmits heat to the pool via natural convection. In natural convection the fluid next to the surface is heated and its density lowered, which makes the fluid rise due to buoyancy. As the heat flux is increased, the wall temperature correspondingly increases, and eventually the onset of nucleate boiling occurs. A phase change occurs near the heat transfer surface where a vapor bubble forms, grows, and then departs from the surface. Nucleate boiling can transfer large amounts of heat because of the large heat of vaporization required for the phase change. As the heat flux is increased further more vigorous boiling occurs and bubbles grow and depart more frequently from the surface. In a temperature-controlled experiment, eventually an unstable boiling regime known as transition boiling is reached. During transition boiling large vapor pockets are produced at the surface causing the heat transfer coefficient to drop dramatically due to the poor heat transfer coefficient of the vapor layer. The heat transfer coefficient is defined in the equation below.

$$q'' = h(T_{wall} - T_{bulk}) \qquad \textbf{Eq. 2-5}$$

where q'' is the heat flux (W/m^2), h is the effective heat transfer coefficient (W/m^2-K), T_{wall} is the wall temperature of the heat transfer surface (K), and T_{bulk} is the bulk fluid temperature (K).

The vapor layers may collapse and rewet the surface but if the temperature is raised further, stable film boiling occurs. In a heat-flux controlled experiment, the transition boiling region is skipped, and an excursion from nucleate boiling to stable film boiling occurs at the critical heat flux. The boiling curve is shown in Figure 2-5 [1].

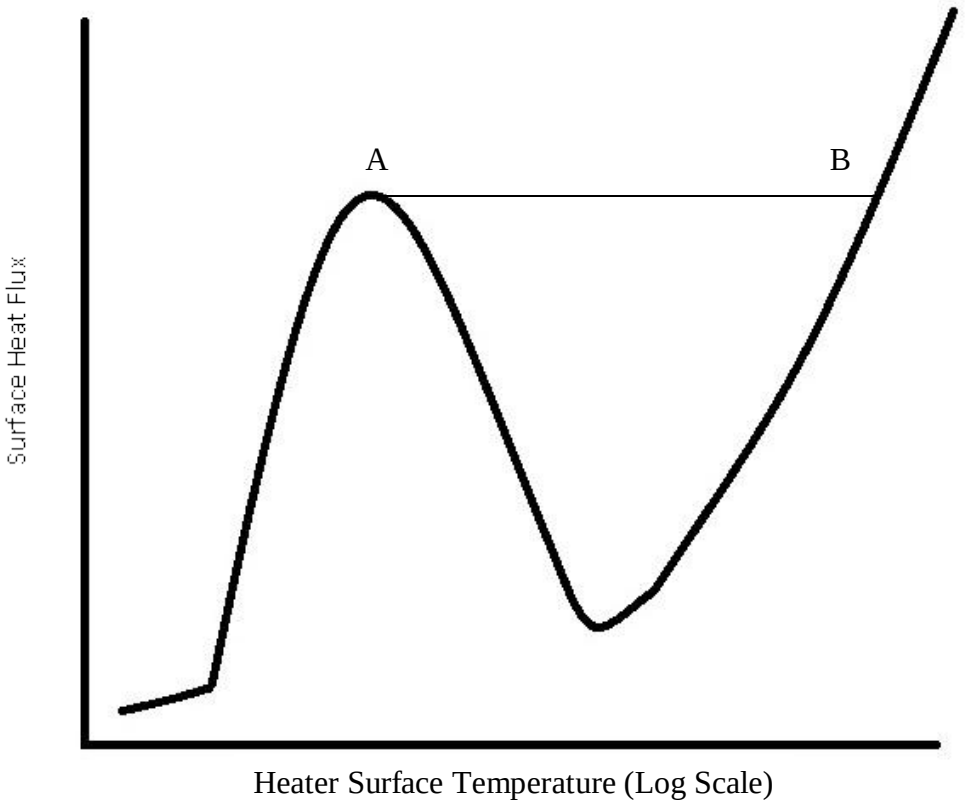

Figure 2-5: Characteristic pool boiling curve.

The first part of the curve, which has a very shallow slope is the natural convection region before boiling occurs, and density changes are responsible for fluid circulation. The sharp change of the slope marks the onset of nucleate boiling (ONB). Nucleate boiling has a far superior heat transfer coefficient to natural convection, and thus the surface temperature does not rise as fast for a given increase in the heat flux [1]. Once point A is reached the heat transfer coefficient is drastically reduced, and if the heat flux remains unchanged the system will shift to point B. This is the transition to film boiling and can lead to an increase in wall temperature of over 1000°C and usually leads to burnout [1].

2.3 Critical Heat Flux

The exact mechanism of reaching CHF is not exactly known but the prevailing theory for pool boiling is that the large amount of vapor formation at the surface prevents the rewetting of

the surface by the surrounding liquid [1]. Zuber proposed a correlation based on an array of vapor jets and their interaction [6].

$$q''_{critical} = K\rho_g h_{fg}\left[\frac{g\sigma(\rho_f - \rho_g)}{\rho_g^2}\right]^{1/4} \qquad \textbf{Eq. 2-6}$$

Where $q''_{critical}$ is the critical heat flux (W/m^2), K is a dimensionless constant that depends on the boiling geometry, h_{fg} is the latent heat of vaporization (J/Kg), g is the acceleration due to gravity (m/s^2), σ is the surface tension of the liquid (N/m), ρ_f and ρ_g are the densities of the liquid and vapor phases respectively (kg/m^3). However, this is based solely on hydrodynamic phenomena and does not take into account surface energy, wettability, roughness, porosity, or any surface characteristics. For this reason the hydrodynamic model appears to not capture all of the phenomena involved in reaching critical heat flux since experimentally surface characteristics appear to play a role [7].

3 Nano-Engineering Surfaces

3.1 Nano-Surfaces for Boiling

Nano-surfaces for boiling heat transfer enhancement are being studied because of their apparent ability to change surface characteristics to allow for rewetting of the surface during boiling, and increasing heat transfer and critical heat flux. Ahn et. al has used carbon nanotubes on surfaces to increase CHF by up to 60% and the mechanisms were identified to be the larger heat transfer surface, increased solid-liquid contact due to nanotubes, disruption of the micro-layer, and pinning the liquid-vapor contact line [8][9]. Nanowires have also been vertically oriented on a boiling surface and increased the heat transfer coefficient by more than 100% [10]. These nanowires reportedly help rewet the surface through capillary action and their micro sized cavities between the nanowires may create stable vapor columns and change the instability wavelength, which is defined below.

$$\lambda = C_1 2\pi \left[\frac{\sigma}{g(\rho_f - \rho_g)}\right]^{1/2} \qquad \textbf{Eq. 3-1}$$

Where λ is the Taylor instability wavelength (m), C_1 is a constant that ranges from 1 to $\sqrt{3}$, and the remaining symbols are defined above in Eq. 2-6. For water at 1 atmosphere and saturation conditions the value varies from approximately 1.5cm to 2.7cm. Similarly, Ujereh et al. have used carbon nanotube arrays to decrease the incipience superheat, increase CHF and the heat transfer coefficient [11].

Furberg et al. have patented a nanosurface of porous layers on a substrate [12]. This structure is electrodeposited and takes advantage of both micron sized surface features and dendritic nanostructures. The structure is very porous, and the pores are interconnected well allowing for vapor escape. The dendritic structures alter the micro layer and increases surface

area, which increases boiling heat transfer. These surface characteristics lead to reports of surface superheats of less than two degrees for some surface morphologies and improved heat transfer coefficients for boiling in R-134a [12]. Vemuri et al. also observed that a nanoporous surface decreased the incipient superheat by about 30% compared to a smooth surface [13]. Kunugi et al. have also seen over 180% increase in the heat transfer coefficient by creating a nanoporous layer out of ~100nm size particles[14].

Other researchers have looked into "painting" a surface with a microstructured material to increase boiling heat transfer [15][16]. You et al [15] patented a coating containing a glue with a solvent loaded with particles that create cavities. These surfaces reported a decrease of up to 85% in the superheat for the onset of nucleate boiling, up to 80% reduction in nucleate boiling superheats, and over 100% increase in CHF when boiling FC-72 on silicon[13]. O'Conner [16] also saw similar enhancements when using other microstructured metallic particle coatings.

Nam et al. have observed steady vapor bubble nucleation from nanoscopically smooth hydrophobic regions placed on a silicon substrate, which have very low nucleation onset temperatures of ~9°C, which cannot be explained by traditional nucleation theory[17]. Kim et al. have increased CHF by engineering a surface to have good wettability and capillarity [18].

3.2 Layer By Layer Deposition

Layer-by-layer deposition is used to build a thin film nanoparticle coating one layer of nanoparticles at a time. This process was first introduced by Iler in 1966 for creating thin films of colloids, and since then has been expanded to numerous systems with many parameters able to be controlled, and now to nanoparticle systems [19][20][21][22]. First, the surface to be coated is dipped into a bath of charged polymer particles. The surface is then rinsed and then dipped

into a nanoparticle suspension of the opposite charge, and the charge is carefully controlled by adjusting the pH. The surface is then rinsed creating a single bilayer and the process is repeated to construct the desired number of bilayers. The thickness per bilayer is controlled by the pH and by the nanoparticle size [20][21][22]. The process is shown in Figure 3-1.

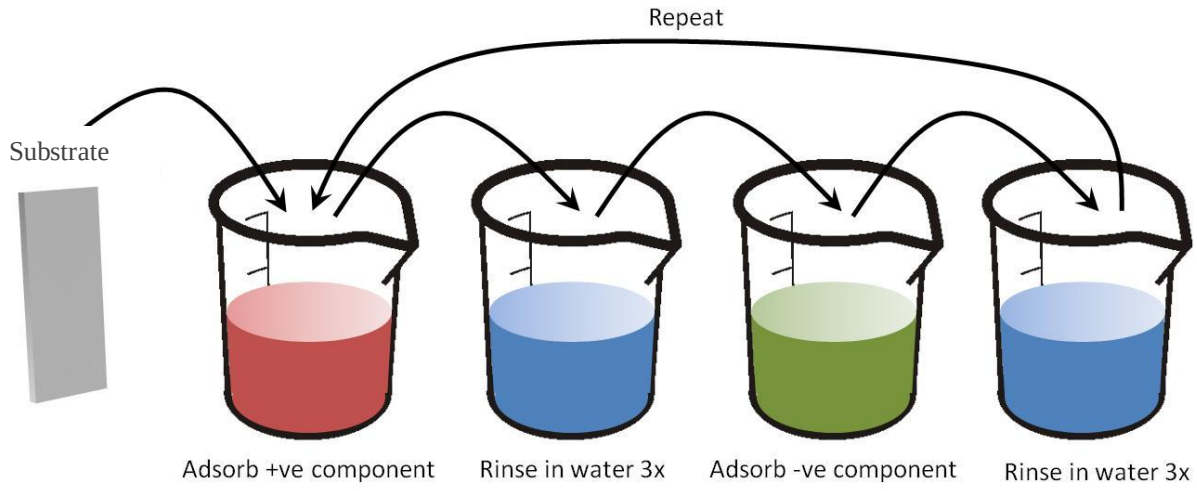

Figure 3-1: Layer-by-layer Process for assembling multilayers. PAH (pH 7.50) is the cation and SiO2 (pH 9.00) is the anionic species. ***Illustration courtesy of Erik Williamson.***

Superhydrophilic (contact angle less than 5 degrees in 0.5 seconds) surfaces can be created using SiO_2 nanoparticles with poly(allylamine) hydrochloride also called PAH. These surfaces can be made using the above technique with the PAH/SiO_2 system, and they can then be calcinated at 550°C for 1 hour to remove the PAH which makes the coatings more robust and more wetting. Cebeci et al. report the wetting behavior to be due to the chemical composition, the nanotexture, and nanoporosity [23]. These hydrophilic layer-by-layer coatings using silica nanoparticles have been shown to provide increases in CHF of up to 100% and the film thickness also increased CHF [24].

Hydrophobic surfaces with contact angles greater than 140 degrees can also be created by careful selection of nanoparticle sizes using the method described above and coating the surface

with a monolayer of 1H,1H,2H,2H-perfluorodecyltriethoxysilane commonly referred to as fluorosilane [25].

3.3 Ultraviolet Ozone (UVO) Patterning of the Surface

UVO is a common procedure for cleaning silicon wafers to obtain atomically clean surfaces for various processing techniques [26]. It works by 184.9nm UV light breaking down oxygen into atomic oxygen and 253.7nm UV light emitted by a low pressure mercury bulb breaking down ozone by photodisassociation. Then secondary reactions from the highly active oxygen occur to oxidize organic materials and they desorb from the surface. When both wavelengths are present atomic oxygen is constantly generated and ozone is continually formed and destroyed [27][28]. Some reactions also may occur directly from the UV light from the breaking of chemical bonds of hydrocarbons, specifically from the 253.7nm radiation [29].

Researchers have used the UVO process to destroy volatile species on the surface of a substrate in a specific pattern. This can be done by using a mask, or by varying exposure time across the sample [30][31][32]. When using a mask, it is important that the mask be transparent to the 184.9nm and 253.7nm UV light, and that there be area for air flow across the transparent regions to allow for the desorbed species to be removed. A good solution to the transparency issue is to use fused quartz silica. It has a very high transmission of the UV light wavelengths that are important. As can be seen in Figure 3-2, quartz has a 90% or better transmittance over wavelengths of interest.

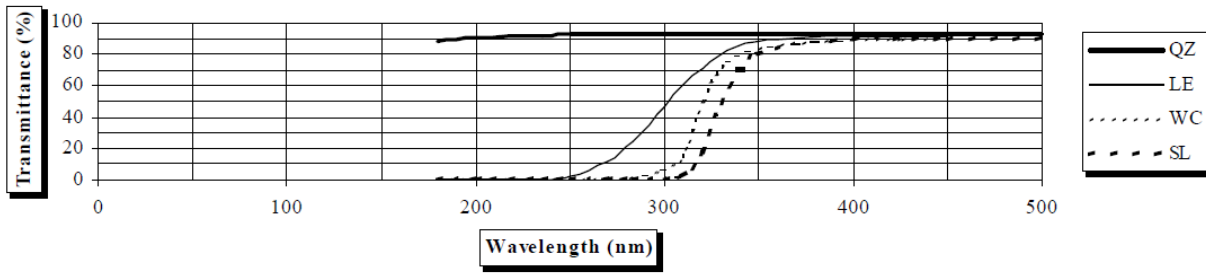

Figure 3-2: Spectral transmittance curve for a 2.3mm thick substrate. QZ is fused quartz glass, LE is Borofloat glass, WC is White Crown glass, and SL is green soda lime glass. Chart reproduced with permission from [33].

The quartz used for the masks was 2.3mm thick and obtained from Nanofilm. The masks were manufactured by Advance Reproductions and the masking agent on the quartz is 110nm layer of chromium that blocks the UV at the desired locations. A diagram of the patterning process is shown in Figure 3-3.

By patterning the surface with various combinations of hydrophobic "islands" in a hydrophilic "sea" there is a potential to create a surface that has a high nucleation site density from the hydrophobic islands, which should help improve the heat transfer coefficient. At the same time the hydrophilic sea can provide a rewetting mechanism to help improve the CHF of the surface.

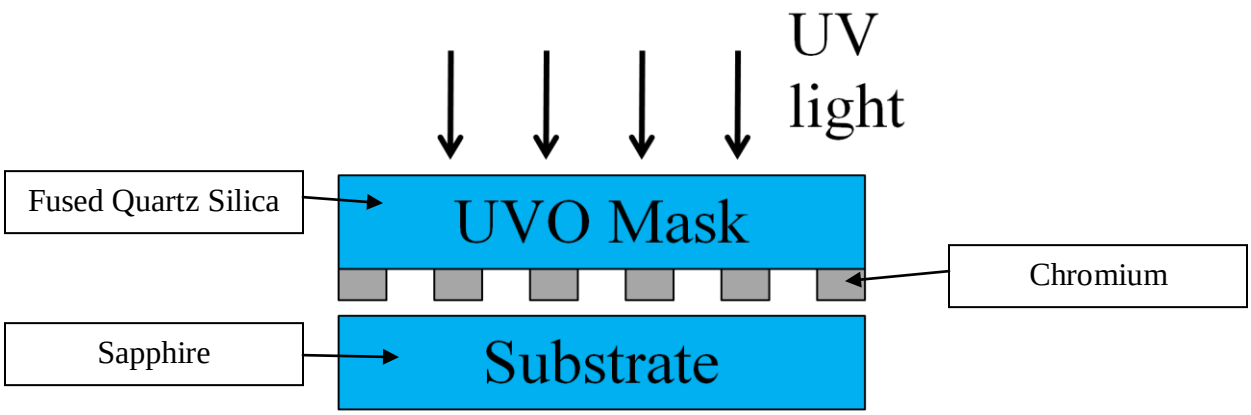

Figure 3-3: Diagram of UVO patterning process. In reality the chromium is in contact with the substrate, the gap is left for clarity in the diagram. The diagram is not to scale.

The complete matrix of masks obtained is shown in Table 3-1 and drawings of some example masks are shown in Figure 3-4. The masks patterns are dots, either clear or opaque on a hexagonal grid spaced 1mm or 2mm apart.

Table 3-1: All of the masks obtained from Advance Reproduction

Dot Size	Dot Pitch	Transparent Region
12µm	1mm	Matrix
12µm	1mm	Dots
12µm	2mm	Matrix
12µm	2mm	Dots
160µm	1mm	Matrix
160µm	2mm	Matrix
260µm	1mm	Matrix
260µm	2mm	Matrix

The relative thinness of the chromium results in poor circulation of air underneath the mask and results in long UVO exposure times of two hours per sample for the patterning process.

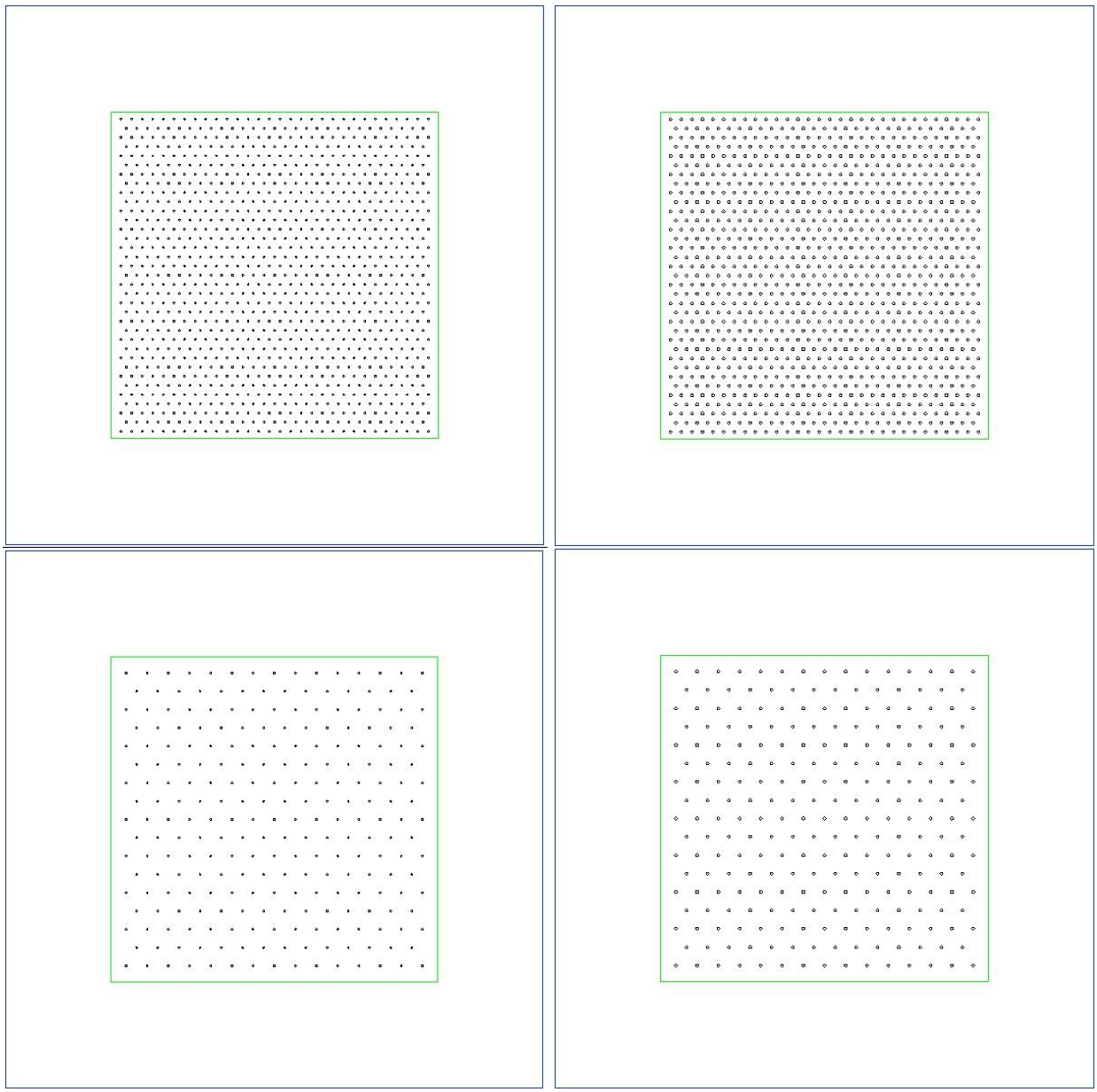

Figure 3-4: Masks from Advance Reproduction. 160µm dots on 1mm pitch [Top Left]. 260µm dots on 1mm pitch [Top Right]. 160µm dots on 2mm pitch [Bottom Left]. 260µm dots on 2mm pitch [Bottom Right].

4 Heater Design

Similar IR boiling work has been done previously by Gerardi [34], and Gerardi's heater design is considered the reference design.

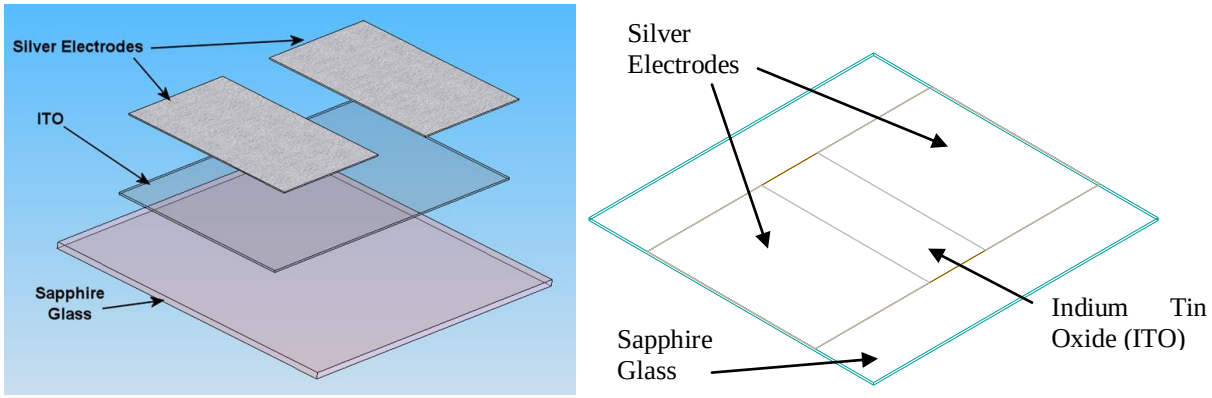

Figure 4-1: Reference ITO heater blowup (left) [34] and drawing (right). The heater consists of a sapphire substrate, an ITO coating, and silver electrodes.

The sapphire glass is 50.8x50.8x0.4mm, is optical quality, and has scratch-dig specification of 40-20. The reference heater is supplied by Diamond Coatings and is manufactured by cleaning the sapphire glass with alcohol, and placing them in a vacuum chamber and plasma cleaned. The ITO is then sputter coated with a Magnetron sputtering at several eV. The resulting ITO is ~700nm thick and has a resistivity of <10Ω/sq. The silver electrodes are composed of a silver ink that is screen printed on top of the ITO at 20-25μm thickness and creates the active heater area between the two electrodes, which is 30mm x 10mm.

The heater must provide the heat necessary to reach CHF for pool boiling experiments carried out in the pool boiling facility shown in Figure 4-2**.** The pool boiling experiments will be conducted by controlling the heat flux, with the possibility of taking both IR video and HSV of the boiling process. During the boiling tests the heater surface needs to remain free of

contamination and not oxidize to preserve the topography and chemistry of the engineered surface.

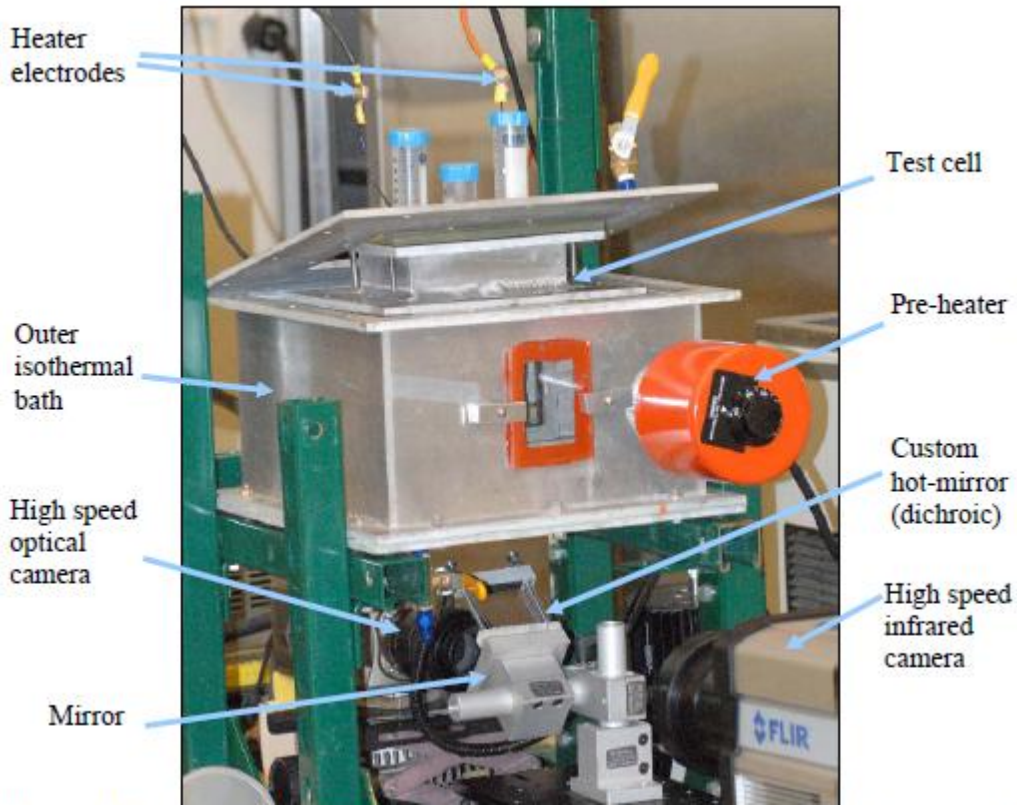

Figure 4-2: Photograph of the pool boiling facility configured to capture both IR images and high speed video, figure reproduced from [34]**.**

4.1 Heater Design Constraints

Several heater designs were considered for this work. The heater design has many conflicting restraints. These ideal heater constraints are described briefly in Table 4-1.

Table 4-1: Heater design considerations and basis

Heater Design Constraint	Basis for constraint
Transparent to visible light	Capable of imaging heater from the bottom with high speed video camera
Transparent substrate to IR but surface opaque to IR	Allows imaging of the surface of the heater with a high speed infrared camera while allowing IR waves to pass through the substrate
>99% of the heat must be generated in the active heater area	Allows for accurate determination of the heat flux by measuring voltage and current from the power supply
Heater and electrodes must remain intact and not oxidize throughout test	Maintains clean surface by preventing corrosion products from entering the water and depositing on the surface during boiling and altering the boiling surface topography and energy
Cost per experiment <$200 including heater and other disposable materials needed for the test	Budgetary constraint based on available funds for the number of anticipated experiments
At 3 MW/m^2 heat flux current <20A and voltage <150V **or** current <500A and voltage <20V	Maintains the voltage and current within the capacity of available power supplies
Active heater dimensions ≥1x1cm	Ensures that there are a minimum of 5 Laplace lengths across the heater in each dimension and has implications to voltage and current constraints.
Electrode dimensions ≥1x1 cm	Defines minimum area for electrodes to allow for attaching wires for electrical connections
Optical properties constant up to 200°C	Optical properties (particularly for IR) need to remain constant throughout the test to minimize difficulties in determining surface temperature
High water contact angle for base heater ~90 degrees	Allows for boiling differences between hydrophobic and hydrophilic structures to be observed based on a control heater that has an intermediate wettability
Heater components insoluble in water	Ensure integrity of heater in boiling water
Thermal stresses between various layers due to differences in thermal expansion do not rupture layers	Ensure integrity of heater during and after temperature changes

4.2 Considered Heater Designs

Heater designs that were considered are shown below in Table 4-2.

Table 4-2: Heater designs considered and their pros and cons

Heater Design	Pros	Cons
1) ITO heater on sapphire substrate with silver ink electrical pads (reference design)	-Transparent to visible light -Opaque to IR on surface -Optically stable to 200°C -Good contact angle	-High voltages necessary -Corrosion problems from silver pads due to high voltages
2) ITO heater on sapphire substrate with carbon electrical pads	- Same as reference design	-High voltages necessary - >20% heat production in pads at achievable thicknesses
3) ITO heater on sapphire substrate with thick ITO for electrical pads	-Same as reference design	-High voltages necessary -Prohibitively Expensive (~$1000 per heater)
4) ITO heater on sapphire substrate with silver ink electrical pads put down first with ITO on top	-Same as reference design	-High voltages necessary -No benefit on pad corrosion gained to reference design
5) ITO heater on sapphire substrate with silver ink electrical pads with printed organic dielectric layer of electrical pads only.	-Same as reference design plus reduced corrosion from silver electrical pads	-High voltages necessary -Small amounts of dielectric on heater cause hot spots at dielectric/heater interface -CHF event has high probability to initiate from dielectric
6) ITO heater on sapphire substrate with silver ink electrical pads with SiO_2 dielectric layer.	-Transparent to visible light -Opaque to IR on surface -Optically stable to 200°C	-High voltages necessary -Expensive -SiO_2 Layer doesn't fully inhibit corrosion -Contact angle not as desirable as reference design
7) ITO heater on sapphire substrate with silver ink pads tested inverted	-Transparent to visible light -Optically stable to 200°C -Good contact angle -Chemically inert -Electrical contacts made outside test bath	-High voltages necessary (but not in contact with boiling surfaces) -Opaque to IR on surface opposite of the boiling surface (degraded IR images)
8) Solid metal self supporting heater (~0.5mm thick)	-Simple -Inexpensive -Good contact angle	-Not IR transparent -Not transparent to visible light -Difficult to control active heater area -Requires very high currents to maintain low voltage
9) Thin metal heater on sapphire substrate	-Opaque to IR on surface	-Requires very high currents to maintain low voltage -Two step process to reach required thicknesses economically -Opaque to visible light -Difficult to control active heater

Table continued on next page

Heater Design	Pros	Cons
10) Silicon Heater with pads on opposite side from water	-Simple -Optically stable to >200°C -Electrical contacts made outside test bath -Acceptable contact angle	-Opaque to visible light -IR visibility strongly dependent on doping and processing techniques. low resistivity wafers necessary for limiting voltage and reaching CHF have poor IR visibility -Surface is not IR opaque -Difficult to control active heater area -Silicon oxidizes at high voltages
11) Silicon Heater with pads on opposite side from water and Si_3N_4 dielectric coating	-Same as 10)	-Same as 10) but oxidation reduced - Si_3N_4 dissolves in boiling water
12) Silicon Heater with pads on opposite side from water and annealed HSQ dielectric coating	-Same as 10)	-Same as 10) but Silicon oxidation reduced
13) Silicon Heater SiO2 insulating layer with overlaying Si layer (SOI wafer)	-Same as 10)	-Same as 10) but Silicon oxidation drastically reduced

Each heater design is discussed and its merits and problems are analyzed.

4.2.1 The reference heater design

The reference heater design shown in Figure 4-1 has excellent optical properties over the temperature ranges of interest. The ITO film does go through a phase change at ~250°C, which alters the IR optical properties as well as resistivity of the film. The film does not let IR pass through it so when the ITO is the boiling surface, the majority of the temperature signal comes from the ITO so the temperature of the surface can be directly read by the IR camera [34]. The high resistivity of the ITO and the cost limitations of sputtering a thicker layer lead to high voltages at CHF of ~50V on the silver electrodes and the ITO. This drives multiple chemical reactions including electrolysis of water and oxidation of the silver electrodes. This oxidation

issue can be seen below in Table 4-3 which lists the half cell potentials for the reactions for potential electrode materials.

Table 4-3: Standard half cell potentials in acid medium at 25°C for potential electrode materials [35].

Half Cell Reaction	E^0 in Volts
$Ag^+ + e^- \Rightarrow Ag(s)$	+0.7991
$Ag^{2+} + e^- \Rightarrow Ag^+$	+1.980
$Ag^{3+} + 2e^- \Rightarrow Ag^+$	+1.900
$Au^+ + e^- \Rightarrow Au(s)$	+1.830
$Au^{3+} + 3e^- \Rightarrow Au(s)$	+1.520
$Au^{3+} + 2e^- \Rightarrow Au^+$	+1.410
$Cu^+ + e^- \Rightarrow Cu(s)$	+0.518
$Cu^{2+} + 2e^- \Rightarrow Cu(s)$	+0.339
$Cu^{2+} + e^- \Rightarrow Cu^+$	+0.161

For each candidate metal for the electrode, the potential needs to be kept below the lowest oxidation potential for that metal. Therefore, for copper the voltage would need to be below 0.399V, for Silver below 0.799V, and for gold below 1.520V.

The oxidation of the silver can be seen by looking at EDS on the ITO area before and after boiling. The spectra are similar except for the introduction of silver and magnesium for the fouled surface, which come from the electrodes and the aluminum bath. The bath is made from 6061 aluminum which contains 0.8% to 1.2% magnesium[36]. The aluminum and oxygen signal is depressed for the fouled surface since there is an oxidation layer and fewer electrons penetrate to the sapphire substrate.

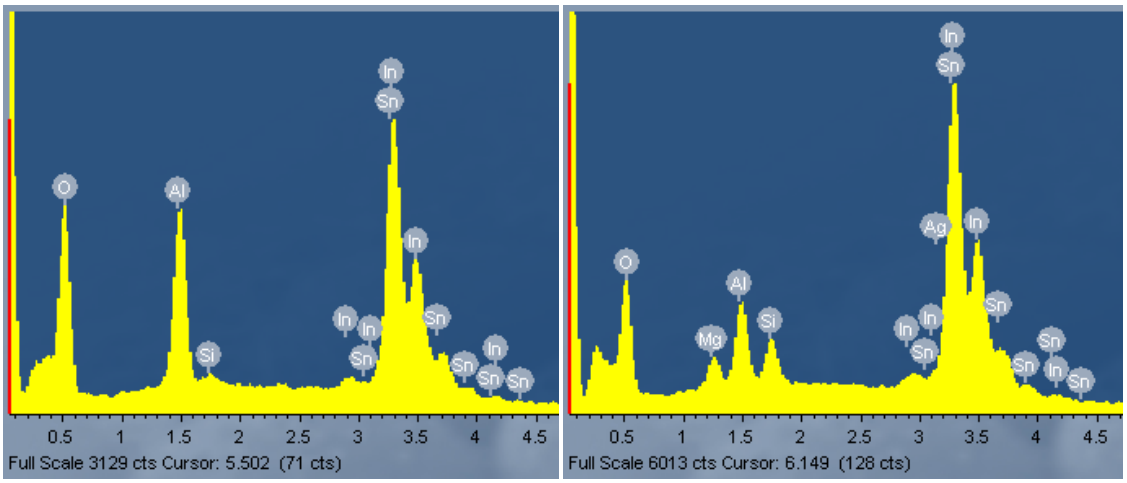

Figure 4-3: EDS spectrum from clean ITO surface (left) and fouled ITO surface (right).

4.2.2 ITO heater on sapphire substrate with carbon electrical pads

This design is similar to the reference design except that the silver pads are replaced with graphite. The graphite has a much higher resistivity than the silver and for the thicknesses that are feasible this design leads to unacceptable heat generation in the electrodes. The current silver ink used for the electrical pads has a resistivity of 0.055Ω/square. This leads to approximately 0.55% of the heat being produced in the silver electrodes instead of in the active heater area. If the silver ink were replaced with the lowest resistivity graphite ink available, which has a resistivity of 12-16Ω/square, this would result in up to 38% of the resistive heat being dissipated in the electrodes, which is clearly unacceptable.

4.2.3 The reference design with the silver electrodes replaced by ITO

This design, replaces the silver ink electrodes with ITO. The ITO would need to be 50 to 100 times as thick as the active heater area to minimize heat generation in the electrical pads. This design, while solving most of the oxidation problems, is prohibitively expensive due to the long times required to deposit the thick ITO. The price per heater would be thousands of dollars.

4.2.4 ITO heater on sapphire substrate with ITO on top

Same as the reference design but with the electrodes put down onto the sapphire first followed by the ITO. The goal of this was to protect the silver from the oxidizing environment of the water. However, this design was tested, but the reaction rates were not appreciably changed. This is apparently due to the ITO coating not being completely coherent. There were noticeable small dots, where oxidation started, presumably at locations that had small pores allowing water to access the metal underneath the coating. Furthermore, the coating is thin (~700nm) and sputtered onto the substrate, which is a line-of-sight deposition process. Therefore, it does not cover large changes in elevation on the sample well, and the edges of the silver pads were noticeably attacked.

4.2.5 ITO heater on sapphire substrate with printed organic dielectric layer

This design is the same as the reference design except that there is an organic dielectric printed over the top of the silver pads by Diamond Coatings (the supplier of the heater) and is shown in Figure 4-5. This method drastically reduces the corrosion from the silver pads. However, there is still oxidation along the edges of the dielectric where it is not possible to get perfect coverage of the silver pads without overlapping the active heater area. Also, any overlap of the dielectric on the active heater area leads to a hot spot on the heater which is a location where CHF will occur, often prematurely such as shown in Figure 4-4.

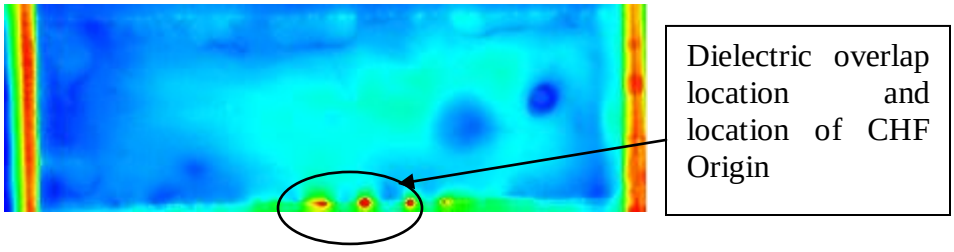

Figure 4-4 Picture of hot spot created from dielectric overlapping active heater area, and eventual location of CHF.

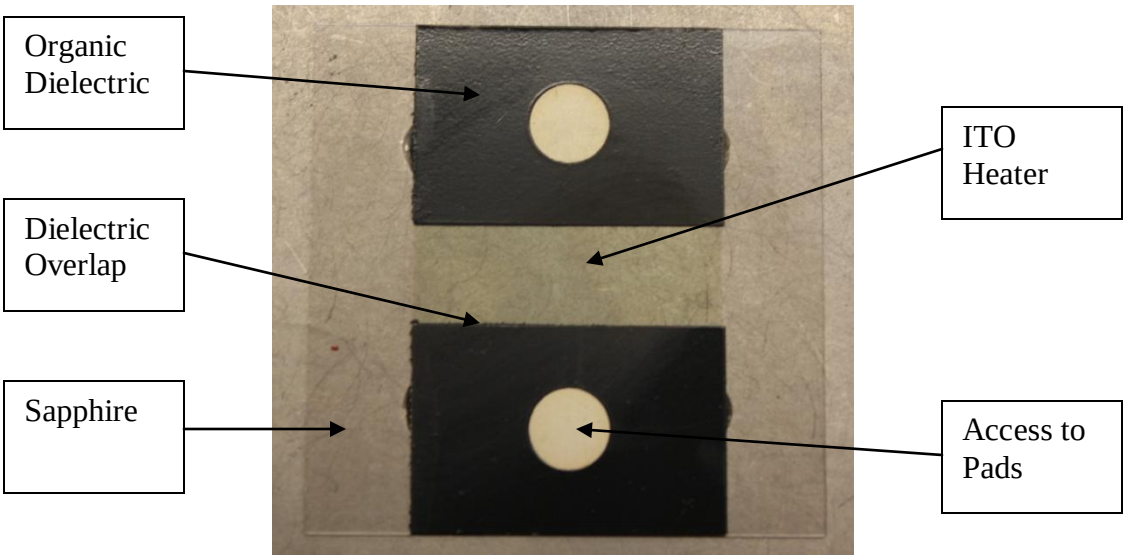

Figure 4-5: Picture of heater with organic dielectric coating over the silver pads. The black material is the dielectric, the light spots in the middle are access areas to the silver pads to make electrical connections.

4.2.6 ITO heater on sapphire substrate with SiO_2 dielectric layer

This design is the same as the reference design with an additional SiO_2 layer placed down on top of the silver pads as well as the active heater area with small access holes left on the silver pads to allow for electrical connections to be made to the pads and is shown in Figure 4-6.

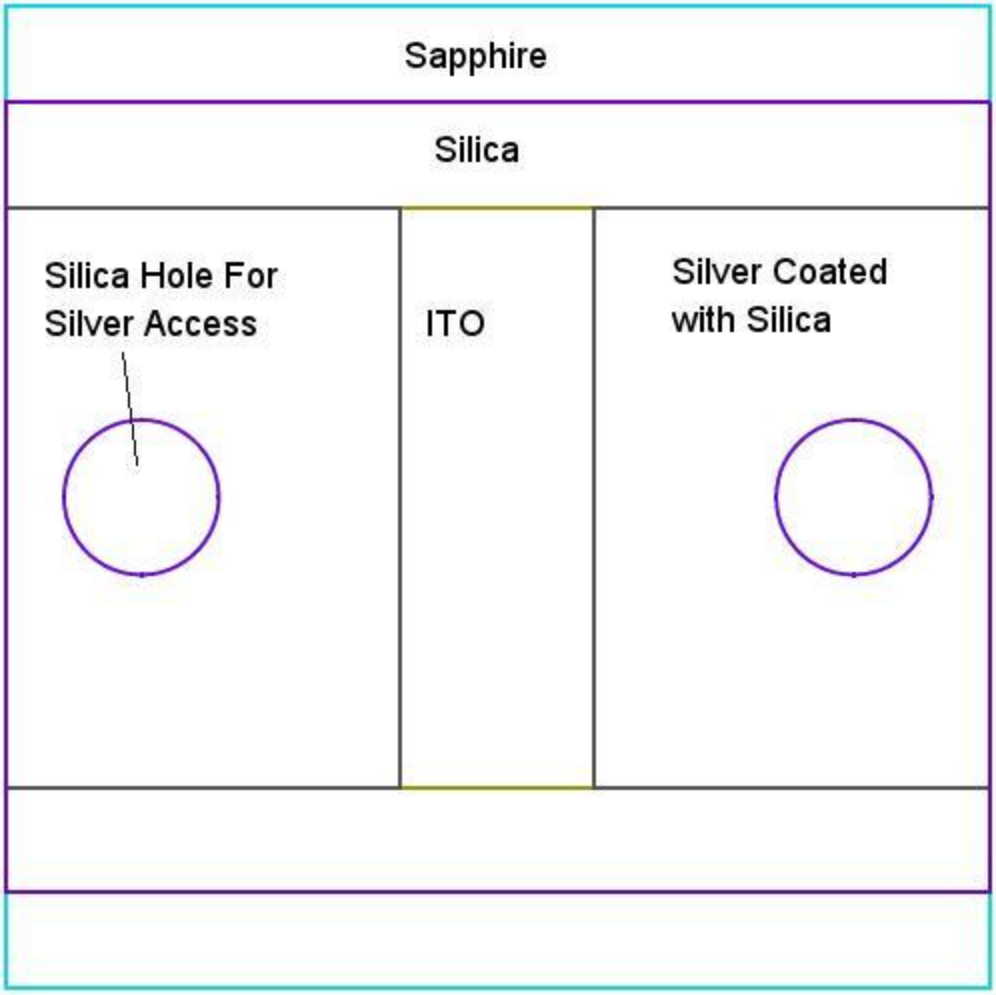

Figure 4-6: Silica coated ITO heater with access points for wire connections

This design had improved corrosion resistance, but the SiO_2 layer was not coherent and had many pores where oxidation of the silver pads was allowed to occur.

4.2.7 ITO heater on sapphire substrate with silver ink pads tested inverted

This design is exactly the same as the reference design but was tested inverted, where the sapphire was the boiling surface, and it was heated from the back with the ITO. This method prevents any electrical potentials from being in contact with the water and therefore prevents electrochemical oxidation of the surface. With this design the silver pads remain intact and there

is no change in the heater area due to the oxidation and erosion of the silver pads away from the active heater area.

However, the ITO is now on the back side of the heater and so the majority of the IR signal will originate from the back of the heater. Therefore, the thickness and thermal diffusivity of the substrate becomes very important in determining the quality of the IR images. The attenuation of a temperature oscillation (wave) traveling through the substrate can be found by solving the transient heat conduction equation

$$\frac{\partial T}{\partial t} = \alpha \frac{\partial^2 T}{\partial x^2} \qquad \textbf{Eq. 4-1}$$

Where T is the temperature (K), t is time (s), α is the thermal diffusivity (m^2/s), and x is position (m). Imposing an oscillation at the surface (effectively representing the ebullition cycles) and an unperturbed temperature at an infinite distance into the medium.

$$T(0,t) = T_0 + \Delta T_0 e^{i\omega t} \qquad \textbf{Eq. 4-2}$$
$$T(\infty,t) = T_0 \qquad \textbf{Eq. 4-3}$$

ω is the frequency of the temperature oscillation (rad/s). This yields the following time dependent temperature profile.

$$T(x,t) = T_0 + \Delta T_0 \exp\left(-\sqrt{\frac{\omega}{2\alpha}}x\right)\cos\left(\omega t - \sqrt{\frac{\omega}{2\alpha}}x\right) \qquad \textbf{Eq. 4-4}$$

A dimensionless temperature wave amplitude for any time t that can then be defined.

$$\frac{T(x,t)-T_0}{\Delta T_0} = \exp\left(-\sqrt{\frac{\omega}{2\alpha}}x\right) = \exp\left(-\sqrt{\frac{\pi f}{\alpha}}x\right) \qquad \textbf{Eq. 4-5}$$

This temperature wave reduction can be plotted for various materials with different thermal diffusivities vs. the distance into the material. This gives an estimation of the attenuation of the temperature wave traveling a distance x into the material and is plotted in Figure 4-7. The bubble departure frequency is an important parameter in this equation, and the higher the departure frequency the more attenuation of the temperature wave. A bubble departure frequency of 120Hz, which is a very high (and thus conservative in this context) frequency for nucleate boiling was used for the calculations shown in Figure 4-7. Clearly, materials with high thermal diffusivity are going to be the best materials to allow the temperature wave to pass through them unattenuated. However, to meet the requirement of being optically transparent, the best choice still is sapphire compared to other kinds of glasses. Furthermore, the thinner the sapphire (while considering price, strength and manufacturability), the better the transmission of the wave. For this heater design that was finally chosen, sapphire of 0.25mm was chosen with a scratch-dig specification of 40-20. For 0.25mm thick sapphire 25% or more of the temperature wave remains even for 120Hz bubble departure frequency. The temperature wave reduction can also be plotted for a fixed material for various bubble departure frequencies, and that is shown in Figure 4-8.

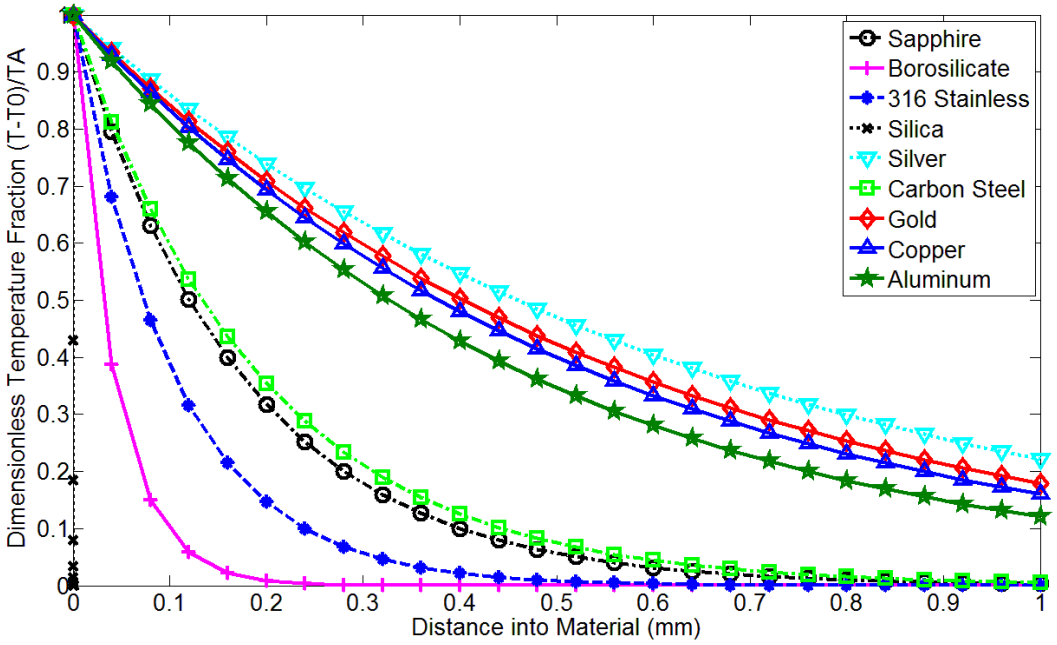

Figure 4-7: Temperature wave reduction for 120 Hz bubble departure frequency for various materials.

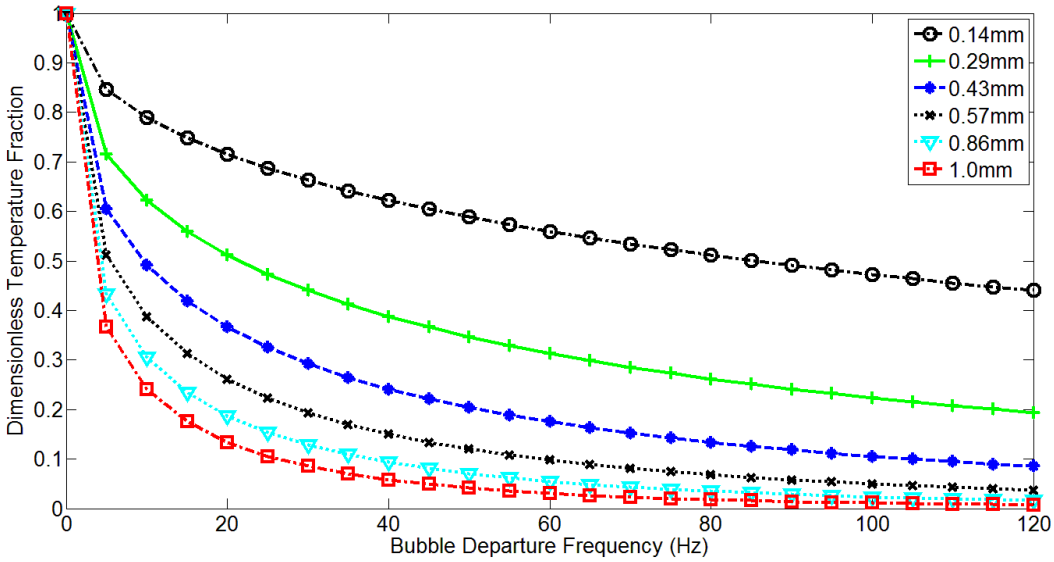

Figure 4-8: Temperature wave reduction for sapphire for various bubble departure frequencies.

The velocity of the temperature wave through the medium can be described by Eq. 4-6.

$$v = \sqrt{2\alpha\omega} = \sqrt{4\pi f \alpha} \qquad \textbf{Eq. 4-6}$$

The frequency is represented by f (Hz). Plotting Eq. 4-6 for sapphire is shown below in Figure 4-9. The time required to cross the sapphire substrate gives a metric for how delayed the temperature signal read by the camera is relative to the temperature on the surface.

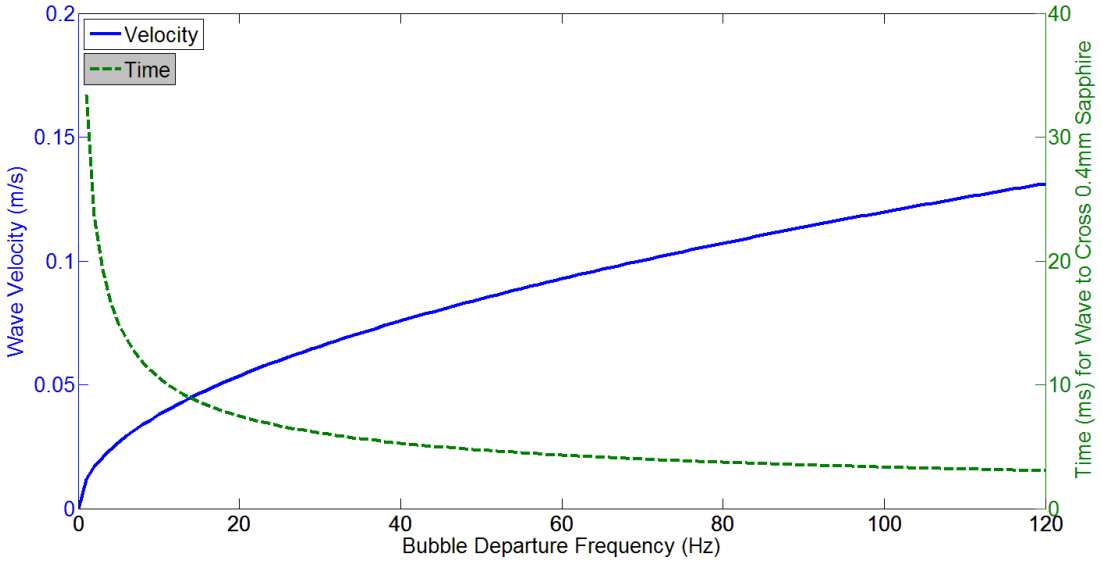

Figure 4-9: Temperature wave velocity in sapphire for various bubble departure frequencies and the time required for wave to cross 0.4mm of sapphire.

4.2.8 Solid metal self supporting heater (~0.5mm thick)

This design is simple, inexpensive, and has a high starting contact angle to explore the effects of wettability changes.

However, it is not IR transparent so the temperature wave reductions shown in Figure 4-7 and Figure 4-8 would apply, and at the necessary thicknesses of 0.5mm needed to maintain the heater as self supporting would result in large temperature wave attenuations. Furthermore, at the large thicknesses needed, very high currents would be needed to reach CHF. This is shown in Figure 4-10. Voltages would need to be kept below those shown in Table 4-3.

These heaters would also not be transparent to visible light so visualization with a high speed video camera would not be possible. There would also still be an electrical potential on the surface, although it could potentially be kept low enough to prevent any of the oxidation reactions to be driven. There is also the additional issue of controlling the active heater area. Since the heater would be a solid piece of metal, a method for attaching connections capable of carrying the high currents without resistive losses in a repeatable fashion to keep the same heater area for each test would have to be devised.

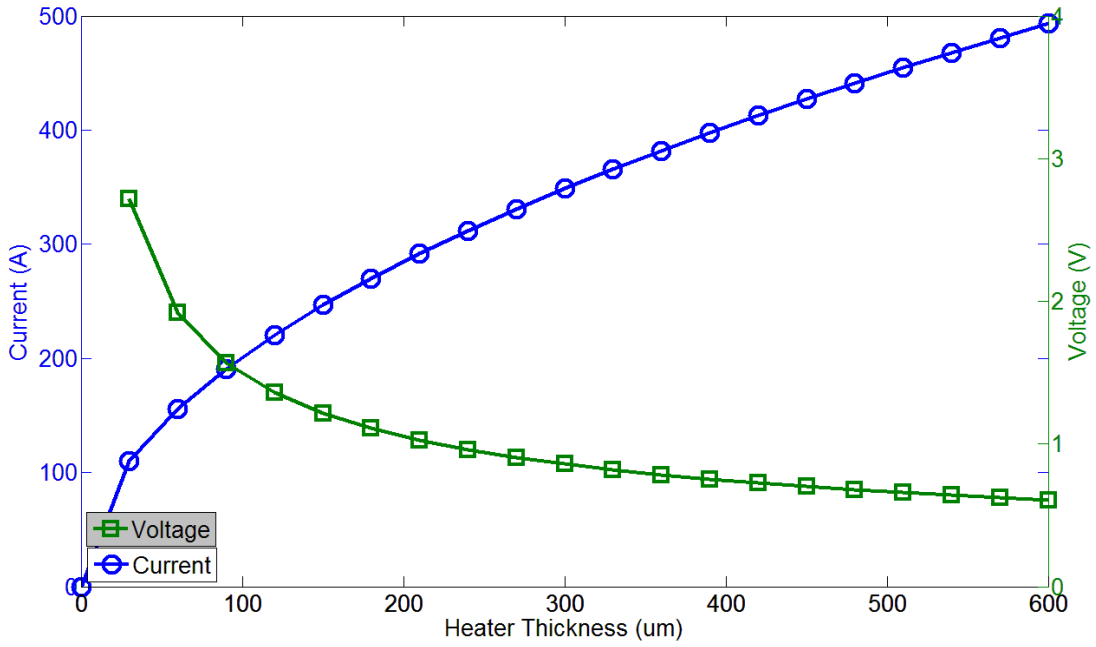

Figure 4-10: 316 stainless steel heater current and voltage vs. heater thickness for 3MW/m^2 heat flux.

4.2.9 Thin metal heater on sapphire substrate

This heater would be opaque to IR on the boiling surface, and as long as the heater was kept thin would provide clear IR images since the attenuation of the temperature wave through a

few 10s of microns of metal would be minimal as shown in Figure 4-7. The heater would have the possibility of having drastically reduced corrosion by keeping the voltage below the oxidation potential for the metal being used. For instance, for silver that is shown in Figure 4-11 has an oxidation potential of 0.799V, which for a 500A limit (limit of the power supply available) the voltage for 3MW/m^2 would be less than 0.6V.

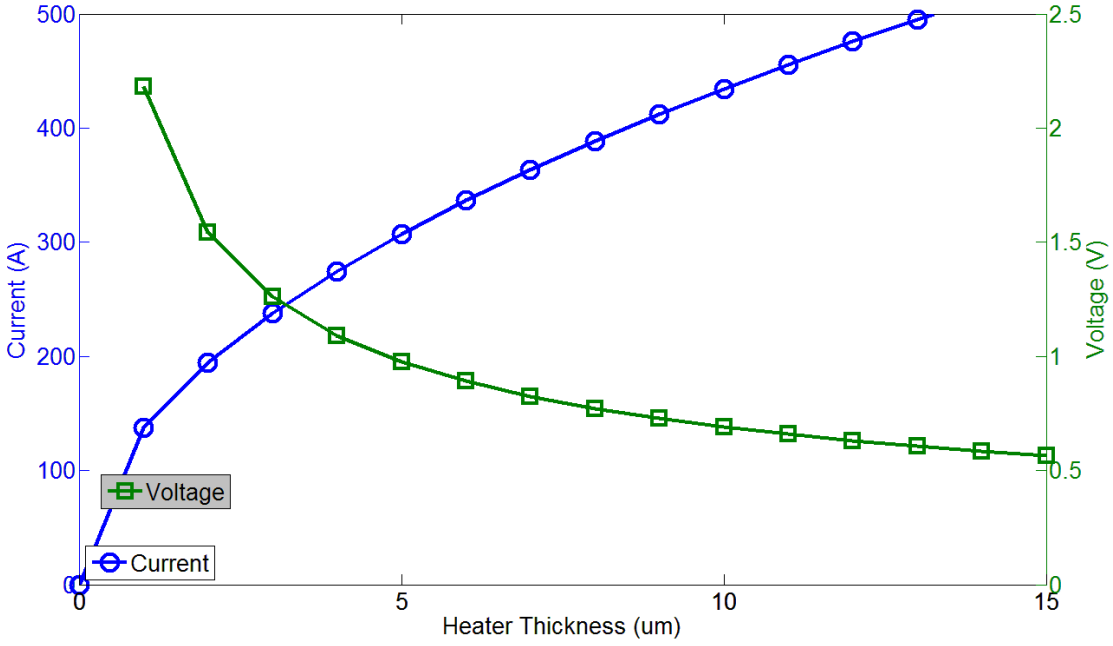

Figure 4-11: Current and voltage plotted versus thickness for a 1x1 cm silver heater at 3MW/m^2.

This heater would still have the disadvantages already described in section 4.2.8 without the temperature wave attenuation issue since the boiling would be taking place on the thin metal surface, where the attenuation is minimal, and the sapphire is transparent to the IR signal. There is also the one additional disadvantage of having to utilize a two step process to coat the substrate. The necessary thicknesses are on the order of 10s of microns as shown in Figure 4-11, so this exceeds the thicknesses economically obtainable by sputtering, or CVD; therefore, a two

step process of sputtering a metal layer would first be necessary to make the sample conductive, and then the sample would need to be electroplated. These processes would require two different vendors, adding additional lead time and cost to the heaters.

4.2.10 Silicon heater with pads on opposite side from water

This silicon heater design is simple and could be made locally at MIT. Silicon is also optically stable to 300°C and higher so there would not be the same optical constant changes that occur in ITO at the phase change ~250°C. The electrical connections would be made outside the water bath so the metals used to make the electrical connections would not oxidize. The contact angle of polished silicon is fairly low and is around 10-20°C depending on the type of silicon wafer used. This could be modified by using an adhesion layer created by coating bilayers of positive and negative polymers as described in section 3.2.

However, once again this heater is opaque to visible light preventing optical imaging from below. The IR transparency of silicon is highly dependent on the processing and doping technology. To reach CHF low resistivity wafers are necessary to prevent extraordinarily high voltages, and these wafers have poor IR visibility presumably because the extra energy levels created from doping allow for IR wave absorption thus making the wafer far less IR transparent. Furthermore, even with low resistivity wafers, the voltages reached would be far in excess of 50V (typical voltage for CHF on reference heater) and lead to rapid oxidation of the silicon heater (see Figure 4-12).

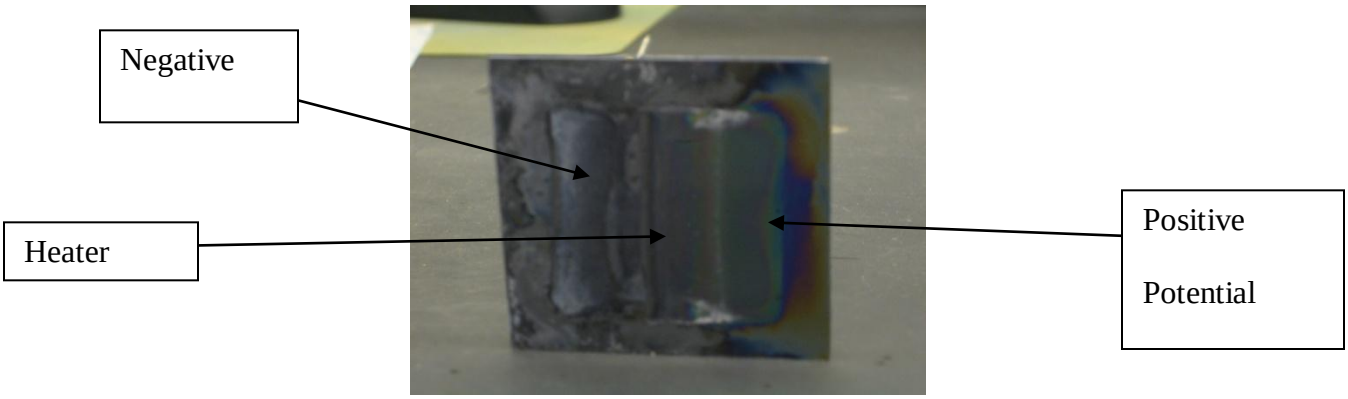

Figure 4-12: Silicon heater post testing. Notice the large depositions of silicon dioxide at the negative terminal of the heater.

The fact that the silicon wafer does not provide an IR signal itself like the ITO does, prevents the direct measurement of the surface temperature. Instead, an average temperature of the first few hundred microns of the water will be measured. The IR waves will have an exponential attenuation.

$$I(x) = I_0 10^{-\alpha x} \qquad \textbf{Eq. 4-7}$$

$$x = -\frac{1}{\alpha}\log_{10}\left(\frac{I(x)}{I_0}\right) \qquad \textbf{Eq. 4-8}$$

Where $I(x)/I_0$ is the fraction of the IR wave remaining and α is the attenuation coefficient (m^{-1}). If the distance is calculated where 99.9% of the IR waves will be absorbed, this will give as an estimate of the distance into the water that the temperature is being measured based on the IR re-emission.

Table 4-4: Water IR attenuation coefficients over IR camera sensitive range, and water 1/1000th thicknesses where 99.9% of the IR waves are attenuated [37].

Wavelength (μm)	Attenuation Coefficient α (1/cm)	One Thousandth Thickness $x_{\frac{1}{1000}}$ (μm)
3	10860	2.76
3.1	7430	4.04
3.2	3700	8.11
3.3	1650	18.18
3.4	698	42.98
3.5	334	89.82
3.6	198	151.52
3.75	119	252.10
3.83	111	270.27
4	151	198.68
4.5	411	72.99
4.66	468	64.10
4.8	431	69.61
5	308	97.40

From examining Table 4-4 it can be seen that at worst the depth of the water over which the temperature average would be measured is ~270μm. This does not seem to be an issue with using a silicon wafer, as the wafers provide a decent image; however, the low resistivity of the wafer makes the image not as clean and the central hot spots on the bubbles are not visible as they are on an ITO heater since the water temperature is being measured rather than the surface.

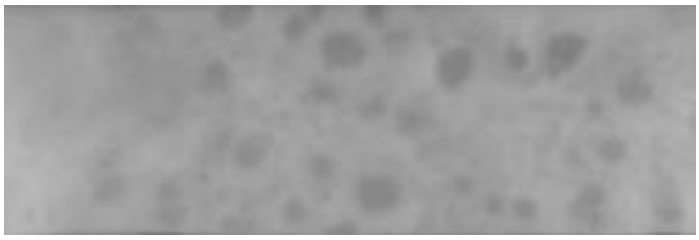

Figure 4-13: **368kW/m^2 heat flux for silicon heater. There is not as good of temperature difference between bubble departures and the rest of the fluid compared to an ITO heater due to measuring the temperature of the water and the relatively low resistivity of the wafer (which reduces transparency). Also, there is a loss of the central hot spot as the center of the bubble dries.**

A simple 1D heat conduction analysis was performed on this heater with constant heat transfer coefficient boundary conditions. The analysis was to prove heat losses through the bottom of the silicon heater are not excessive. Note that the silicon heaters are different from the ITO heaters in this sense as there is heat generation throughout the substrate. Even with very generous estimates of the heat transfer coefficient for natural convection, there was no appreciable fraction of the heat flux traveling through the bottom side at high heat fluxes except at very low heat fluxes (below 10^4 W/m^2), which are not are not of particular interest for this work (see Table 4-5). The temperature profile across the heater for different low and high heat fluxes can be seen in Figure 4-14 and Figure 4-15 respectively. The temperature across the 380μm heater varies by less than a couple of degrees at the maximum.

Table 4-5: **Ratios of heat flux through the bottom of the heater to the heat flux through the top of the heater (boiling surface) with a heat transfer coefficient (htc) for air of 4.3W/(m^{2}K). Each column in the table multiplies this by the number indicated to see the sensitivity of higher natural convection heat transfer coefficients.**

Heat Flux (W/m^2)	1x htc for Natural Convection	10x htc for Natural Convection	50x htc for Natural Convection	100x htc for Natural Convection
10^6	5E-4	4.5E-3	2.28E-2	4.55E-2
10^5	3.5E-3	3.55E-2	1.768E-1	3.513E-1
10^4	3.65E-2	3.623E-1	1	1
10^3	3.405E-1	1	1	1
10^2	1	1	1	1

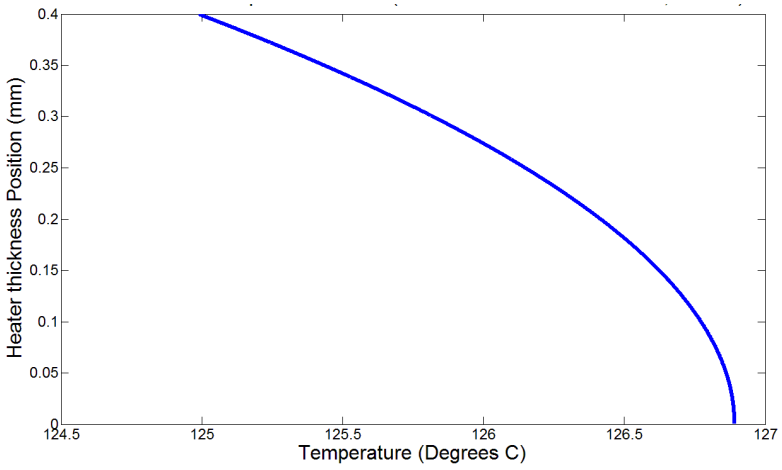

Figure 4-14: Temperature profile through the silicon heater for high heat flux of 10^6W/m^2 with the boiling heat transfer coefficient equal to 40kW/(m^2-K) and the natural convection heat transfer coefficient equal to 4.3W/(m^{2}K)

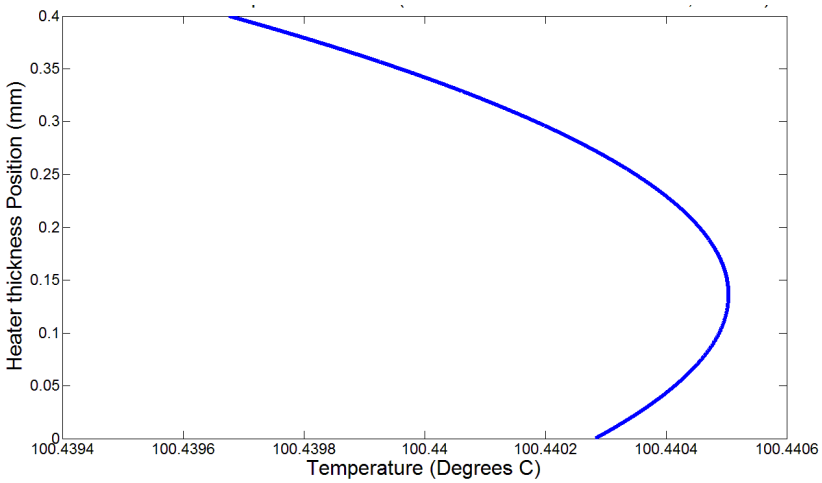

Figure 4-15: Temperature profile through the silicon heater for low heat flux of 1E3 W/m^2 with the boiling heat transfer coefficient equal to 1.5kW/(m^2-K)and the natural convection heat transfer coefficient equal to 4.3W/(m^{2}K).

4.2.11 Silicon heaters with electrically insulating coatings

Design numbers 11-13 from Table 4-2 can be lumped together in one description. All three designs use the same basic idea as number 10 described in section 4.2.10, but add different types of electrically insulating layers to minimize oxidation of the silicon. Therefore, these designs have the same assets and limitations described in 4.2.10, but with varying degrees of improvement of oxidation resistance.

Designs 11 and 12 have coatings that were applied to a clean wafer, then the wafer was cut to the appropriate size. Then gold electrodes were evaporated onto the back side of the silicon wafer to make the electrical connections. The first insulating coating is silicon nitride. This is a coating routinely used in silicon wafer processing. The thickness is ~200nm thick and silicon nitride has a dielectric strength of about 10^7V/cm [35], so the coating should be able to withstand a potential of up to 200V. The second coating is hydrogen silsesquioxane more commonly known as HSQ. HSQ is a photo resist used in silicon wafer processing. This coating

is slightly thicker ~1μm. The HSQ can also be annealed to allow it to cross link in to silicon dioxide, both annealed and unannealed samples were tested with very similar results.

These coatings were spun on so there is the possibility that the smoothness of the silicon wafers could be affected by this process. The Olympus LEXT OLS3000 Confocal Scanning Laser Microscope at Schlumberger-Doll research center was used as well as the JEOL 6320F in the CMSE shared user facility at MIT. The surfaces of both were smooth and below the resolution of confocal microscopy. The HSQ coating had a smooth surface at the nanoscale but had a periodic change in height of ~2μm over a distance of several hundred microns. This is presumably a wave created by the spinning process, but the size scale is large compared to that important for nucleation and should be inconsequential. The SEM images did not show any surface characteristics of interest.

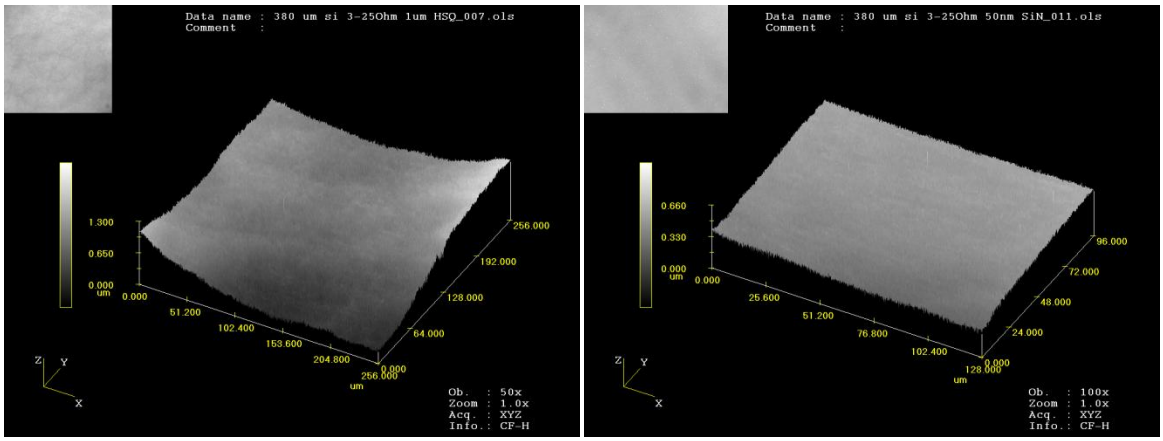

Figure 4-16: Confocal Image of HSQ surface [Left]. While smooth on the nm level there are slow changes in the height over hundreds of um. Confocal image of Si_3N_4 surface [Right]. The surface is very smooth with a SRa of ~10nm at the threshold of the instrument

These heaters after testing are shown in Figure 4-17.

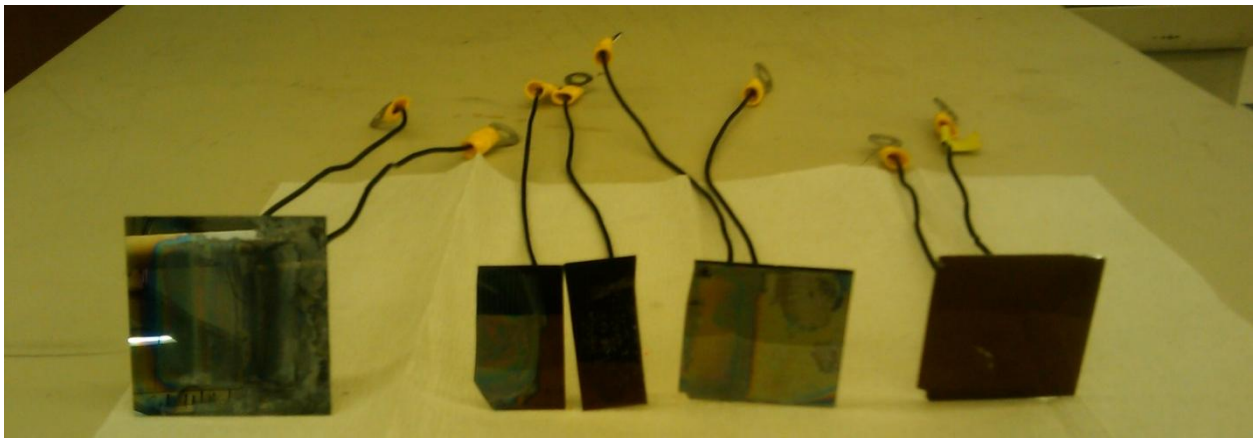

Figure 4-17: **Silicon Heaters coated with dielectric coatings. From Left to right, positive electrode is on the left for each heater. 1) Uncoated heater after boiling, large amount of discoloration and deposition 2) Si_3N_4 heater after test. Some dissolution of the coating on the positive electrode and some aluminum deposition on negative electrode 3) HSQ heater after test slight discoloration on positive electrode, no visible deposition. 4) Clean untested Si_3N_4 heater. The Si_3N_4 coating causes the brown discoloration. None of the coatings affected the quality of the IR images.**

The post testing silicon nitride heater shown in Figure 4-17 reached voltages of ~150V, which is getting close to the calculated dielectric strength of 200V calculated for the coating. Therefore, a

longer boiling test at a lower voltage was performed to see if the high voltage was responsible for the dissolution of the coating. This is shown in Figure 4-18, and it can be seen that the coating still dissolves just as shown in Figure 4-17, and there is deposition on the negative electrode.

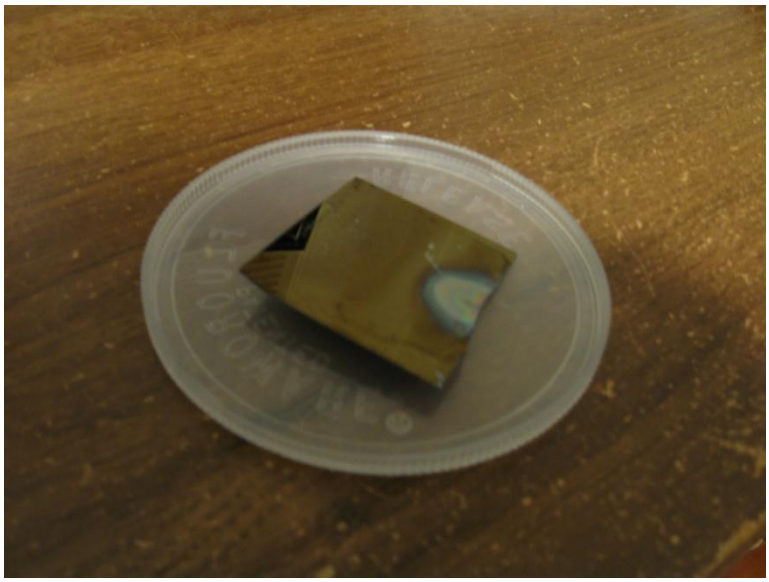

Figure 4-18: Si_3N_4 coated heater tested at 35V for 1 hour. The Si_3N_4 layer dissolved around the positive electrode where the vigorous boiling took place and there was some deposition on the negative electrode.

EDS was performed on the deposits on the heater to determine if there was anything present besides silicon and oxygen. The resulting spectrum is shown in Figure 4-19. The only two additional elements that are present are aluminum, which results from contamination from the boiling facility, which is composed of aluminum, and magnesium, which also is likely an alloying component from the aluminum facility.

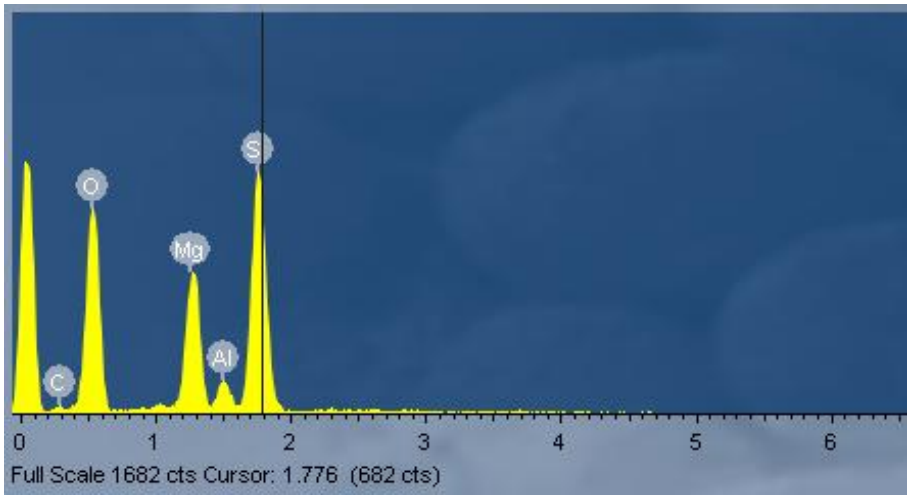

Figure 4-19: EDS spectrum from deposition spot on silicon nitride coated heater.

Design 13 in Table 4-2 uses what is known as a SOI wafer. This wafer is made up of a silicon dioxide layer that is sandwiched between two silicon wafers. The advantage of this wafer is that the back silicon wafer could be used for the resistive heating, while the top silicon layer could be the boiling surface with no electrical potential because of the insulating silicon dioxide layer that is between the two silicon layers. This design was not tested because of the expense of buying a box of these specialty wafers. However, a scrap section of a low resistivity SOI wafer was obtained and tested for IR visibility and it performed poorly. It is possible that other SOI wafers with different processing techniques could perform better in IR transparency, but wafer vendors do not report or guarantee optical properties of silicon wafers.

4.3 Other Experiment Design Change Possibilities

4.3.1 Operating with a positive DC ground

The power supply uses a floating potential split across the ground potential. There is the possibility to run with the positive terminal tied to ground potential so that the power supply operates at a potential below ground. This could potentially reduce oxidation since the positive

terminal where oxidation would occur would already be at a ground potential; however, there would still be a potential difference across the heater. When this was attempted both samples failed at very low heat fluxes, one sample is shown in Figure 4-20.

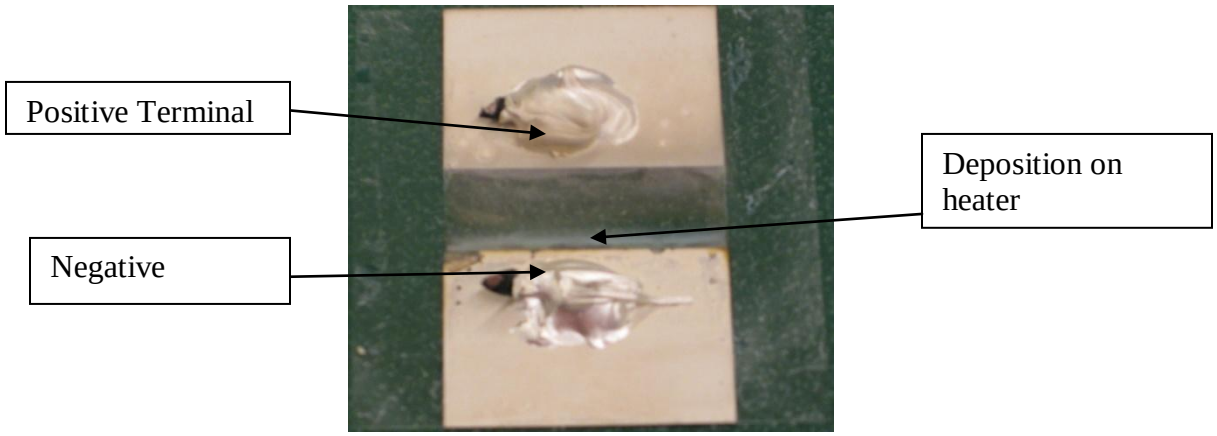

Figure 4-20: Heater after failure in positive ground test. Notice blistering and corrosion on negative electrode.

The electrical connection was severed, but the substrate remained intact. The positive terminal was relatively clean with just some deposition of impurities, but the negative terminal had excessive hydrogen and oxygen production that destroyed the electrical connection at the negative terminal. There was blistering on the negative electrode (possibly from hydrogen absorption) and corrosion at the negative electrode interface with the ITO as shown in Figure 4-20. The corrosion may have been accelerated from hostile local conditions caused by the electrolysis of water.

4.3.2 Using AC current for joule heating

Using AC current instead of DC current has the potential to minimize corrosion if the current alternates faster than the time constant for the oxidation reactions. AC current had some effect on the corrosion rate of the heater, but there was still oxidation and deposition. In addition, the alternation of the current caused large temperature variations (~5°C) on the heater

surface as the current cycles. This temperature oscillation creates a situation where boiling is not at steady state because the heat flux is not constant when looking at the time scale of the current frequency. This frequency (60Hz) is also slower than what bubble departure frequencies can achieve (120Hz and above).

4.3.3 Use of an inert fluid

The possibility of using a different working fluid other than water would be one solution to the oxidation of the silver pads. Another fluid such as ethanol [38], ethylene glycol [39], or a refrigerant [13] could be used instead of water, and minimize if not prevent all of the oxidation reactions.

However, refrigerants and solvents have low contact angles on most materials, so it would be difficult to see the effect of the contact angle changing on the CHF. Furthermore, water is the most typical heat transfer fluid.

4.3.4 Introduction of an additional inner bath for cleanliness

The fact that aluminum will deposit onto the heaters such as shown in Figure 4-19 illustrates the need for better cleanliness controls in the boiling facility. It is very difficult to ensure that there is always a passive layer on the aluminum facility, so it makes sense to use a different material for an inner bath that will not oxidize, is not porous, optically transparent, and easy to clean. To meet this requirement square borosilicate glass tubing of 49mm OD and 45mm ID (VitroCom S-145-1FT) was used to create a bath that encompasses the sapphire substrate, and creates a boiling chamber that is isolated from the aluminum in the boiling facility. The square tubing was cut to size using a tile saw to the maximum height possible to be accommodated by the boiling facility, approximately 5 3/8". This tubing was then set on top of a prepared heater

and was sealed from the outside with high temperature RTV silicone. The sealing from the outside minimizes water contact area with the silicone to minimize any leeching from the silicone sealant.

4.4 Final Design Selection

The final design selection is a version of the heater described in section 4.2.7 for the inverted ITO and sapphire heater. Ultimately, this design was chosen because it had no issues with corrosion, as it is electrically insulated from the water, which allows for very careful control of the surface. Control of the surface is important for testing engineered surfaces to ensure the modifications made to the surface are responsible for boiling behavior changes, and not from contamination that is depositing on the surface. This design also allows for acceptable IR images as well as having the potential for HSV to be taken.

The thickness of the sapphire was reduced from the reference design thickness of 0.4 mm to 0.25 mm, which was the thinnest economical sapphire available. This thickness reduction allowed for improved IR images by increasing the transmitted temperature wave from ~12% to ~25% for 120 Hz bubble departure frequency as shown in Figure 4-9.

The width of the heater was also reduced from 3cm in the reference design to 2cm. This reduction reduces the current necessary for the same heat flux by 1/3 and ensures that the power supply will not limit the ability to reach CHF (maximum of 20A) in case of any large enhancements. This changes the resistance of the heater. The resistance of the ITO coating is 10Ω/square, so with two squares in parallel (2cmx1cm) the theoretical resistance is 5Ω as shown in Eq. 4-9. The actual resistance of the heaters can vary from about 5.5Ω to 7Ω.

$$R_{parallel} = \left(\sum \frac{1}{R_i}\right)^{-1} = \left(\frac{1}{10} + \frac{1}{10}\right)^{-1} = 5\ Ohms \qquad \textbf{Eq. 4-9}$$

Where R_i are each of the resistances in parallel (Ohms). Also, the narrower heater provides more clearance in both the boiling facility and when using the additional inner bath as described in section 4.3.4, which was also utilized in the final design. The drawing of the heater and a picture with leads attached and the borosilicate inner bath is shown in Figure 4-21.

The DC supply was used instead of an AC supply since there was little difference in the corrosion rate, and the AC supply lead to temperature variations as the current oscillated. The DC supply was used with a floating potential instead of a positive ground because of the problems related to operating with a positive ground that were described in section 4.3.1. Water was chosen as the working fluid to more closely mimic engineering heat transfer systems, and to provide a measureable difference in wettability instead of using a well wetting fluid. Furthermore, since a design was chosen where corrosion was not an issue, there was not any motivation to change the fluid away from water.

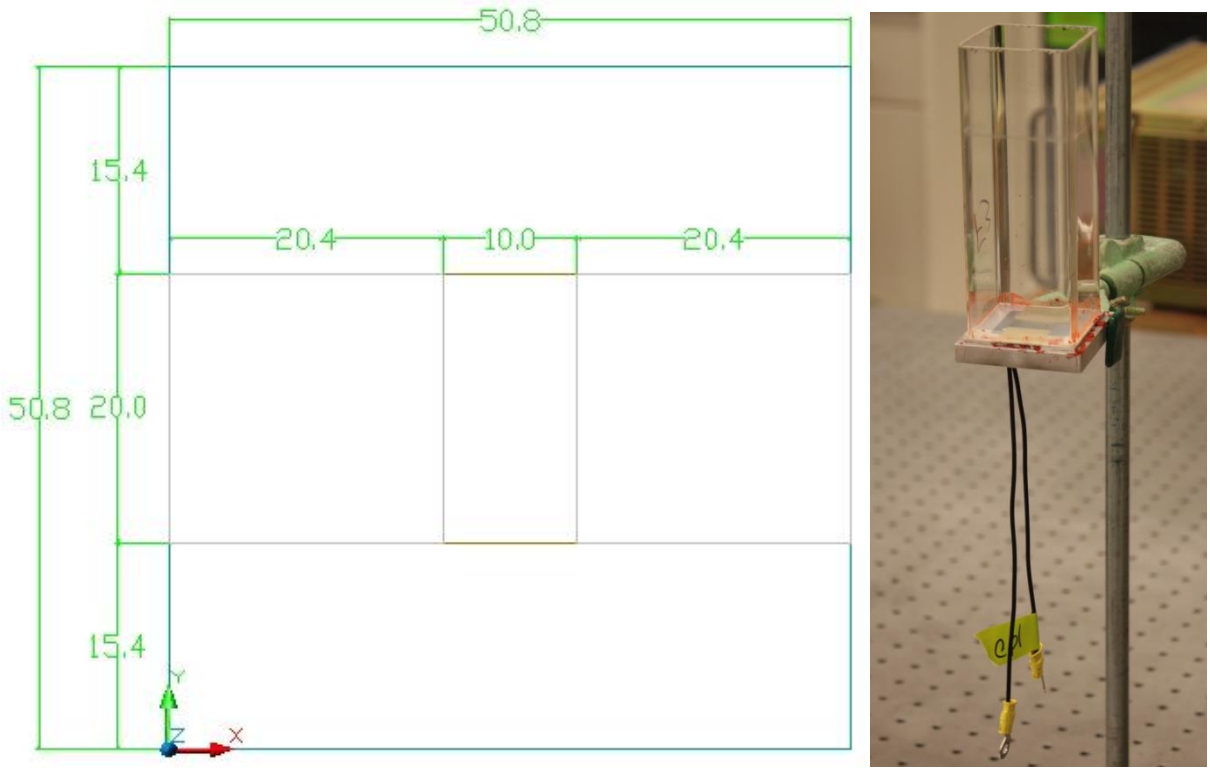

Figure 4-21: Drawing of the heater design used (left), dimensions are in mm and the sapphire is 0.25mm thick. The heater electrical leads and the inner bath attached (right).

5 Separate Effect Pool Boiling Experiments

The separate effects on boiling of several different surface characteristics are analyzed using LbL thin film coatings. First, the effect of different particle sizes used for the coatings is explored. Then the effect of different coating thicknesses and the effect of hydrophobic vs. hydrophilic surfaces are explored. The surfaces for each of these cases are characterized to determine the roughness, layer thickness, and porosities of the surface. The best features of the separate effects will then be utilized to create an optimized surface that contains the optimal nanoparticle size, bilayer thickness, and surface wettability features to give the best heat transfer characteristics.

5.1 Multilayer Preparation

The multilayers (see section 3.2) were prepared in the laboratories of Professor Rubner at MIT. Four different silica nanoparticle sizes were used of 7nm (Aldrich LUDOX SM-30), 20nm (Aldrich LUDOX TM-40, 50nm (Polysciences Silica Microspheres CAT#24040), and 100nm (Polysciences Silica Microspheres Cat#24041). The nanoparticle solution was prepared by creating a 0.03wt% solution of each nanoparticle size in the solution diluted in a pH 9.0 buffer. The pH 9.0 buffer was made in the laboratory and had the composition below.

Table 5-1: Composition of pH 9.0 buffer solution. When preparing the solution solid NaOH was used exclusively.

3.1 g/L boric acid
3.7 g/L KCl
0.86 g/L NaOH **or** 21.5mL NaOH 1N solution

Then NaCl was added to bring the solution to a concentration of 0.1M NaCl. The NaCl creates an ionic interference during the adsorption process and yields a multilayer with a higher

roughness. The nanoparticle solution was then placed on a stir plate for approximately 1 hour or until all of the NaCl had dissolved. The PAH solution was prepared by making a 10^{-2}M solution of PAH. This solution was then pH corrected to 7.5 with 1N NaOH.

The multilayers were then created using a Zeiss HMS Programmable Slide Stainer that is shown below.

Figure 5-1: Zeiss HMS Programmable Slide Stainer "Wilma". This particular dipper has been modified with large 1L baths positioned on top of stir plates.

This particular stainer was chosen because it both supports large substrates with the 1L baths and has the ability to use stir bars on the solutions to keep a uniform concentration. This agitation is important because some of the coatings are 100 bilayers thick, which takes over two days for

dipping to complete, and non-uniformities can occur in the coating if the solutions are not agitated.

To create the bilayers the heaters are first rinsed with ethanol on the sapphire only side, and then rinsed with DI water on both sides. The heaters are then clipped to the dipping arm of the dipper and properly positioned in height to keep the clips out of the solution while dipping while still dipping the entire heater area. The dipping sequence used for one bilayer is shown below, and this process was repeated for the desired number of times for the coating thickness desired.

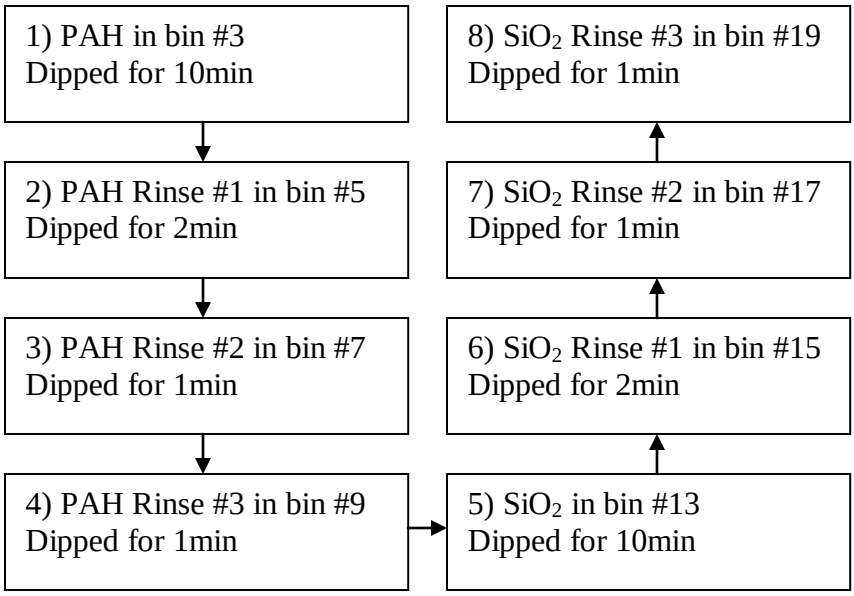

Figure 5-2: Dipping sequence and details for SiO_2 multilayers. The first number indicates the sequence followed by the contents of the bin, and in which bin it is located. The Rinse bins are all filled with DI water. The second line has the residence time of the samples in the solution. One sequence represents a single bilayer, the process is then repeated for the desired number of bilayers.

After the completion of the dipping the heaters are allowed to dry overnight before the contact angle is measured or any further processing is done on the sample. The samples may be treated with fluorosilane (1H,1H,2H,2H-perfluorodecyltriethoxysilane) to make the samples hydrophobic using a procedure used by Bravo et al. [25]. The fluorosilane layer is vapor

deposited by placing 0.5 ml of the fluorosilane in a sealed PTFE container in an oven at 140°C for 30 minutes. The PTFE container is then removed, the sample that is desired to be coated is placed in the container, and the PTFE container is returned to the oven for an additional 30 minutes. The coating is then allowed to dry overnight prior to measuring the contact angle. This coating is a monolayer and does not affect the topography of the sample, but merely bonds to the SiO_2 to change the surface energy of the particles.

5.2 Pool Boiling Facility

The pool boiling facility is an aluminum concentric bath design that is open at the bottom of the central bath to allow for the placement of the sapphire heater with optical access. The outer isothermal bath has a 1500W pre-heater that brings the experiment up to temperature and maintains the entire facility at saturation conditions throughout the experiment.

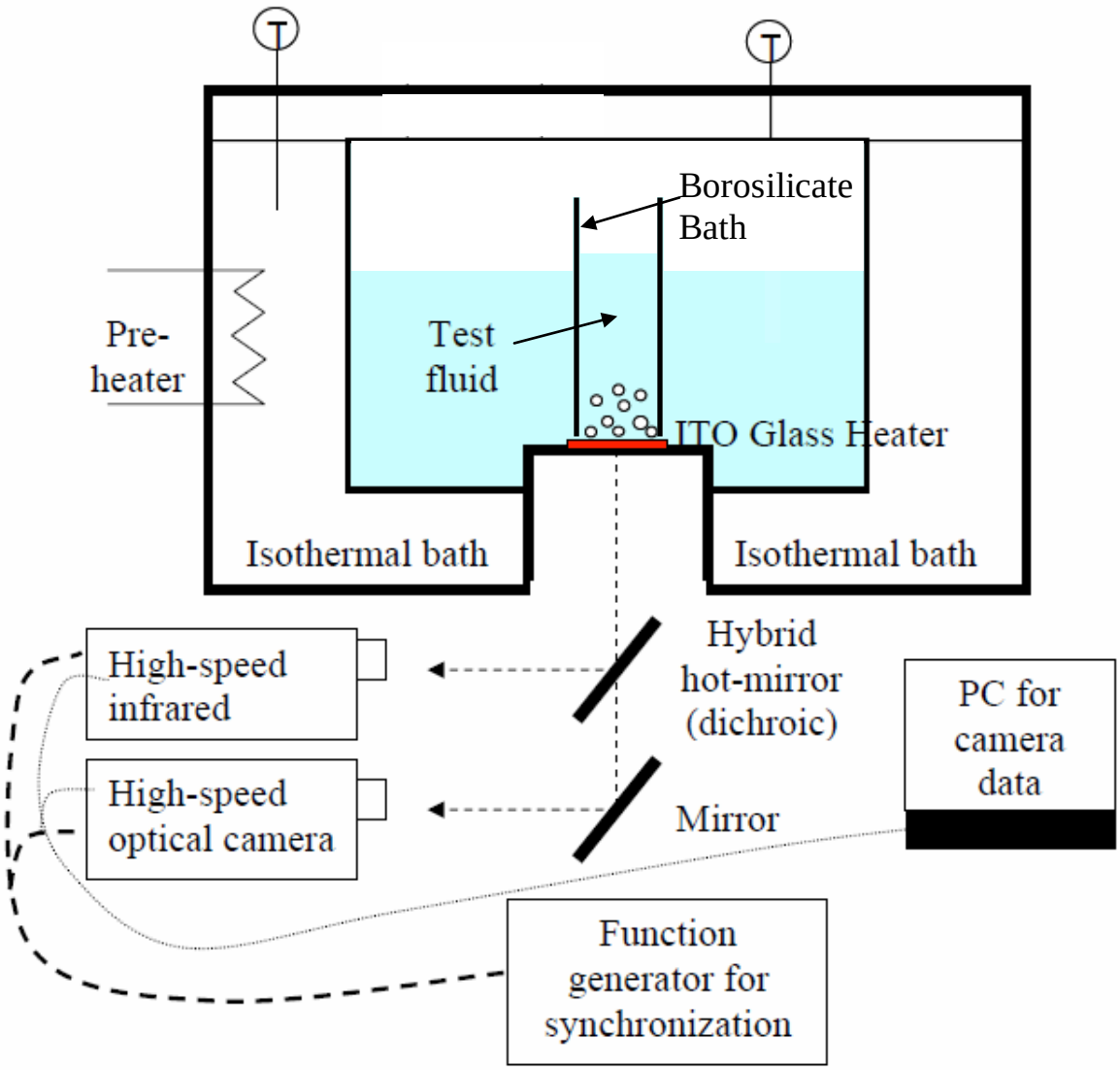

Figure 5-3: Schematic of the pool boiling facility modified from Ref. [34].

The boiling facility is diagramed in Figure 5-3. For complete dimensions and details of the boiling facility see reference [34]. For most experiments the hybrid hot mirror was not used and a gold mirror was used in its place to reflect the IR signal to the high speed IR camera. The IR camera used was a FLIR SC6000 with a 100mm lens and 0.75 inches of extension rings.

There were a few modifications to the facility to allow for testing of an inverted heater and to accommodate the borosilicate bath. First, a nylon plate was placed on the aluminum inner bath

before placing the inverted heater in the facility. This plate provided for electrical isolation from the aluminum facility since now the silver pads are facing down. Long threaded rods were added to the facility to allow for a clamping of the borosilicate bath and to place a vented Viton® lid on the top of the facility to minimize splashing from the borosilicate bath. A silicone gel gasket is used to seal the space between the nylon plate and the aluminum facility as well as between the nylon plate and the back of the heater. These silicone gel gaskets are isolated from the boiling test fluid. The connections to the silver pads are made with a silver conducting epoxy and high temperature wire. These leads are then connected to an Electronic Measurements, Inc. TCR DC power supply rated at 250V and 20A. A gold mirror is then placed below the facility. A picture of the experimental setup used with an inverted heater is shown in Figure 5-4. An Agilent Technologies 34980A Data Acquisition System is used to measure the voltage across the heater terminals, the current from the power supply using a shunt resistor, and the temperature of the heater, and the temperature of the middle bath. From this information the power and heat flux are calculated for the heater to allow monitoring of the experiment.

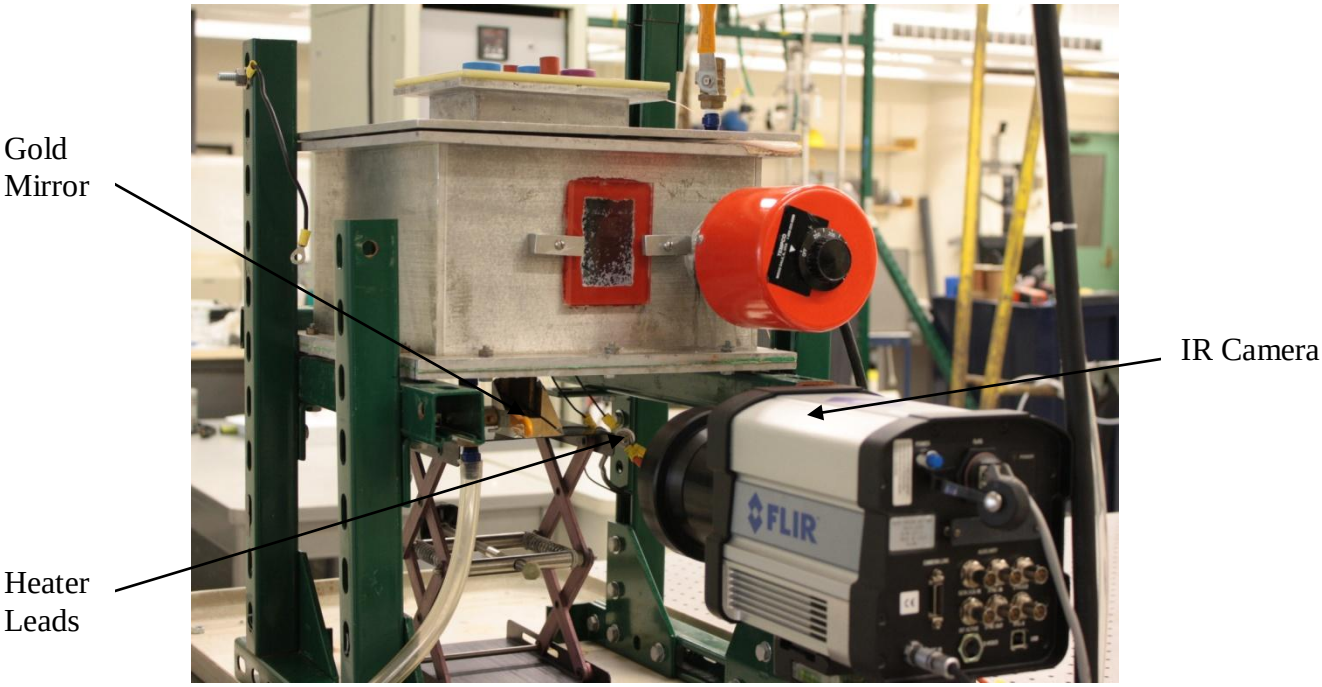

Figure 5-4: Photograph of the pool boiling facility as configured for inverted experiments. Heater leads are not insulated for clarity.

5.3 Pool Boiling Procedure

5.3.1 Sample preparation

The sapphire surface was processed to give it the desired features for the boiling test of interest. The silver pads were then rubbed with a dry cotton swab to remove any coatings and oxidation from the silver pad for an area of about 1 cm from the ITO. There is a slight color change indicating that fresh silver is being exposed. This ensures that the conductive silver epoxy makes a good mechanical and electrical bond with the silver pad. Leads are then affixed to the heater using a conductive silver epoxy. The heaters and epoxy then are allowed to cure overnight. After curing is completed the leads are bent at about a 90 degree angle. The heater is then placed in a stand that allows for the leads to hang free while the periphery of the heater is setting on a surface. Any extra silicone left on the borosilicate bath from previous experiments is

removed and the borosilicate bath is then cleaned three times in isopropanol and rinsed three times with DI water. The borosilicate bath is then centered onto the heater and the bath is sealed to the heater from the outside with high temperature RTV silicone. The silicone is allowed to cure for a minimum of 2 hours. Then the heater surface is rinsed with DI water using a wash bottle. The back of the heater surface is cleaned with DI water and a cotton swab to remove any coatings from the back of the heater that could affect the IR signal. If a temperature calibration is going to be performed a thermocouple is placed on the back of the heater covering about half of the active heater and leaving half to be imaged with the IR camera.

5.3.2 Sample mounting and experiment assembly

The gel gasket described in section 5.2 is placed on top of the nylon plate. The heater with the borosilicate bath is then lowered into facility and pressed to seal against the gasket. The borosilicate bath is then filled with DI water, the Viton® vented cap is placed on top and the heater is gently secured with nuts and a top plate to provide even pressure. The bath around the borosilicate bath is then filled with DI water and the outer isothermal bath is filled with tap water. The pre-heater is then turned on and a thermocouple is placed in the middle bath outside the borosilicate bath and the experiment is allowed to reach saturation. While heating up the electrical connections are made to the DC supply as well as to the Agilent system. The gold mirror is then placed under the facility to reflect the image to the IR camera. . The camera preset for 50-150°C for the 100mm lens is selected. This preset covers the range of temperatures of interest while maintaining an acceptable number of counts at the low range. The actual temperatures covered for the heater by this preset are closer to 80-200°C based on the emissivity of the ITO. The IR camera is then properly oriented and a single point temperature correction is

performed using a black body emitter at about 100°C to equalize the response across all of the camera pixels.

5.3.3 Taking temperature data

When the facility reaches saturation the DC power supply is turned on and the heater is brought to a heat flux of 300kW/m^2 and allowed to degas for 20 minutes. If a temperature calibration is being performed the temperature is read from a thermocouple while taking IR images for calibration while increasing the heat flux. The thermocouple on the back of the heater is then removed prior to taking data. The DC supply is then shutdown and the experiment is allowed to sit for 8 minutes to allow the temperature to cool down to equilibrium. Then the power supply is energized and stable heat fluxes are obtained and IR movies are recorded. When in the natural convection regime the experiment takes about two minutes to reach thermal equilibrium, but once nucleate boiling begins equilibrium is reached in seconds. However, a minimum of 30 seconds is waited to allow the experiment to come to equilibrium. When approaching the CHF longer videos are recorded while increasing the heat flux to attempt to capture the CHF event. After CHF is reached the power supply is shutdown, the pre-heater is turned off, the Agilent system data acquisition is halted, the water from the experiment drained, and the heater sample is removed and stored.

5.3.4 Temperature calibration

IR images are taken at different temperatures as described in the above sections. The average counts for all of the pixels over the visible part of the heater for all of the frames is computed using a MATLAB script excepting a 1mm around the edge of the heater. This is used to generate a linear calibration curve of pixel counts to temperature. The slope of the temperature calibration is very consistent from experiment to experiment, but the bias changes

slightly. Therefore, even if a calibration is not performed for a specific experiment, the data can still be fit to a curve because the initial temperature at a heat flux of 0 kW/m^2 is known, which can be used to compute the bias for the experiment.

The temperature being read by the IR camera is the temperature on the back of the heater away from the boiling surface. Therefore, the surface temperature was calculated using the input heat flux and using the thermal resistance for an infinite 1D slab as shown below.

$$\Delta T = q'' \frac{a}{k} \qquad \textbf{Eq. 5-1}$$

Where ΔT is the temperature drop from the back of the heater to the front, q" is the heat flux (W/m^2-K), a is the heater thickness (m), and k is the thermal conductivity of sapphire (W/K-m).

5.3.5 Facility Benchmark

The facility had previously been benchmarked considering both CHF and the heat transfer coefficient from Gerardi's work [34]; however, significant changes were made to the heater compared to that work, so a second verification is necessitated. Using the Zuber correlation for CHF from Eq. 2-6 yields a CHF value of 1107kW/m^2 for the conditions of the facility while Gerardi's work for pure water had an average CHF value of 976kW/m^2 compared to 907 kW/m^2 using the new heater, a 7% smaller value. A benchmark with a 0.1vol% silica nanofluid diluted from Ludox 37wt% silica nanofluid that was also tested by Gerardi was used to benchmark the CHF enhancement of the new heater. The 0.1vol% silica nanofluid was boiled for 15 minutes at 300 kW/m^2 for degassing similar to the other heaters tested and then the test for the CHF took approximately an additional 30 minutes. Gerardi measured a CHF value of 1767kW/m^2, while the new heater had a value of 1726kW/m^2 a 2% smaller value. Thus the maximum difference from the old design is 7% or less. Furthermore, the heater is thinner than

that used by Gerardi, and therefore can be expected to have a slightly lower CHF due to inability of the heater to store and conduct heat away from hot spots. This can be quantified by the parameter known as thermal activity, S, which is given below [2].

$$S = D\sqrt{\rho c k} \qquad \textbf{Eq. 5-2}$$

Where D is the characteristic dimension (in this case the heater thickness in m), ρ is the density (kg/m^3), c is the specific heat (J/kg-K), and k is the thermal conductivity of the heater material (W/K-m). According to Arik [40], for values greater than 8J/(m-K-s$^{1/2}$) there is no further influence from the heater being thicker. The value changes linearly with thickness and for Gerardi's heater the value was 3.82J/(m-K-s$^{1/2}$), and for the new heater it is 2.34J/(m-K-s$^{1/2}$). This is a significant change of over 30%, which provides an explanation of the lower CHF values given the relationship between thermal activity and the maximum CHF shown below[40].

$$\frac{q_{CHF}}{q_{CHF,\max}} \propto \frac{S}{S+0.8} \qquad \textbf{Eq. 5-3}$$

This ratio is 0.827 for Gerardi's heater and is 0.745 for the new heater. Therefore, one would expect about a 10% lower CHF for the new heater, which agrees well with the experimental value of 7% lower.

The CHF enhancement from Gerardi's results using 0.1vol% silica nanoparticle solution was 84%, and the new heater design had a similar enhancement of 90% using 0.1vol% silica nanoparticle solution.

Table 5-2: Benchmarking of CHF values of new heater design compared to that used by Gerardi [34] and those predicted by Zuber [1].

Test Name	CHF (kW/m^2)	Average CHF (kW/m^2)	CHF Spread Percentage	CHF Standard Deviation Percent	% Deviation From Gerardi [34]	% Deviation from Zuber [1]
Clean Heater-6	920					
Clean Heater-7	986					
Clean Heater-8	799					
Clean Heater-9	885					
Clean Heater-10	947	907	21%	8%	-7%	-18%
0.1 vol%-1	1732					
0.1 vol%-2	1720	1726	1%	1%	-2%	N/A

5.3.6 Uncertainty Analysis

The heat flux uncertainty for the facility has previously been calculated by Gerardi and determined to be less than 2% [34] and is still valid for the experiments performed in this work. The effect of radial conduction in the heater was also determined to be negligible by Gerardi [34]. However, there is some additional uncertainty in the temperature measurements because the temperature is measured on the back of the heater and the temperature at the surface is then calculated.

The uncertainty in the thermocouple temperature measurement is 0.75% as quoted by the Omega [41]. The uncertainty of the temperature measurements from the SC6000 IR camera is 2% as quoted by the FLIR [42], however, it should be less than this due to the custom calibrations performed for the specific experimental setup.

The uncertainty in the temperature drop calculation is dependent upon the uncertainties of the different uncertainties used in Eq. 5-1 that calculates the temperature drop. The tolerance of

the thickness of the sapphire was measured by performing measurements on 8 samples and the average value was found to be 262μm ± 8μm or about 3%. The thermal conductivity tolerance is also not explicitly known, but can be approximated by using the amount of anisotropy in the thermal conductivity of sapphire for the different crystal orientations, which is about 3% [43]. The heat flux uncertainty was already reported above as 2%. Therefore, the total error in the temperature drop calculation can be determined using error propagation for multiplication of uncorrelated variables shown below [44]:

$$\frac{\sigma_{\bar{f}}}{\bar{f}} = \sqrt{\sum_i \left(\frac{\sigma_i}{\bar{x}_i}\right)^2} \qquad \textbf{Eq. 5-4}$$

Where $\frac{\sigma_{\bar{f}}}{\bar{f}}$ is the resulting relative error, and $\frac{\sigma_i}{\bar{x}_i}$ are the individual relative errors. The resulting error is 4.7%; however this applies to the temperature drop calculation, which is 100°C less than the absolute temperature which is plotted in the graphs, and the relative errors determined above. Correcting to the total temperature yields a maximum error of about 2% for the highest temperatures encountered, which is about 175°C. The interaction of the three errors associated with the temperature measurement from the camera, thermocouple, and calculation is difficult to quantify, especially since the thermocouple temperature error and the IR camera temperature error are correlated variables. However, the IR camera and thermocouple errors can be assumed to be a single measurement with an error of 2% and combining that with the error of 2% from the temperature drop calculation the resulting error can be calculated from the equation below [44] for uncorrelated variables that are added together.

$$\sigma_{\bar{f}} = \sqrt{\sum_i (\sigma_i)^2} \qquad \textbf{Eq. 5-5}$$

Taking 175°C as the temperature of interest the resulting error is about 2.8%, which should be a good estimate for the temperature error. These errors are not shown on the plots to keep the information clear.

5.4 Effect of Particle Size

5.4.1 Multilayer particle Size effect on CHF

To analyze the effect of particle size on CHF and the heat transfer coefficient, several different particle sizes were used to make the LbL coatings with 20 bilayers. The particle sizes used were 7nm, 50nm, and 100nm. Also, a layer was created using a combination of 20nm particles and 50nm particles. This coating had been used in other boiling studies [24], and was used as a comparison to the different particle sizes. A table of the different particle size experiments along with the clean heater data and the 0.1vol% silica nanofluid tests. The 0.1vol% silica nanofluid particles have an approximate mean diameter of 33nm [34]. A summary of the CHF results is shown below.

Table 5-3: CHF results for the various particle sizes with 20 bilayers compared to clean sapphire heaters and 0.1vol% silica nanofluid.

Test Name	CHF (kW/m^2)	Average CHF (kW/m^2)	% CHF Enhancement over Clean Heater	CHF Spread Percentage	CHF Standard Deviation Percent
Clean Heater-6	920				
Clean Heater-7	986				
Clean Heater-8	799				
Clean Heater-9	885				
Clean Heater-10	947	907	0%	21%	8%
0.1 vol% (33nm)-1	1732				
0.1 vol% (33nm)-2	1720	1726	90%	1%	1%
7nm 20bilayers-3	1107				
7nm 20bilayers-4	1085	1096	21%	2%	1%
50nm 20bilayers-1	1650				
50nm 20bilayers-2	1600				
50nm 20bilayers-3	1500	1583	74%	9%	5%
100nm 20bilayers-2	1342				
100nm 20bilayers-4	1400				
100nm 20bilayers-5	1490				
100nm 20bilayers-6	1297	1382	52%	14%	6%
20/50nm 20bilayers-1	1640				
20/50nm 20bilayers-2	1600				
20/50nm 20bilayers-3	1522	1587	75%	7%	4%

The first 5 clean heaters were used to refine the experimental procedure and setup, and are not reported here. Three other test had a low water level that caused erroneous results and are not reported those are the 7nm 20 bilayers test 1 and 2 and the 100nm 20 bilayers-1. Scanning the data the large enhancements came from 50nm, 100nm, and the mixture of 20nm and 50nm particles.

The CHF data spread was analyzed using Peirce's criterion to check for potential outliers in the data [45][46]:

$$\zeta_i = \frac{\left| q''_{CHF_i} - \bar{q}''_{CHF} \right|}{\sigma_{CHF}} \qquad \textbf{5-6}$$

Where q''_{CHF_i} is the CHF for each individual experiment (W/m2-K), $\bar{q}''_{CHF}$ is the average CHF for all of the tests (W/m2-K), σ_{CHF} is the standard deviation for all of the CHF tests (W/m2-K), and ζ_i is the dimensionless deviation ratio. For a series of three tests a deviation ratio (ζ_i) of 1.196 and above signifies an outlier [45]. All of the tests passed this except for the 100nm 20 bilayer coating test 3. This test was omitted and two extra tests were performed to confirm the results.

The 20/50nm coating enhancement of 75% is very close to Forrest's results [24], who used a similar coating (Forrest's coating received a heat treatment of 550°C for one hour to remove the PAH that the heater in this test did not), with wire boiling tests and got an enhancement of 63%. The highest enhancements are from the 20/50nm and 50nm coatings, and the enhancements are statistically the same.

5.4.2 Multilayer particle size effect on heat transfer coefficient

The boiling curves and heat transfer coefficients for a characteristic curve for each of the particle sizes with 20 bilayers are shown below along with those for the clean heaters and the 0.1Vol% silica nanofluid for comparison.

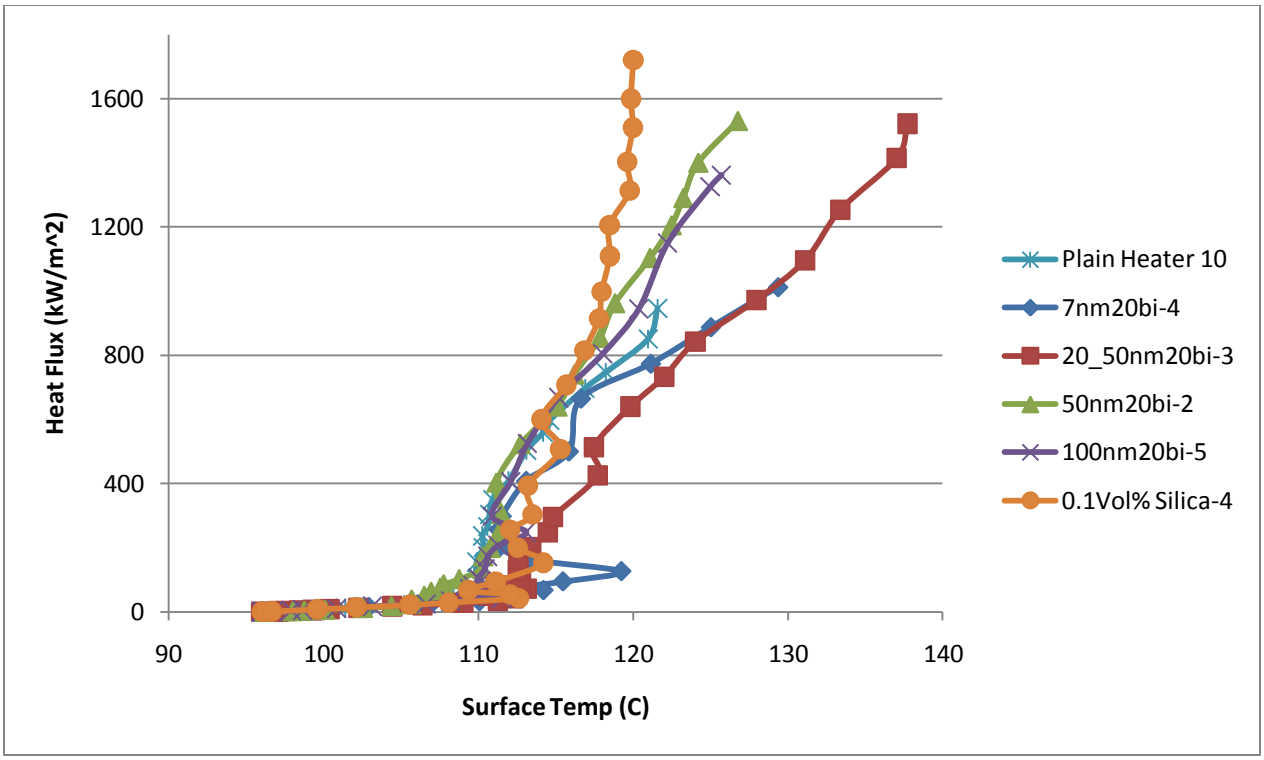

Figure 5-5: Characteristic boiling curves for each of the 20bilayer tests with a plain heater and 0.1Vol% silica nanofluid as a comparison.

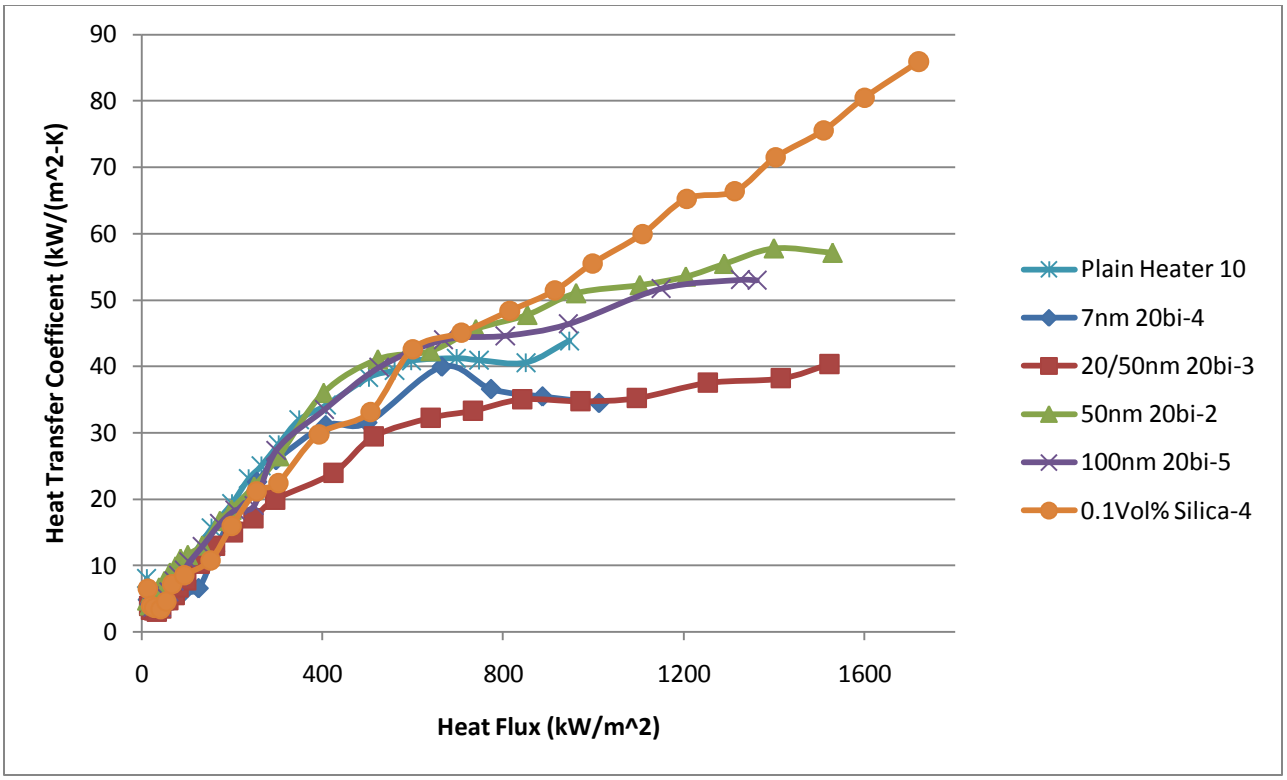

Figure 5-6: Heat transfer coefficients for characteristic boiling curves for each of the 20 bilayer tests with a plain heater and 0.1Vol% silica nanofluid as a comparison.

Examining the CHF values from the previous section and the above two figures it can be seen that the 50nm 20 bilayer coating has a comparable CHF to that of the 20/50nm 20 bilayer coating while the 50nm 20bilayer coating has a superior heat transfer coefficient. The 100nm 20 bilayer coating has a similar heat transfer coefficient to the 50nm 20bilayer coating but does not have as high of a CHF. This indicates that the 50nm 20 bilayer coating is the best choice to vary the coating thickness to see the effect of coating thickness on CHF and the heat transfer coefficient.

5.5 Effect of Multilayer Thickness

5.5.1 Multilayer thickness effect on CHF

The effect of the multilayer thickness was explored by increasing the coating thickness from 20 bilayers to 50 and 100 bilayers. The 50nm particle coating was chosen based on the results in the above section. The CHF results for the various layer thicknesses are shown in the table below.

Table 5-4: Summary of the CHF results for the various multilayer thicknesses. Clean heater results and 0.1Vol% silica nanofluid are shown for comparison.

Test Name	CHF (kW/m^2)	Average CHF (kW/m^2)	% CHF Enhancement over Clean Heater	CHF Spread Percentage	CHF Standard Deviation Percent
Clean Heater-6	920				
Clean Heater-7	986				
Clean Heater-8	799				
Clean Heater-9	885				
Clean Heater-10	947	907	0%	21%	8%
0.1 vol% (33nm)-1	1732				
0.1 vol% (33nm)-2	1720	1726	90%	1%	1%
50nm 20bilayers-1	1650				
50nm 20bilayers-2	1600				
50nm 20bilayers-3	1500	1583	74%	9%	5%
50nm 50bilayers-1	2030				
50nm 50bilayers-2	1800				
50nm 50bilayers-3	1770	1867	106%	10%	8%
50nm 100bilayers-1	1950				
50nm 100bilayers-2	2050				
50nm 100bilayers-3	1770	1923	112%	15%	7%

There is an increase in CHF of over 25% by increasing the layer thickness to 50 bilayers, there is a slight increase by increasing to 100 bilayers, but the increase is within the experimental standard deviation.

5.5.2 Multilayer thickness effect on heat transfer coefficient

The boiling curves and heat transfer coefficients for the multilayer thickness of 20 bilayers, 50 bilayers and 100 bilayers with 50nm particles are shown below.

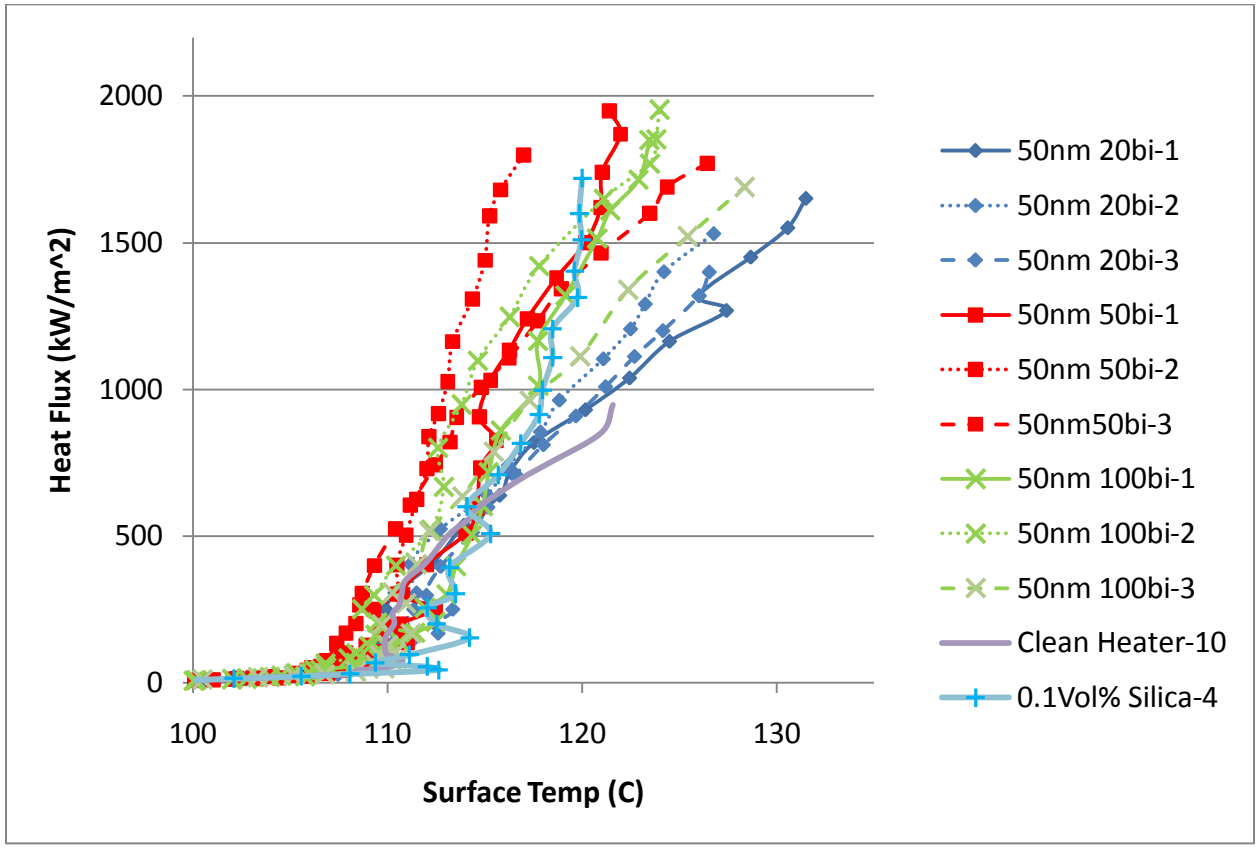

Figure 5-7: Boiling curves for various bilayer thicknesses of 50nm particles. The layer thicknesses are 20 bilayers (diamonds), 50 bilayers (squares), and 100 bilayers (X). A characteristic clean heater (smooth line) and 0.1Vol% silica nanofluid (+) are shown for comparison.

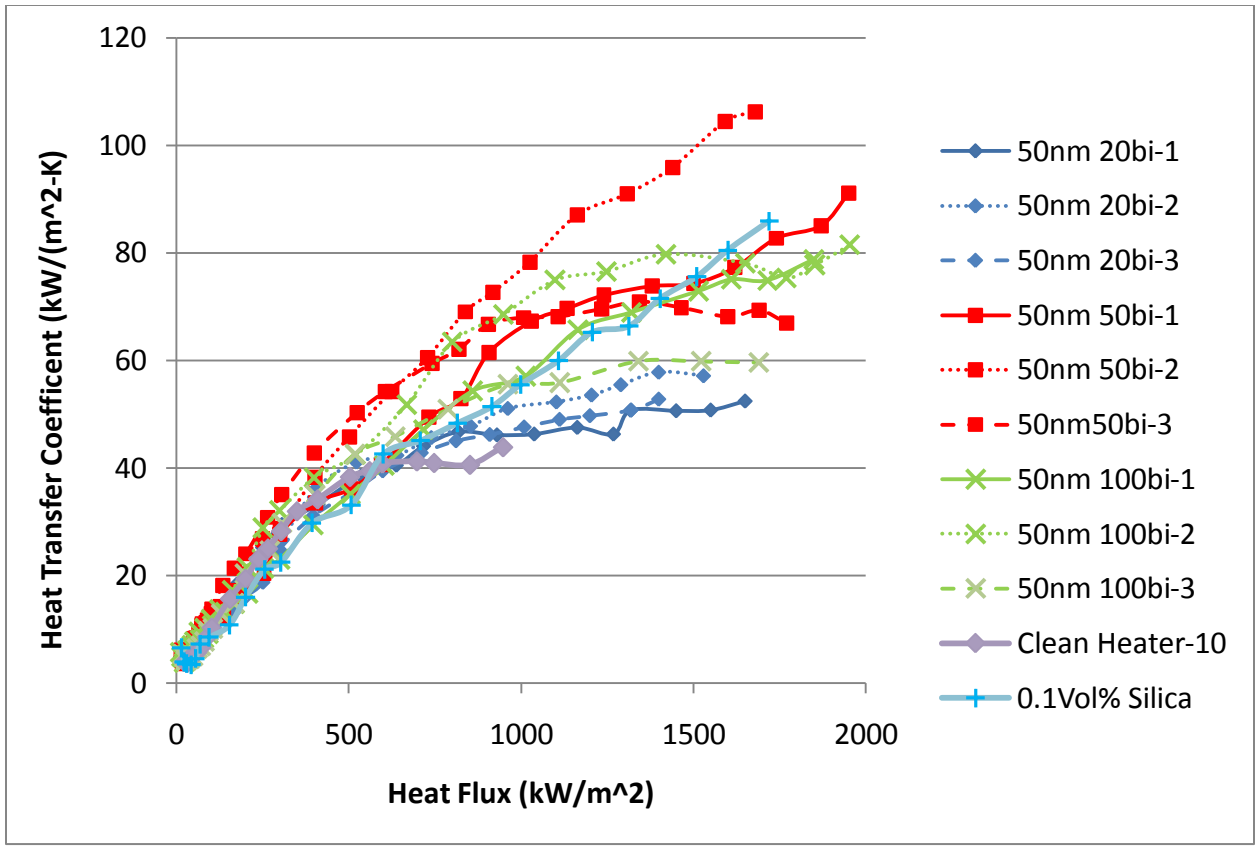

Figure 5-8: Heat transfer coefficients for various bilayer thicknesses of 50nm particles. The layer thicknesses are 20 bilayers (diamonds), 50 bilayers (squares), and 100 bilayers (X). A characteristic clean heater (smooth line) and 0.1Vol% silica nanofluid (+) are shown for comparison.

Even though the 100 bilayer case had a slightly higher average CHF than the 50 bilayer case, the 50 bilayer case (squares in above figures) on average has the best heat transfer coefficient. This is probably from the extra nucleation sites created by the additional layer thickness, while the layer still being thin enough to have a negligible thermal resistance. The 100 bilayer case thickness is calculated to be approaching 2.7µm, which is beginning to have a significant thermal resistance.

5.6 Effect of Multilayer Wettability

The 50nm 50 bilayer coating from the above section that exhibited the best combined enhancement in both CHF and heat transfer coefficient was used to make a superhydrophobic surface. This surface was then tested to see the effects on boiling. The boiling curves and heat transfer coefficients are shown below.

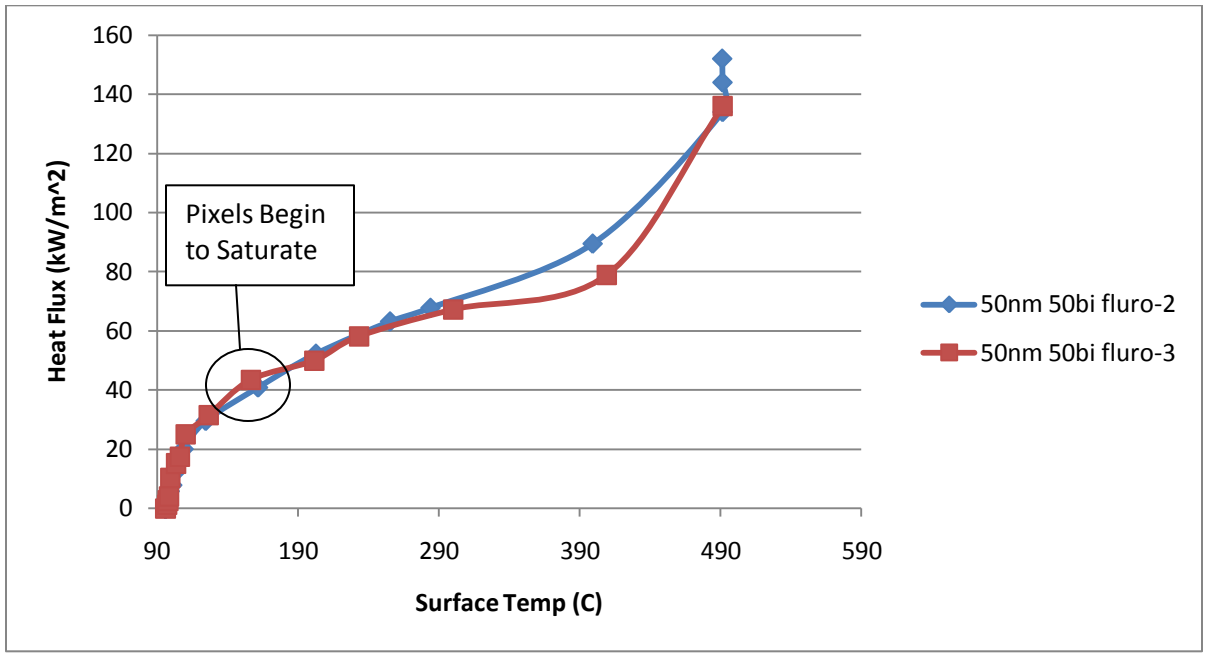

Figure 5-9: Boiling curves for 50nm 50 bilayers silica particles with fluorosilane coating creating a hydrophobic surface with a contact angle of approximately 140 degrees. The temperatures are averages and are sensitive to the area selected because of the large discontinuity in the surface temperature. The sensor begins to have saturated pixels at about 50kw/m^2 (which is essentially the CHF for this surface). Test 2 failed at 89 kW/m^2 and test 3 failed at 79 kW/m^2.

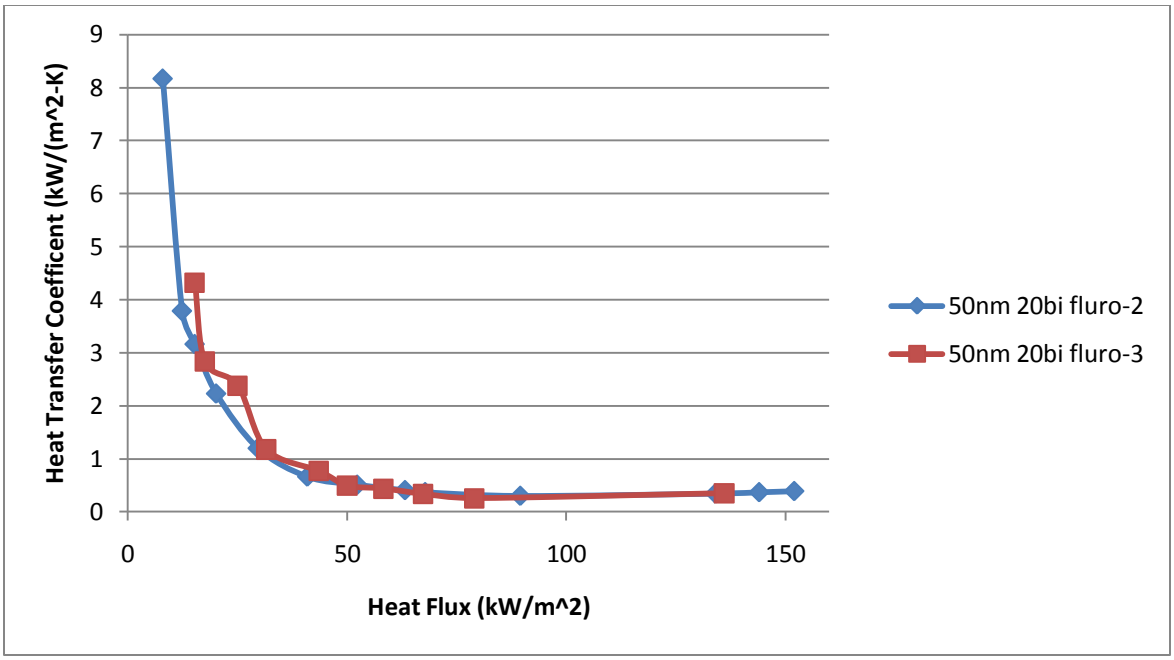

Figure 5-10: Heat transfer coefficient for fluorosilane coated 50nm 50 bilayer silica nanoparticle coating.

These surfaces hit CHF at a very low value because the surface was not able to be rewet during boiling, since the hydrophobic surface has a static contact angle of ~140 degrees versus 0-60 degrees for clean and multilayered surfaces.. These surfaces would never wet entirely. The first sample was destroyed because of the degas procedure of raising the heat flux to 300 kW/m^2 for the degas, and the sample was vapor blanketed and failed at about 100 kW/m^2 while ramping up to 300 kW/m^2. The degas procedure was modified for these surfaces by holding the sample at 30 kW/m^2 for 30 minutes. Visual inspection of the second sample showed that the sample surface was never fully wet by the water, and as the heat flux was increased a single site in the middle is all that would nucleate. Essentially it was film boiling, but not encompassing the entire heater. The liquid vapor interface never moved during the ebullition cycle, and the top of the film deformed to release a bubble. Therefore, there wasn't much time dependent behavior at a given heat flux in the IR signal. The liquid vapor contact line would stay constant at a given heat flux

and only grew as the heat flux was increased. This behavior is sketched below in Figure 5-11. The temperature profiles for different heat fluxes are shown in Figure 5-12

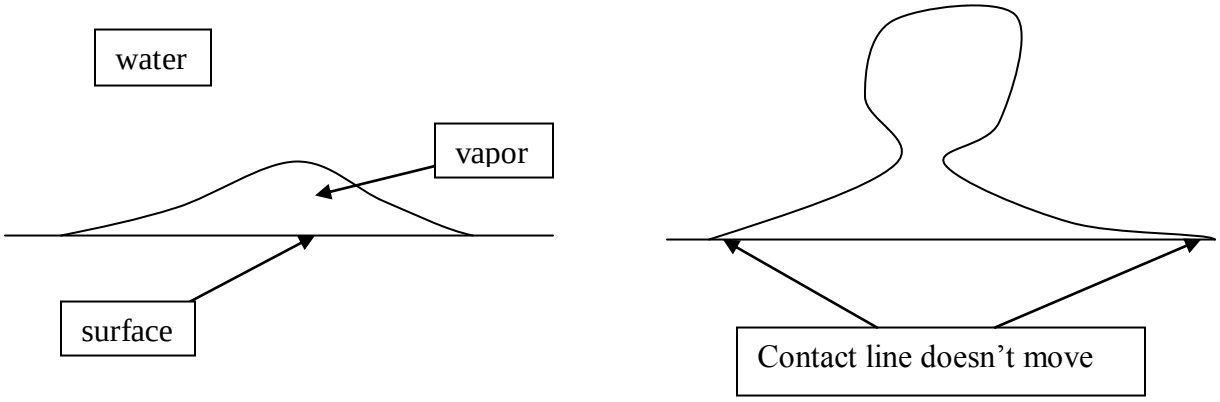

Figure 5-11: Depiction of quasi-film boiling that takes place on hydrophobic surface.

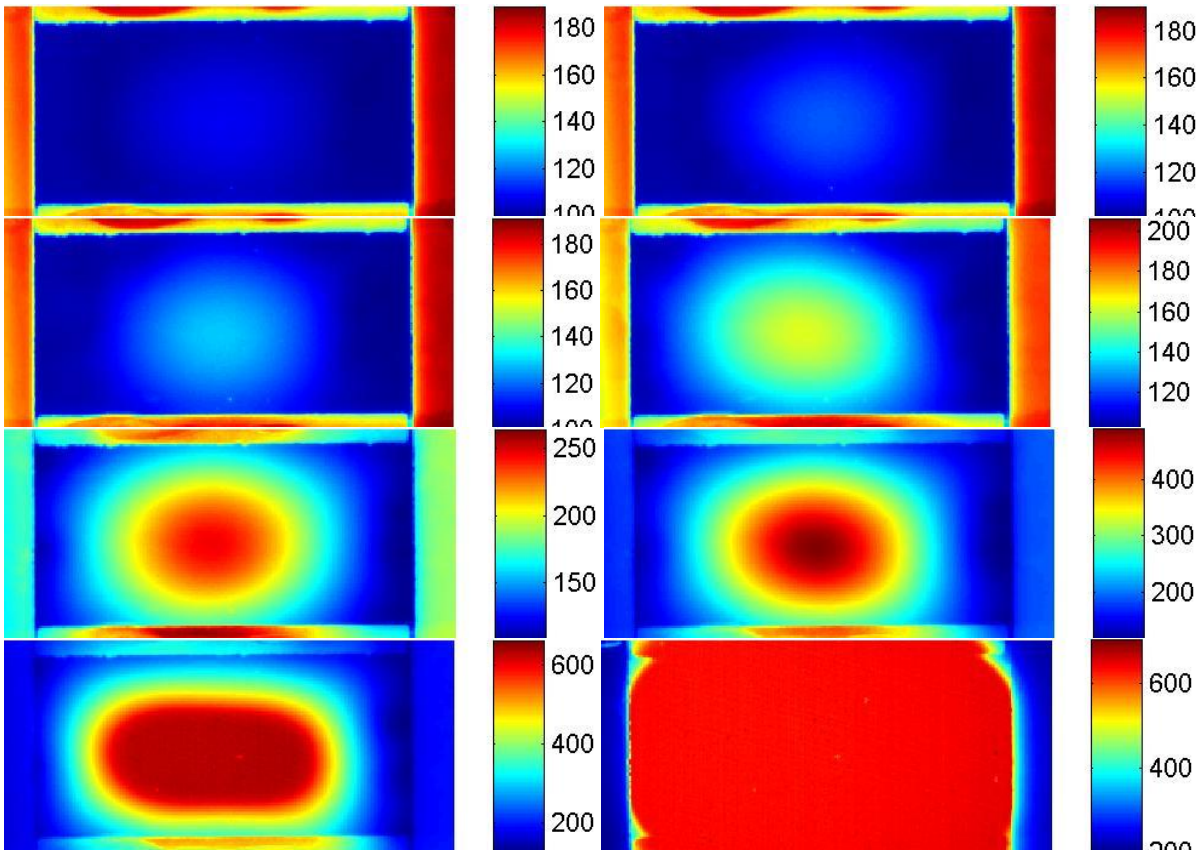

Figure 5-12: Increasing heat fluxes from left to right for 50nm 50bilayers with fluorosilane coating. Heat fluxes are 7.9, 15.2, 20.1, 29.6, 40.9, 63.2, 89.5, and 152 kW/m^2. 152 kW/m^2 was reached as a steady state after a temperature excursion which drove the resistance up to reach an equilibrium.

5.7 Characterization of Multilayers

The separate effects that were to be tested were particle size, bilayer thickness, and surface wettability. The important parameters of interest for the different multilayers are therefore surface roughness and morphology (measured with confocal microscopy and SEM), coating thickness (measured with spectroscopic ellipsometry), the porosity (measured with spectroscopic ellipsometry), and the contact angle (measured with goniometry). The confocal microscope used was the Olympus LEXT OLS3000 Confocal Scanning Laser Microscope at Schlumberger-Doll research, the SEM was the JEOL 6320F in the CMSE shared user facility at MIT, the spectroscopic ellipsometer is a J.A. Woollam Co., INC model XLS-100 at the Institute

for Soldier Nanotechnologies at MIT, and the goniometer is a CAM 101 contact angle analyzer and optical measurement software (KSV Instruments). The separate effect test matrix is shown in the table below.

Table 5-5: Separate effects test matrix to explore effects of particle size, layer thickness, and wettability.

Sample Parameters	Reason for Inclusion in Test Matrix
Plain Sapphire	Benchmark for facility and grounds of comparison for enhancements
Plain Sapphire with 0.1vol% silica nanofluid	Benchmark for facility by comparing to Gerardi's work [34]
Sapphire heater coated with 20 bilayers of 7nm particles	Explore effect of particle size
Sapphire heater coated with 20 bilayers of 50nm particles	Explore effect of particle size
Sapphire heater coated with 20 bilayers of 20nm and 50nm particles	Explore effect of particle size, and compare with Forrest's work [24]
Sapphire heater coated with 20 bilayers of 100nm particles	Explore effect of particle size
Sapphire heater coated with 50 bilayers of 50nm particles	Explore effect of particle thickness
Sapphire heater coated with 100 bilayers of 50nm particles	Explore effect of particle thickness
Sapphire heater coated with 50 bilayers of 50nm particles, and a fluorosilane coating	Explore effect of surface wettability

5.7.1 Silica nanoparticle layer roughness and morphology

The roughness was measured with an Olympus LEXT OLS3000 Confocal Scanning Laser Microscope by scanning an area of 128µm x 128µm at 100x magnification. The facility is shown below.

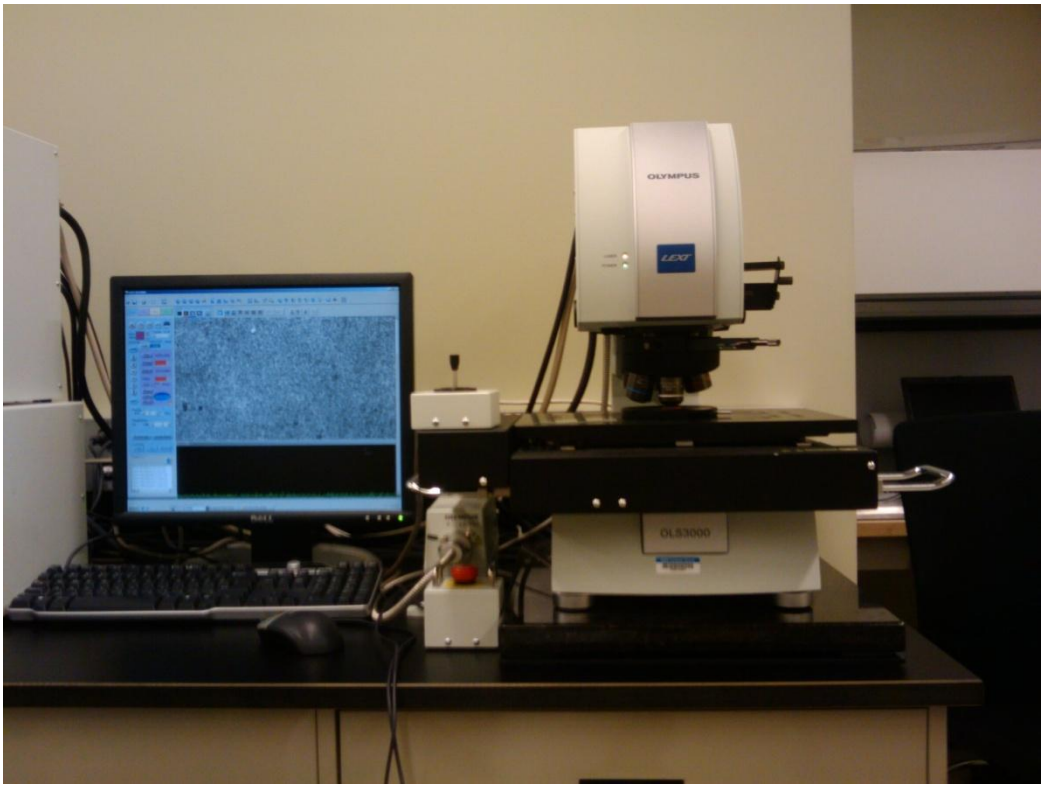

Figure 5-13: Olympus LEXT OLS3000 Confocal Scanning Laser Microscope used for roughness and topography measurements.

To account for noise spikes in the data that are caused by rear reflections from dust spots on the substrate, a local roughness value was also calculated based on a 30µm x 30µm area that was characteristic of the bulk roughness. The SRa and SRz values are shown in the table below, and the precision of the instrument is ~10nm.

Table 5-6: SRa and SRz values of for both the entire imaged area of 128µm x 128µm and a local characteristic spot of 30µm x 30µm.

Sample Name	Global SRa (µm)	Local SRa (µm)	Global SRz (µm)	Local SRz (µm)
Clean heater before boiling	0.04	0.01	0.17	0.04
Clean heater after boiling	0.04	0.01	0.32	0.08
0.1vol% silica	2.97	1.21	29.84	12.67
7nm 20 bilayers before boiling	0.03	0.03	2.38	0.44
7nm 20 bilayers after boiling	0.12	0.10	3.45	1.80
50nm 20 bilayers before boiling	0.09	0.04	0.91	0.75
50nm 20 bilayers after boiling	0.05	0.04	3.02	0.39
100nm 20 bilayer heater 2 after boiling	0.05	0.04	1.49	0.60
100nm 20 bilayer heater 3 after boiling	0.04	0.04	0.59	0.36
50nm 50 bilayer before boiling	0.07	0.06	0.91	0.65
50nm 100 bilayer before boiling	0.22	0.13	4.08	1.54

The roughness is not a strong function of particle size as can be seen below. The change is only about 15nm from 7nm particles to 100 nm particles which is not significant considering the measurement error. However, the roughness for the 20 bilayer case is 2.5 times that of a clean sapphire heater.

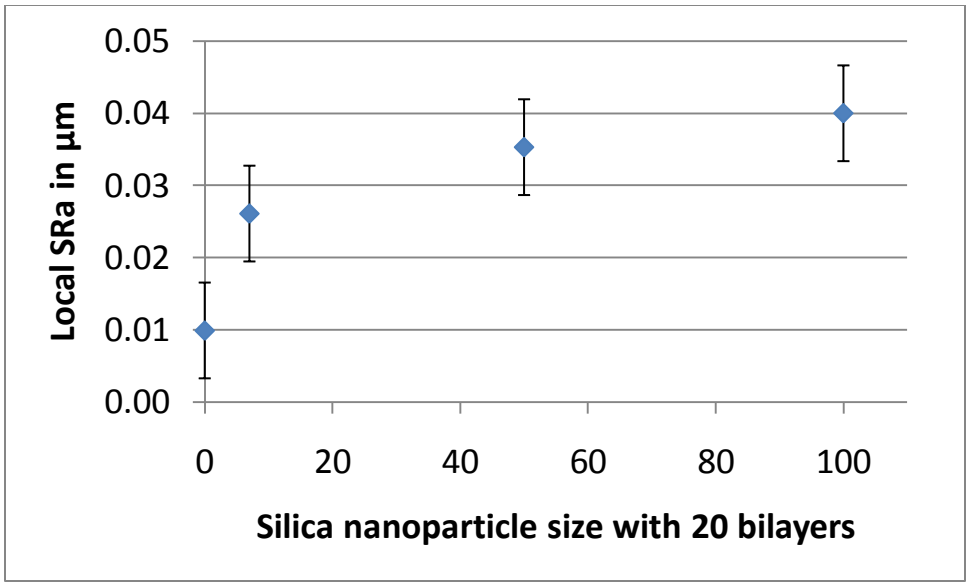

Figure 5-14: The local SRa of a 30µm x 30µm spot vs. the nanoparticle size for a 20 bilayer coating.

The roughness increases almost linearly with the number of bilayers of 50nm particles as shown below. The number of bilayers have an effect on roughness when applied to a smooth substrate such as sapphire. Forrest's boiling work [24] used similar coatings used stainless steel plates and the bilayers had no apparent effect on roughness; however, the metal plates had a SRa of nearly 300nm, and coating thicknesses of only up to 40 bilayers were tested. Therefore a change of 50nm in roughness was difficult to see with the variability of the roughness between different samples.

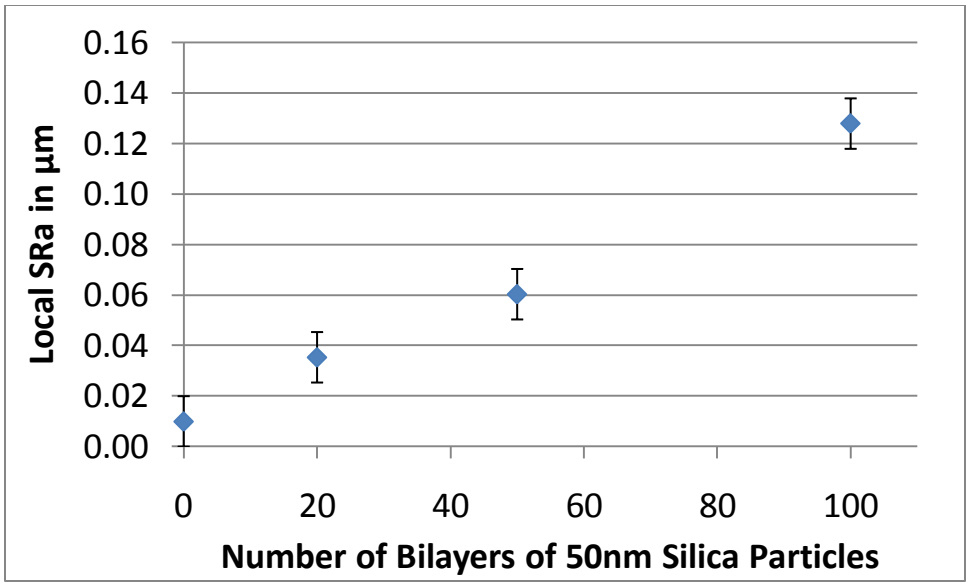

Figure 5-15: The local SRa of a 30µm x 30µm spot vs. the number of bilayers for 50nm silica particles.

The difference in roughness from a clean sapphire heater and a 50nm particles with 100 bilayers can be seen below in the 3D surface plots.

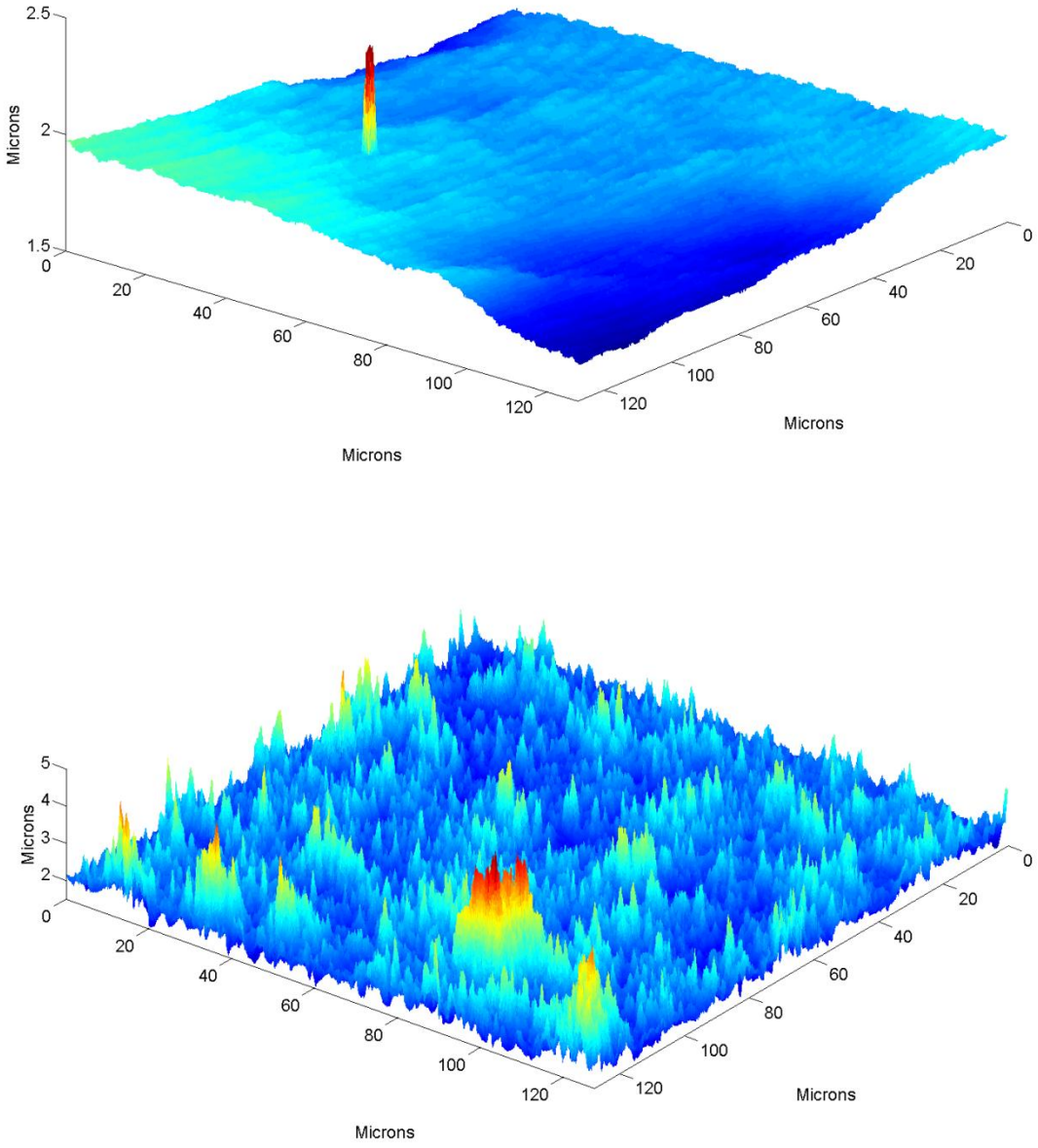

Figure 5-16: Clean heater before boiling, spike is a contamination spot that was used for focusing (Top). **50nm 100 bilayer heater number 3 before boiling** (Bottom). **There is a significant change roughness for this large number of bilayers.**

SEM images were taken of the surface to qualitatively see the assembly of the nanoparticles using a JEOL 6320F SEM that is shown below.

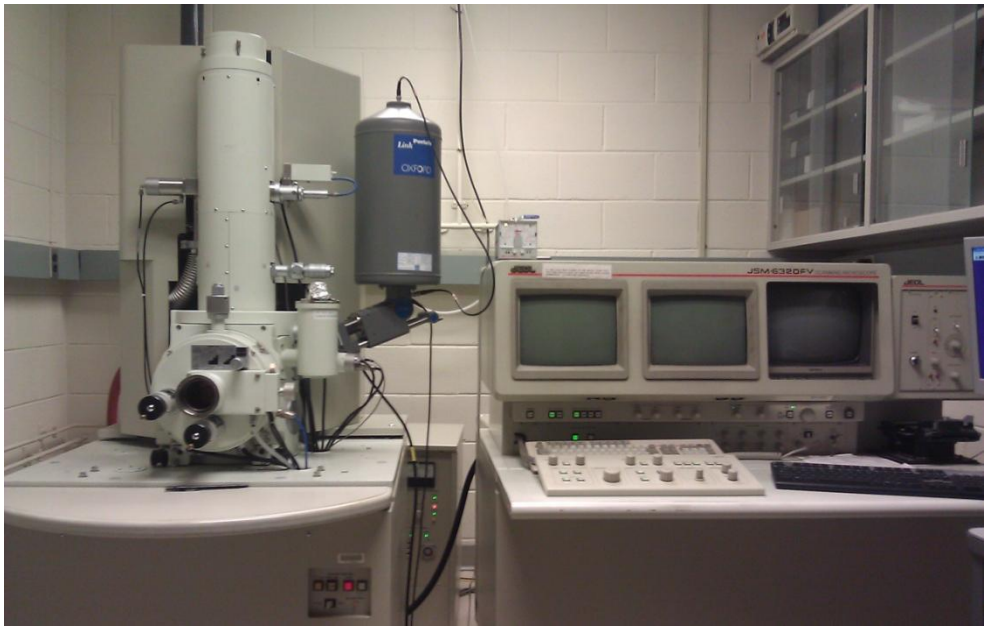

Figure 5-17: Photograph of JEOL 6320F HR Scanning Electron Microscope.

The 7nm particles could not be resolved with the JEOL 6320F. However, the 50nm and 100nm particle sizes were large enough and well defined enough to see individual particles.

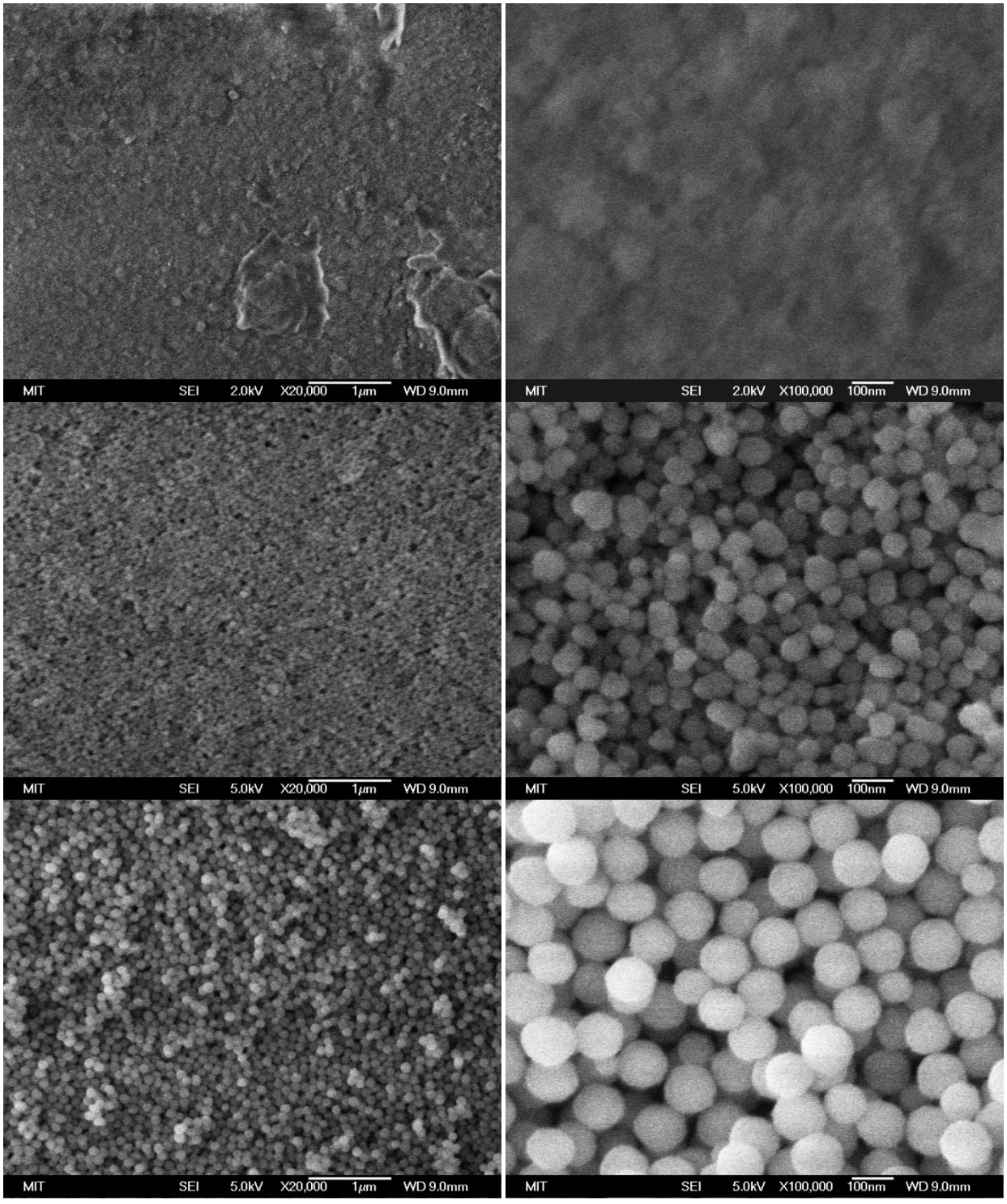

Figure 5-18: Pre-testing images of various particle sizes with 20 bilayers at 20k (left column) and 100k (right column) magnification. First row is 7nm particles, second row is 50nm particles, and the third row is 100nm particles.

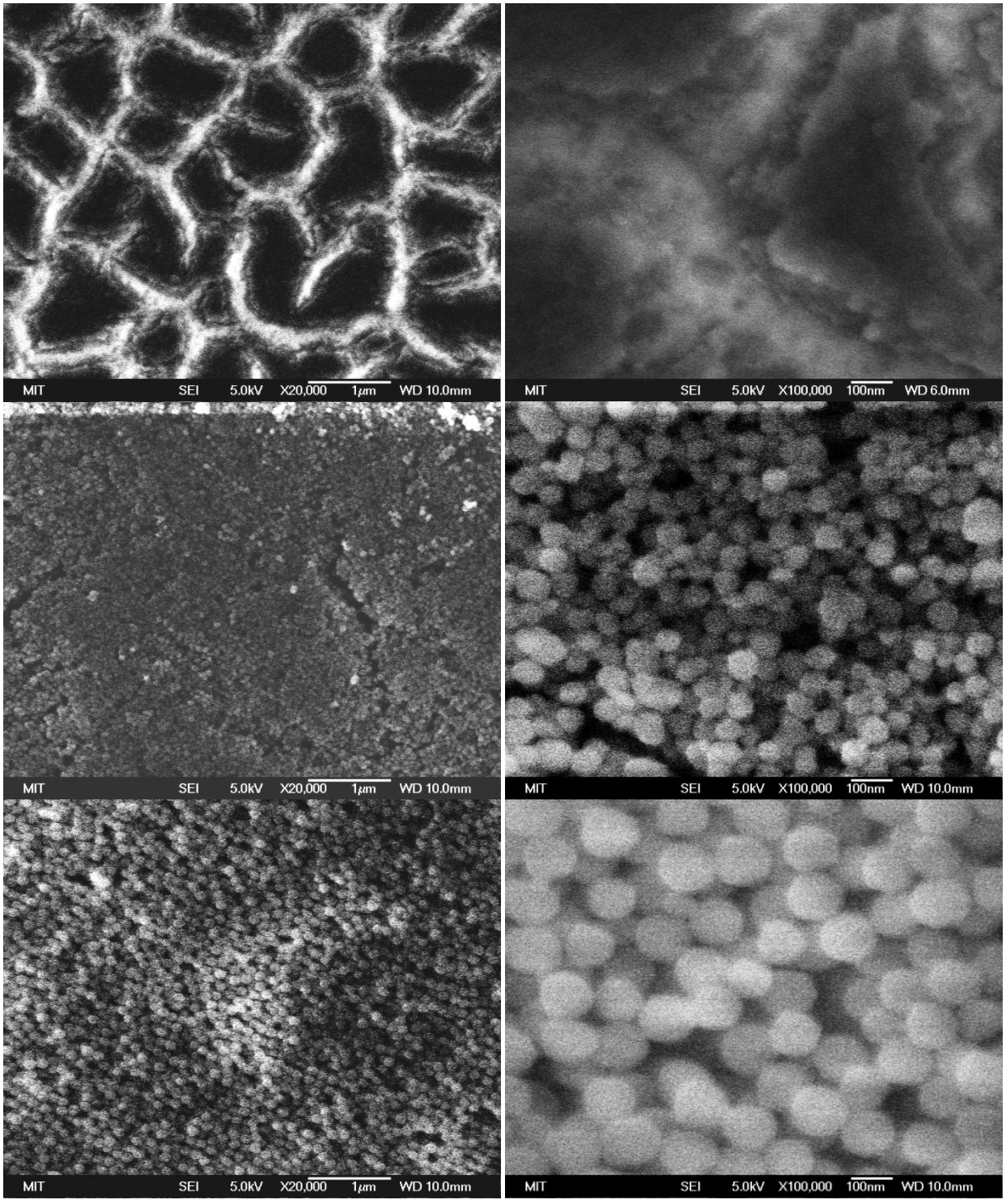

Figure 5-19: Post-testing images of various particle sizes with 20 bilayers at 20k (left column) and 100k (right column) magnification. First row is 7nm particles, second row is 50nm particles, and the third row is 100nm particles.

The cracks that are seen in the post-testing images in the above figure prompt the question of whether the cracking is occurring during the test or if the cracking occurs when CHF is reached and the surface temperature rises drastically. To test this a heater with 50nm particles and 50 bilayers was boiled at 1200kW/m^2 for 20 minutes then allowed to cool down while wet. The heater was then allowed to air dry and then imaged in the SEM. As can be seen in the figure below no cracking of the coating occurred when the heater was not allowed to reach CHF.

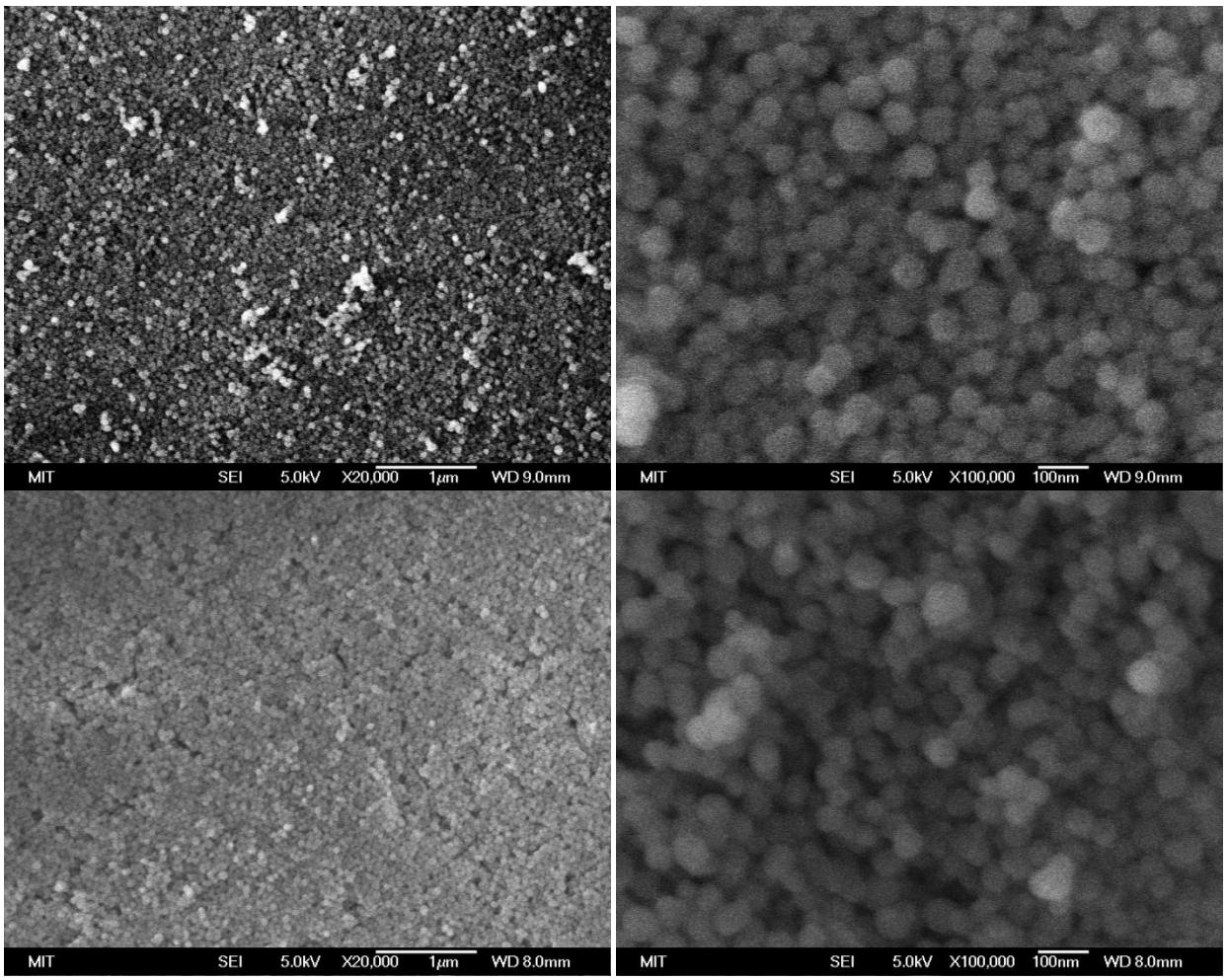

Figure 5-20: Heater coated with 50nm particles with 50 bilayers pre-test (top row), and the same coating after boiling at 1200 kW/m^2 for 20 minutes without reaching CHF (bottom row). The sample was allowed to cool to room temperature slowly while wet. Notice that there is no cracking when the heater is not allowed to reach CHF.

5.7.2 Silica nanoparticle layer thicknesses and porosity measured with spectroscopic ellipsometer

Ellipsometry is an optical technique used to characterize SiO2 thin films within the microelectronics industry [47]. Ellipsometry measures the polarization of light after reflection off of a surface and spectroscopic ellipsometry does this for many different wavelengths of light. The optical properties of the material affect how the light is polarized upon reflection, and modeling techniques allow for information to be extracted from the polarization such as thickness and refractive index. It is also possible to determine the porosity of a layer by filling the pores with a different medium (such as ethanol) and then using the rule of mixtures to determine the volume fraction of the pores according to the following equation [22].

$$p = \frac{n_2 - n_1}{n_{ethanol} - n_{air}} \qquad \textbf{Eq. 5-7}$$

Where p is the porosity, n_2 and n_1 represent the measured refractive indices of the film in ethanol and air respectively, and $n_{ethanol}$and n_{air} are the refractive indices of ethanol and air respectively. The optical properties at 620nm were used for calculating the porosity. The ellipsometry measurements were made with a J.A. Woollam Co., INC model XLS-100. The facility is shown in the figure below.

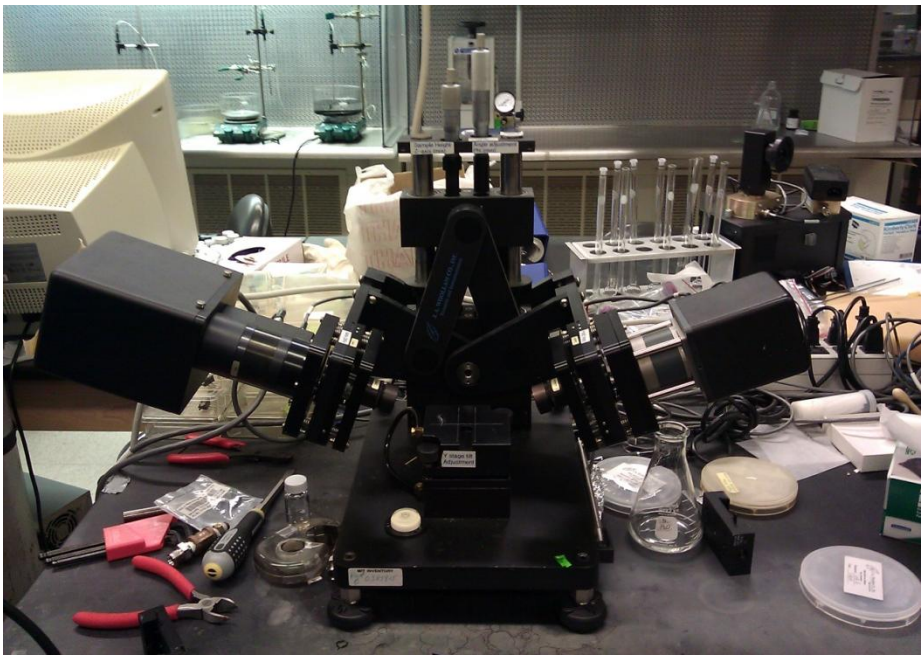

Figure 5-21: J.A. Woollam Co., INC model XLS-100 ellipsometer used for layer thickness and porosity measurements.

Three measurements were taken in air and three measurements were taken in ethanol, and since the measurements are independent this gives nine combinations that can be used to calculate the porosity. The average of the nine calculations was used to calculate the average porosity, and the standard deviation was used to estimate the error.

Table 5-7: The layer thicknesses and porosity for the various particle sizes and various numbers of bilayers.

Sample	Thickness (nm)	Per Bilayer Thickness (nm)	Thickness Sample Standard Deviation	Porosity	Porosity Standard Deviation(%)
7nm 20 bilayers	240	12	3.50%	0.39	13%
20/50nm 20 bilayers	440	22	2.30%	0.47	4%
50nm 20 bilayers	500	25	2.00%	0.59	5%
50nm 50 bilayers	1360	27	0.90%	0.49	6%
100nm 20 bilayers	990	49	0.70%	0.57	4%

The thickness and porosity for the 50nm particles with 100 bilayers could not be measured because of the opacity of the coating. However, if the thickness continues to increase linearly and thus have the same per bilayer thickness as for the 20 bilayer and 50 bilayer cases the thickness can be estimated to be ~2.7μm. The porosity cannot be estimated in the same manner, but all of the multilayers have similar porosity values of between 0.39 and 0.59, and it is reasonable to assume that the 50nm particle, 100 bilayer coating will fall in the same range.

The 7nm particles had a significantly lower porosity and a larger per bilayer thickness relative to the particle size than for the larger particle sizes. The larger per bilayer thickness is most likely due to conglomeration of the particles prior to deposition on the surface. The porosity while being significantly lower also had a significantly larger error than the other bilayers.

5.7.3 Contact angle measurements of multilayers

An AST Products INC VCA 2000 Video Contact Angle System with VCA Optima XE software was used to measure the static, advancing, and receding contact angles for all of the different multilayers. The setup is shown below.

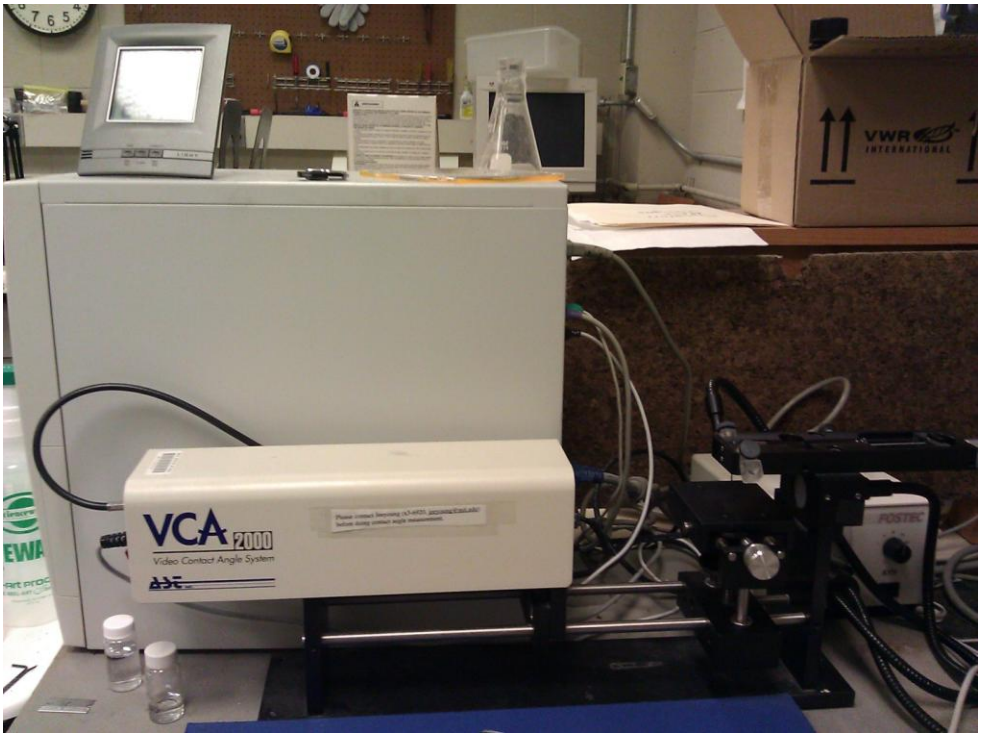

Figure 5-22: AST Products INC VCA 2000 Video Contact Angle System used for contact angle measurements.

The static contact angle was described in section 2.1; however, the advancing contact angle and receding contact angle are also important for boiling phenomena. The advancing contact angle represents the contact angle that water will make with a surface as a liquid/vapor/surface contact line is moving forward to a non-wetted area. The receding contact angle is then simply the angle the water makes with the surface as the liquid/vapor/surface is moving toward the wetted area. The static contact angle is measured at 0.5 seconds after the contact of the droplet with the surface. The advancing contact angle is measured by adding water to a static drop and then measuring the angle that the water makes with the surface right before the contact line begins to move forward. The receding contact angle is measured in a similar fashion by removing water from a static droplet then measuring the angle of the contact line just before the droplets contact line begins to move from the droplet shrinking. The receding

contact angle is normally the smallest, then the static is larger, and the advancing contact angle is the largest. These three cases are shown below.

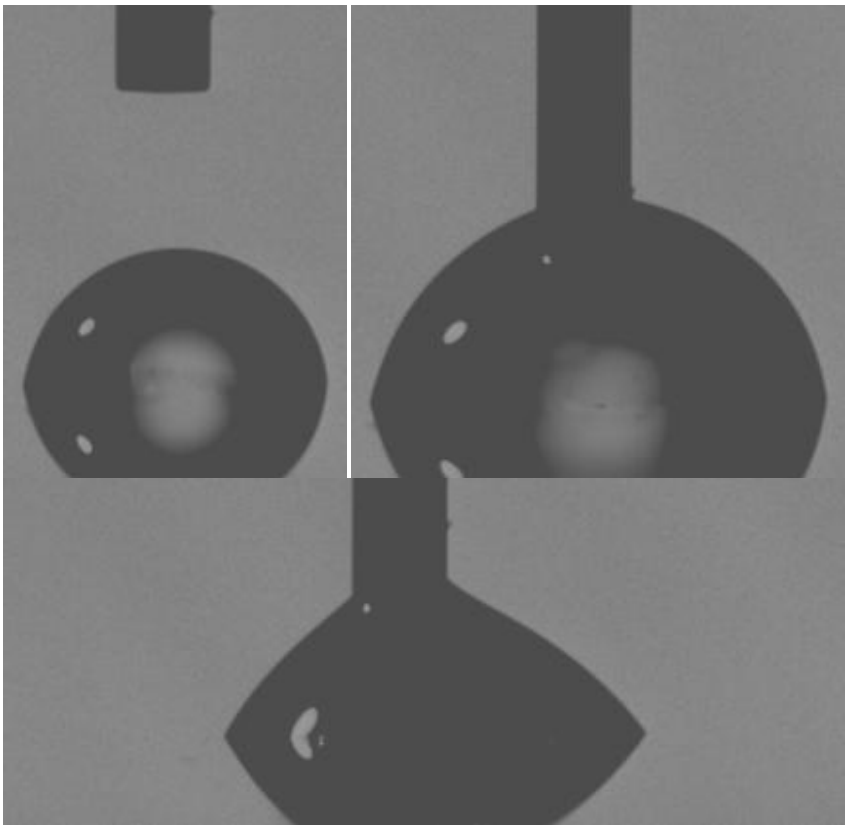

Figure 5-23: Measurement of contact angles, static contact angle (Top Left), the advancing contact angle (Top Right), and the receding contact angle (Bottom).

A summary of the contact angle data for the various multilayers on sapphire is shown in the table below.

Table 5-8: Static, advancing, and receding contact angles for all of the multilayers tested.

	Clean Heater	7nm 20bi	50nm 20bi	100nm 20bi	20/50nm 20bi	50nm 50bi	50nm 100bi	50nm 50bi fluorosilane
	64.0	8.0	29.1	29.7	< 5	18.3	28.6	139.3
Static	64.7	7.8	28.9	26.1	< 5	25.5	30.9	136.2
Angle	73.3	9.0	29.6	23.5	< 5	22.9	29.6	135.2
	74.5	7.9	28.7	25.6	< 5	25.1	30.1	138.4
	64.1	8.1	32.4	27.1	< 5	26.7	31.9	136.3
Average:	68.1	8.2	29.7	26.4	< 5	23.7	30.2	137.1
Std Dev:	8%	6%	5%	9%	N/A	14%	4%	1%
	66.0	14.4	34.2	33.2	8.8	33.2	47.3	154.6
Advancing	66.9	10.3	33.2	27.0	5.5	35.9	43.1	152.0
Angle	69.0	9.5	34.6	37.5	6.2	36.5	44.6	156.1
	69.0	12.8	36.9	38.2	9.5	36.4	47.6	159.4
	64.3	10.2	34.3	34.7	8.4	39.3	46.6	154.0
Average:	67.0	11.4	34.6	34.1	7.7	36.3	45.8	155.2
Std Dev:	3%	18%	4%	13%	23%	6%	4%	2%
	26.6	< 5	9.6	7.6	< 5	8.3	8.2	57.3
Receding	29.9	< 5	8.0	9.5	< 5	9.6	10.8	63.1
Angle	28.9	< 5	9.2	8.6	< 5	9.4	10.7	70.7
	34.4	< 5	11.2	8.2	< 5	10.7	10.9	71.0
	29.5	< 5	10.4	7.3	< 5	10.1	12.1	69.4
Average:	29.9	< 5	9.7	8.2	< 5	9.6	10.5	66.3
Std Dev:	10%	N/A	13%	11%	N/A	9%	14%	9%

5.8 Analysis of Separate Effect Results

5.8.1 Effect of layer thickness

The thermal conductivity of a porous layer can be estimated with the equation below [48].

$$k_{eff} = k_f \left(\frac{k_s}{k_f} \right)^{0.280 - 0.757\log(\varepsilon) - 0.057\log(k_s / k_f)} \qquad \text{Eq. 5-8}$$

Where k_{eff} is the effective thermal conductivity (W/K-m), k_f is the thermal conductivity of the fluid (W/K-m), k_s is the thermal conductivity of the solid (W/K-m), and ε is the porosity (dimensionless). Eq. 5-8 is valid for porosities from 20% to 60%, which covers the full range of porosities of the coatings used. The temperature drop across a 50% porous layer as a function thickness is shown below for a heat flux of 1MW/m^2.

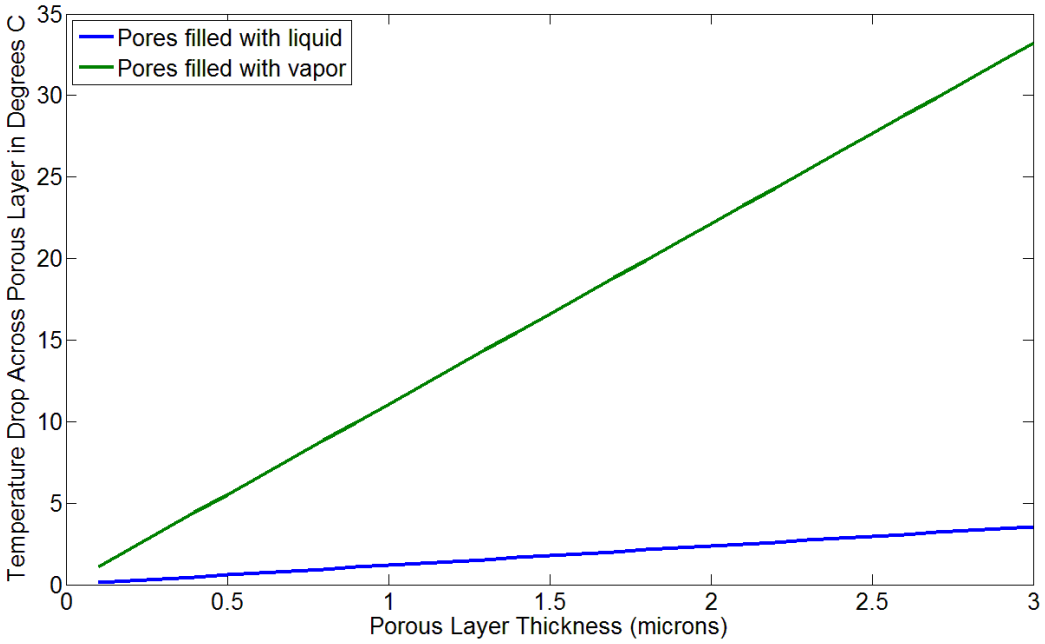

Figure 5-24: Temperature drop across a 50% porous silica nanoparticle layer vs. layer thickness for a heat flux of 1MW/m^{2}with the pores filled with both liquid water and water vapor.

As can be seen in the above figure, the temperature drop for the 50nm particle 100 bilayer case (~2.7 μm) is approaching 4°C for the liquid water case, which starts to become significant relative to the wall superheat. The effect is even more pronounced with vapor filled pores where the temperature drop can reach 30°C. This effect was not taken into account in the heat transfer coefficient plot.

5.8.2 Effect of Wettability

The wettability has an important influence on CHF as demonstrated by the results of section 5.6, and has been revealed by previous researchers [2]. The Zuber CHF prediction given in Eq. 2-6 is based on the hydrodynamic instability theory, thus it does not account for any surface conditions. Therefore, it would predict the same CHF value for the 50nm 50 bilayer hydrophilic coating and the same coating with a fluorosilane coating while in reality the hydrophilic coating has a CHF of 37 times higher. Therefore, driving factors behind CHF must also be the contact angle and chemistry of the surface. Then it is obviously important to account for the surface effects as is done the macrolayer dryout [49][50], and hot spot theories [51] of CHF.

The macrolayer dryout theory is based on a macrolayer that is defined by the contact angle of water with the surface. CHF is reached when the macrolayer vaporizes. As the contact angle goes down the macrolayer thickness goes up and increases CHF [49][50].

The hot spot theory describes the CHF event as being tied to a specific nucleation site that at some heat flux is no longer able to be rewet. This nucleation site forms a hot spot that will grow and coalesce with other hot spots eventually vapor blanketing the heater and leading to CHF. The CHF prediction is given below [51].

$$q''_{CHF} = \kappa^{-1/2} \rho_g h_{fg} \left[\frac{g\sigma(\rho_f - \rho_g)}{\rho_g^2} \right]^{1/4} \qquad \textbf{Eq. 5-9}$$

This is very similar to Zuber's prediction, except the dimensionless first constant that depends on surface properties. Kim et al. [2] proposed an analytical expression for κ that is shown below.

$$\kappa = \left(1 - \frac{\sin\theta}{2} - \frac{\pi/2 - \theta}{2\cos\theta}\right)^{-1/2} \quad \textbf{Eq. 5-10}$$

The value of κ is shown in the table below for the various coatings, along with the predicted enhancement of the coating relative to the bare surface. Eq. 5-8 does not apply for contact angles greater than 90° so it cannot be applied for the hydrophobic case. The enhancements are calculated the ratio of Eq. 5-9 for the different values of κ, and all of the parameters are the same except for κ, so the enhancement is just the ratio of the κ values to the -1/2 power.

Another correlation for the contact angles influence on CHF was proposed by Kandlikar, this once again has a similar format to Zuber's prediction, but accounting for heater orientation, and a slightly different influence from the contact angle:

$$q''_{CHF} = \left(\frac{1+\cos\theta}{16}\right)\cdot\left[\frac{2}{\pi} + \frac{\pi}{4}(1+\cos\theta)\cos\phi\right]^{1/2} \rho_g h_{fg}\left[\frac{g\sigma(\rho_f - \rho_g)}{\rho_g^2}\right]^{1/4} \quad \textbf{Eq. 5-11}$$

Where θ is the static contact angle and ϕ is the angle the heater makes with the horizontal.

Table 5-9: Values for κ for the various multilayers and experimental and predicted CHF enhancements.

	Static Contact Angle	*K* (Kim)	Experimental % CHF Enhancement	Predicted % CHF Enhancement (Kim)	Predicted % CHF Enhancement (Kandlikar)
Clean Heater	68.1	6.5	N/A	N/A	N/A
7nm 20 bilayers	8.2	2.2	21%	58%	34%
50nm 20 bilayers	29.7	2.61	74%	63%	47%
20/50nm 20 bilayers	5	2.17	75%	58%	80%
100nm 20 bilayers	26.4	2.52	62%	62%	81%
50nm 50 bilayers	23.7	2.45	106%	61%	68%
50nm 100 bilayers	30.2	2.63	112%	64%	85%

The values are very close for the thin porous coatings. However, there is clearly a dependence on the multilayer thickness that is not captured solely by the contact angle, which does not change appreciably as the layers get thicker.

6 Patterned Surface Effects

Using the results obtained in the separate effect experiments discussed in section 0, patterned surfaces were created to explore the effects of varying the wettability across the surface of the heater. Several different patterned surfaces are explored including a hydrophobic surface with small hydrophilic "islands", and various hydrophilic surfaces with small hydrophobic "islands" of different sizes and spacing.

6.1 Patterning Procedure

The surface is first prepared with a 50nm particle 50 bilayer coating, which proved to be the coating with the highest CHF and heat transfer coefficient from section 0. The surface is then treated with a fluorosilane coating as discussed in section 5.1. After the surface has set overnight, the surface is patterned by using a UV ozone chamber and fused quartz silica masks (see section 3.3). The UVO chamber is checked to ensure it is hooked up to ventilation, and stands are positioned on the chamber tray so that there is only ~2mm clearance between the UV light and the masks when the samples are placed in the chamber. Prior to placing the samples and masks in the chamber, the chamber is operated for 12 minutes to clean the surfaces and warm up the lamp. The samples are then placed on the stands in the UVO tray and the masks are placed on top of the sapphire side of the heater with the chromium side facing the sapphire. The chamber is then closed and set for a 2 hour exposure. At the conclusion of the exposure the surfaces are patterned and ready to be prepared for a boiling test as discussed in section 5.3.1.

6.2 Hydrophobic "Sea" with 12μm hydrophilic "islands"

Two different surface types were tested that had a hydrophobic "sea" with hydrophilic "islands." Both patterns had 12μm island sizes on a hexagonal lattice; on one the islands had a

1mm pitch and on the other the islands had a 2mm pitch. The islands were too small to be visible from condensation patterns on the heater. This is because the average drop size on the hydrophobic surface was ~20-30μm which is larger than the hydrophilic regions.

The boiling tests behaved similarly to the pure hydrophobic surface discussed in section 5.6, where a large region of the heater film boiled at a low heat flux. However, the size of the region was smaller, and the region grew more slowly with an increasing heat flux. However, by about 100kW/m2 there were large sections that were film boiling, and would not rewet, and essentially represented CHF for these heaters. The differences and similarities can be seen in the figure below that shows both the purely hydrophobic surface, and the hydrophobic surface with hydrophilic islands.

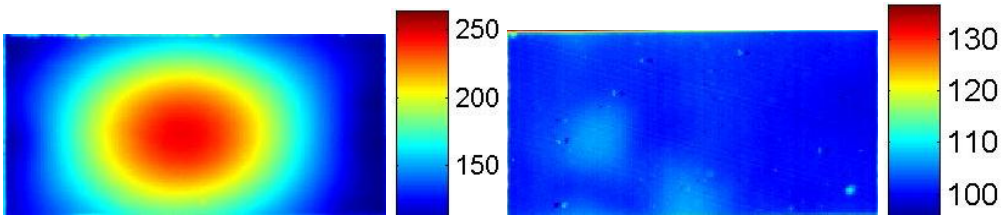

Figure 6-1: Pure hydrophobic surface at 40.9kW/m^2 (Left) and a hydrophobic surface with 12μm hydrophilic islands on 1mm pitch (Right) at 45.9kW/m^2. Notice that the pure hydrophobic surface has a larger hot spot and higher temperatures.

The heaters with 1mm pitch and 2mm pitch performed similarly as can be seen in the boiling curve and heat transfer coefficient figures below.

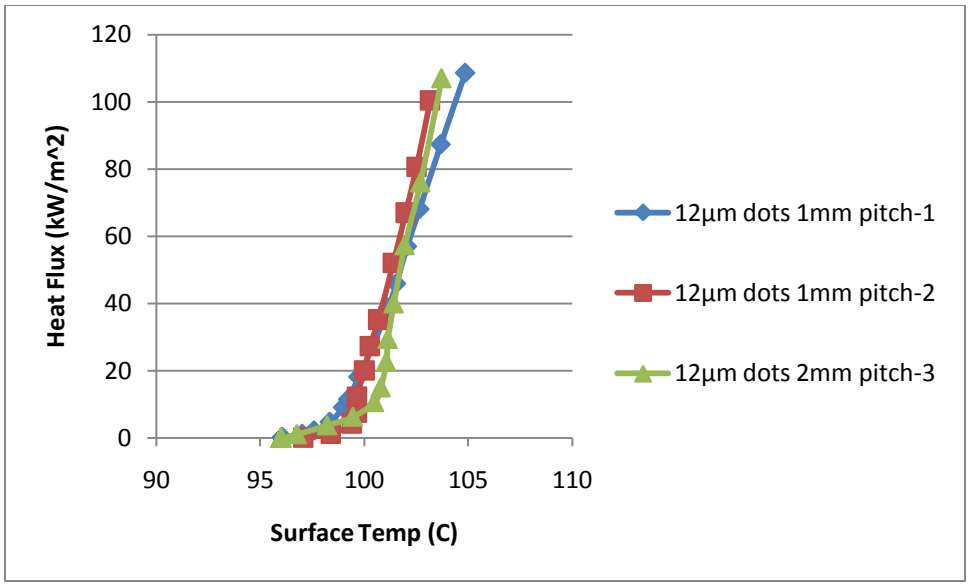

Figure 6-2: Boiling curves for 12µm islands on a 1mm and 2mm pitch. The first test of the 2mm pitch failed due to a power supply transient.

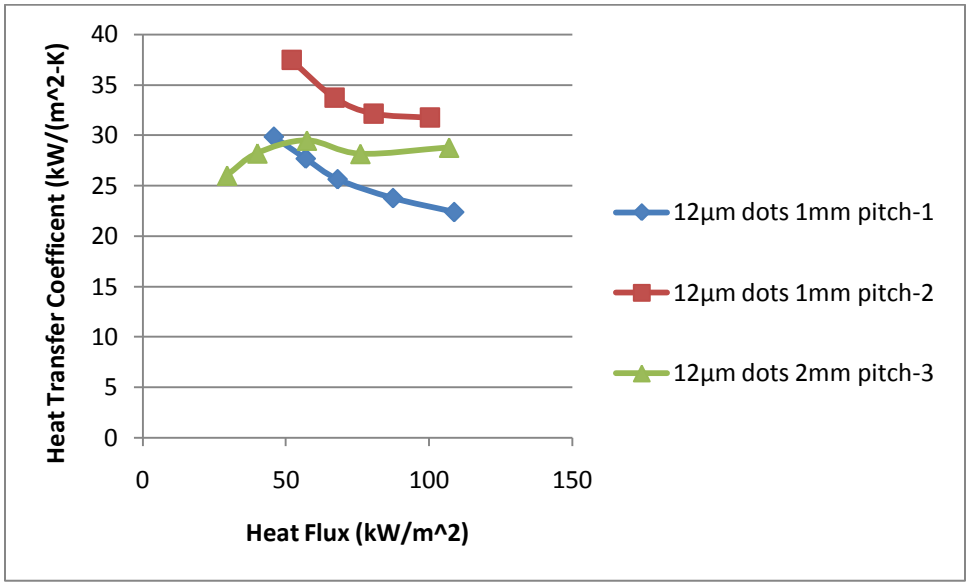

Figure 6-3: Heat transfer coefficients for 12µm islands on a 1mm and 2mm pitch. The first test of the 2mm pitch failed due to a power supply transient.

6.3 12µm Hydrophobic "Islands" in a Hydrophilic "Sea"

Again, two different types of 12µm Hydrophobic "Islands" in a Hydrophilic "Sea" on a hexagonal lattice were tested, one on a 1mm pitch and one on a 2mm pitch. As in the previous section, the islands could not be identified from condensation patterns. However, when looking at large areas of transition from the hydrophobic to hydrophilic region, a transition region could be observed that was ~30µm in size that can be seen in Figure 6-4. This indicates that the 12µm hydrophobic features may have been too small for the resolution of the patterning process. However, this differs from the previous section with the hydrophilic regions. Even though the hydrophilic regions could not be distinguished, they are highly likely to exist on the surface because the lack of resolution will tend to make hydrophilic regions larger than the size on the mask. The hydrophilic locations are larger since the UV passes through the transparent locations on the mask to create ozone and destroy the fluorosilane layer. Therefore, in the previous section, the hydrophilic islands should have existed and been larger than 12µm.

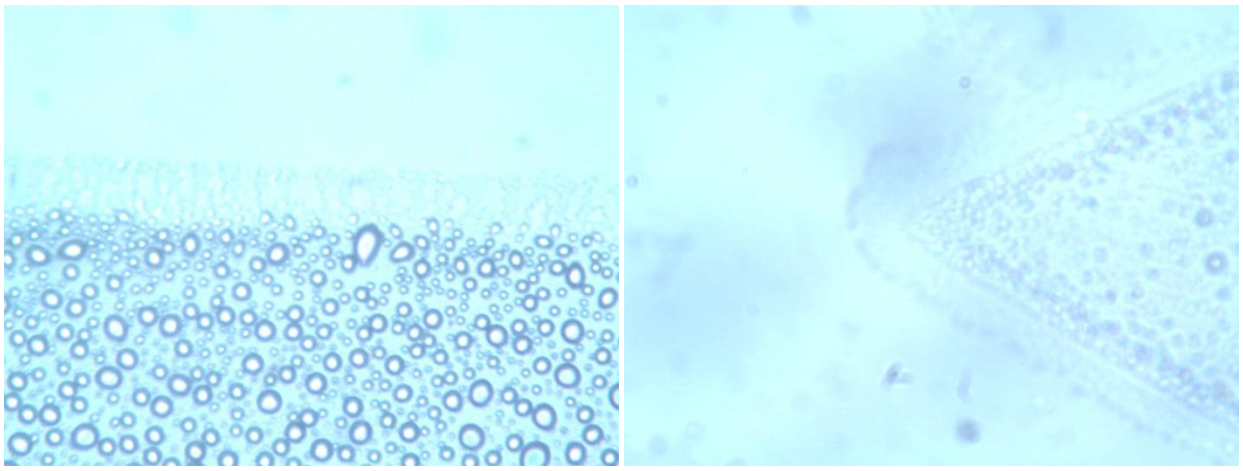

Figure 6-4: Optical microscope images of hydrophobic/hydrophilic interfaces for patterned nanoparticle surfaces. The horizontal view scale is ~250 um. The transition region is ~30µm.

All of the CHF results for the 12μm feature sizes, as well as for those of 160μm and 260μm that are discussed in the next section are shown in the table below. The boiling curves and heat transfer coefficients for the 12μm features are shown in the following figures.

Table 6-1: CHF results for 12μm feature size hydrophilic "sea" patterned surfaces. Table also includes clean heaters, 0.1Vol% silica, and 50nm 50 bilayer coating for comparison.

Test Name	CHF (kW/m^2)	Average CHF (kW/m^2)	% CHF Enhancement over Clean Heater	CHF Spread Percentage	CHF Standard Deviation Percent
Clean Heater-6	920				
Clean Heater-7	986				
Clean Heater-8	799				
Clean Heater-9	885				
Clean Heater-10	947	907	0%	21%	8%
0.1 vol%-1	1732				
0.1 vol%-2	1720	1726	90%	1%	1%
50nm 50 bilayers-1	2030				
50nm 50 bilayers-2	1800				
50nm 50 bilayers-3	1770	1867	106%	10%	8%
12um dots 1mm pitch-1	1900				
12um dots 1mm pitch-3	1860	1880	107%	2%	2%
12um dots 2mm pitch-1	2000				
12um dots 2mm pitch-2	1408				
12um dots 2mm pitch-3	2120	1843	103%	39%	21%

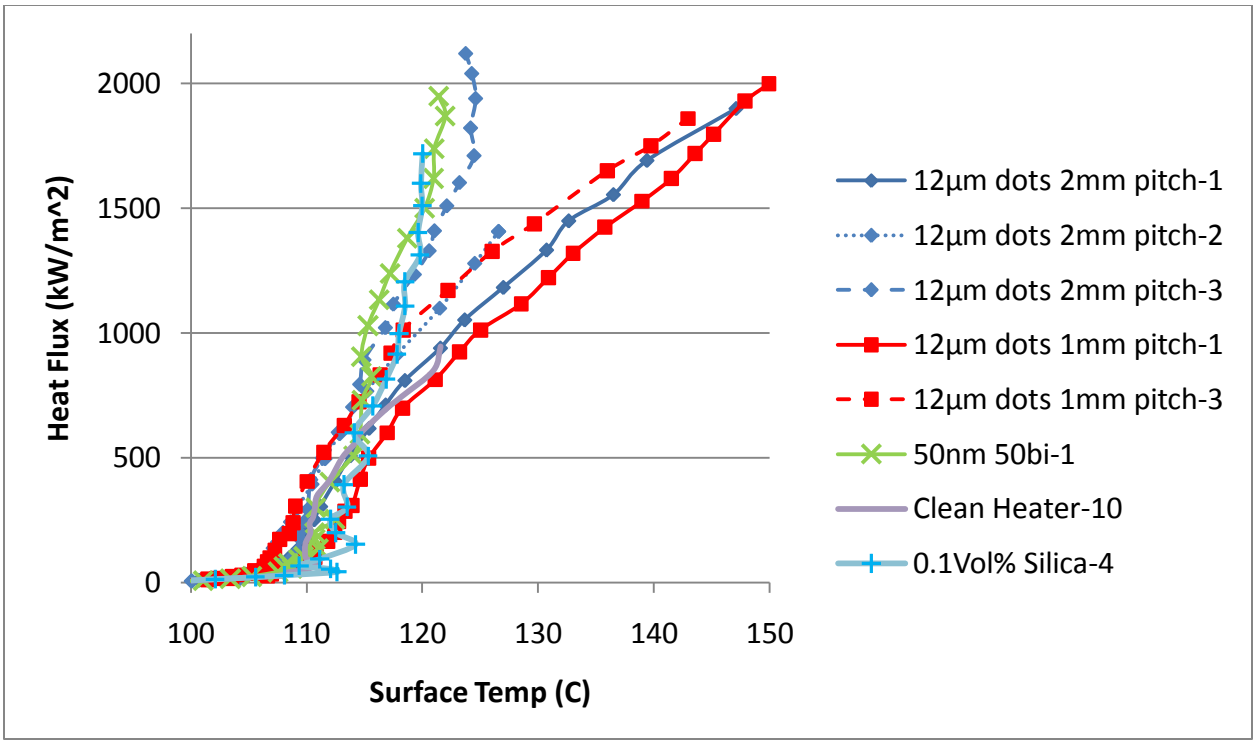

Figure 6-5: Boiling curves for 12µm hydrophobic "islands" in a hydrophilic "sea" with characteristic 50nm 50 bilayer coating, clean heater, and 0.1Vol% silica as comparisons

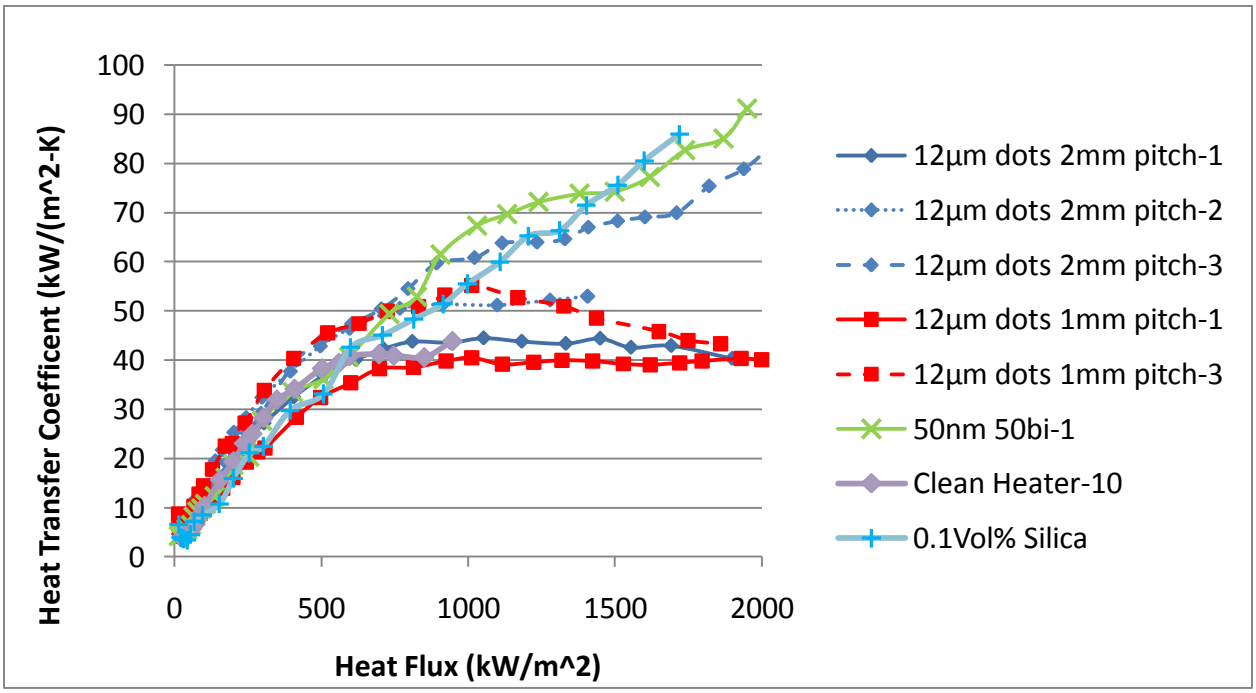

Figure 6-6: Heat transfer coefficients for 12µm hydrophobic "islands" in a hydrophilic "sea" with characteristic 50nm 50 bilayer coating, clean heater, and 0.1Vol% silica as comparisons

In general these 12μm patterned surfaces had very similar CHF values to the 50nm 50 bilayer coating, which is the underlying coating under the patterned surface. However, some had degraded heat transfer coefficients as shown in Figure 6-6.

6.4 160μm and 260μm hydrophobic "islands" in hydrophilic "sea"

Because of the patterning resolution issue that was discussed in the previous section, masks with 160μm and 260μm dot sizes were used to create larger hydrophobic "islands". These should create islands of nominal size of 100μm and 200μm based on the estimate of the resolution derived from Figure 6-4. Optical microscope pictures are shown in the figure below

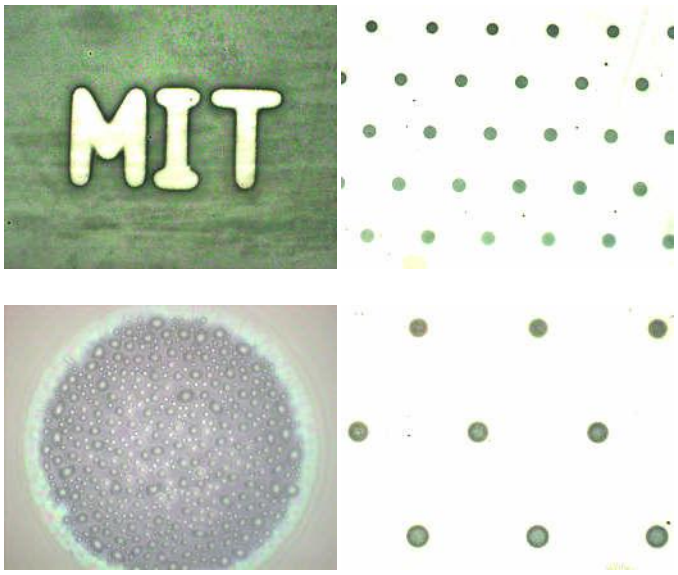

Figure 6-7: Optical microscope images of a slide patterned with the 260μm 1mm pitch mask. The top images have a horizontal length of ~5.5mm, bottom left image has a horizontal length of ~220μm, bottom right image has a horizontal length of ~4mm. The dots are spaced 1mm apart and each dot is ~180μm in diameter. Dark regions are hydrophobic and condense drop-wise forming an opaque layer while clear regions are hydrophilic and condense film-wise making a transparent layer.

The above optical microscope images confirm that there is a patterned surface for the 160μm and 260μm masks. For the 260μm masks the actual feature size is ~180μm and for the 160μm masks the actual size is ~90μm. Both feature sizes are slightly smaller than the target sizes of 200μm and 100μm, but are close, and offer a significant difference in the feature size to see if there is an effect on boiling. The CHF results are shown in the table below.

Table 6-2: CHF results for 160µm and 260µm feature sizes with hydrophilic "sea" patterned surfaces. Table also includes clean heaters, 0.1Vol% silica, and 50nm 50 bilayer coating for comparison.

Test Name	CHF (kW/m^2)	Average CHF (kW/m^2)	% CHF Enhancement over Clean Heater	CHF Spread Percentage	CHF Standard Deviation Percent
Clean Heater-6	920				
Clean Heater-7	986				
Clean Heater-8	799				
Clean Heater-9	885				
Clean Heater-10	947	907	0%	21%	8%
0.1 vol%-1	1732				
0.1 vol%-2	1720	1726	90%	1%	1%
50nm 50bilayers-1	2030				
50nm 50bilayers-2	1800				
50nm 50bilayers-3	1770	1867	106%	10%	8%
160um dots 1mm pitch-1	1600				
160um dots 1mm pitch-2	1790				
160um dots 1mm pitch-3	1800	1730	91%	12%	7%
160um dots 2mm pitch-1	1600				
160um dots 2mm pitch-2	2100				
160um dots 2mm pitch-3	2165	1955	115%	29%	16%
260um dots 1mm pitch-1	1640				
260um dots 1mm pitch-2	1930				
260um dots 1mm pitch-3	1450	1673	84%	29%	14%
260um dots 2mm pitch-1	1910				
260um dots 2mm pitch-3	1600	1755	93%	18%	12%

Again, the CHF enhancements are clustered around the values for the 50nm 50 bilayer coating case which is the underlying layer for the patterned surface. There is a much wider variability in the CHF than for the base surface. This may be due to inconsistencies in the fluorosilane coating and then the resulting patterned surface. The boiling curves and heat transfer coefficients also show large variations as seen in the figures below.

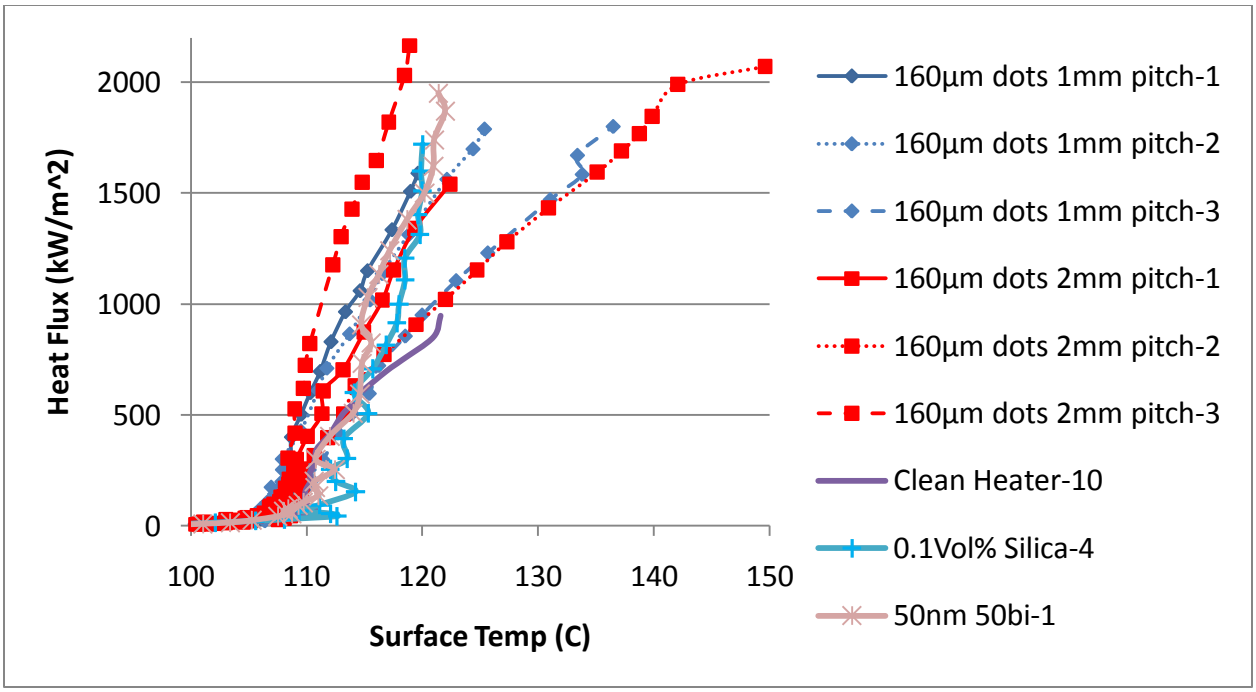

Figure 6-8: Boiling curves for 160µm hydrophobic "islands" in a hydrophilic "sea" with characteristic 50nm 50 bilayer coating, clean heater, and 0.1Vol% silica as comparisons

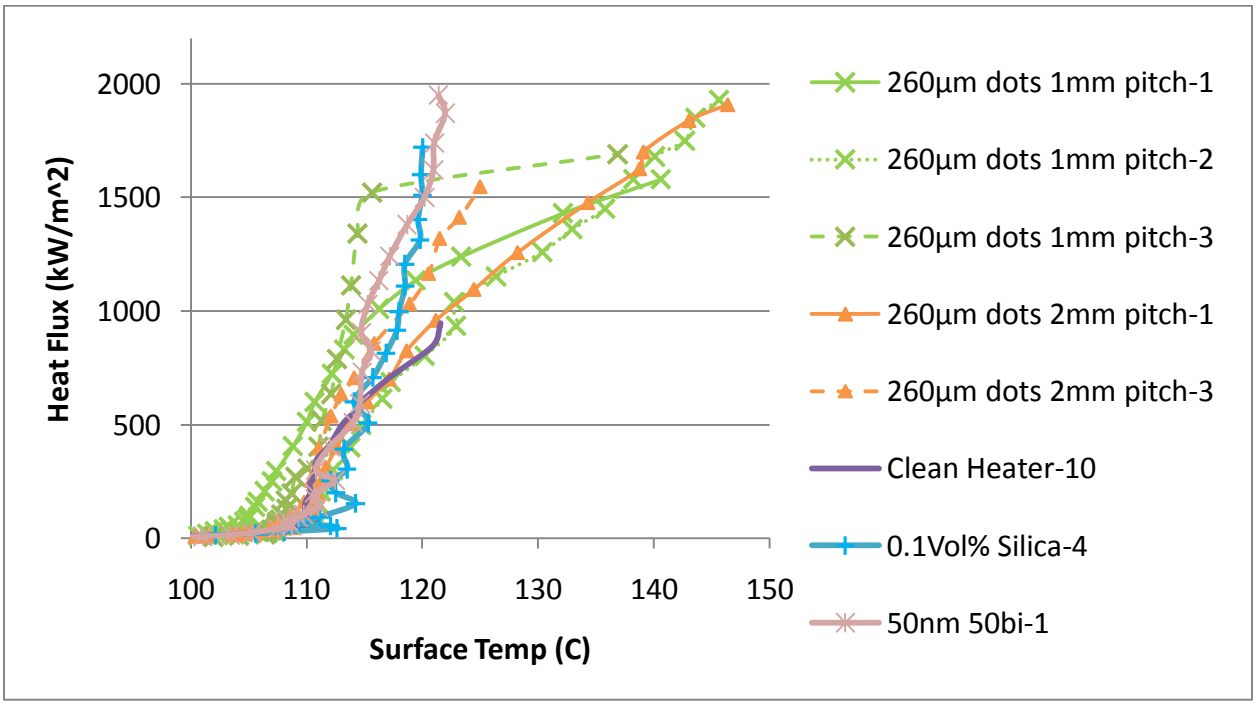

Figure 6-9: Boiling curves for 260µm hydrophobic "islands" in a hydrophilic "sea" with characteristic 50nm 50 bilayer coating, clean heater, and 0.1Vol% silica as comparisons

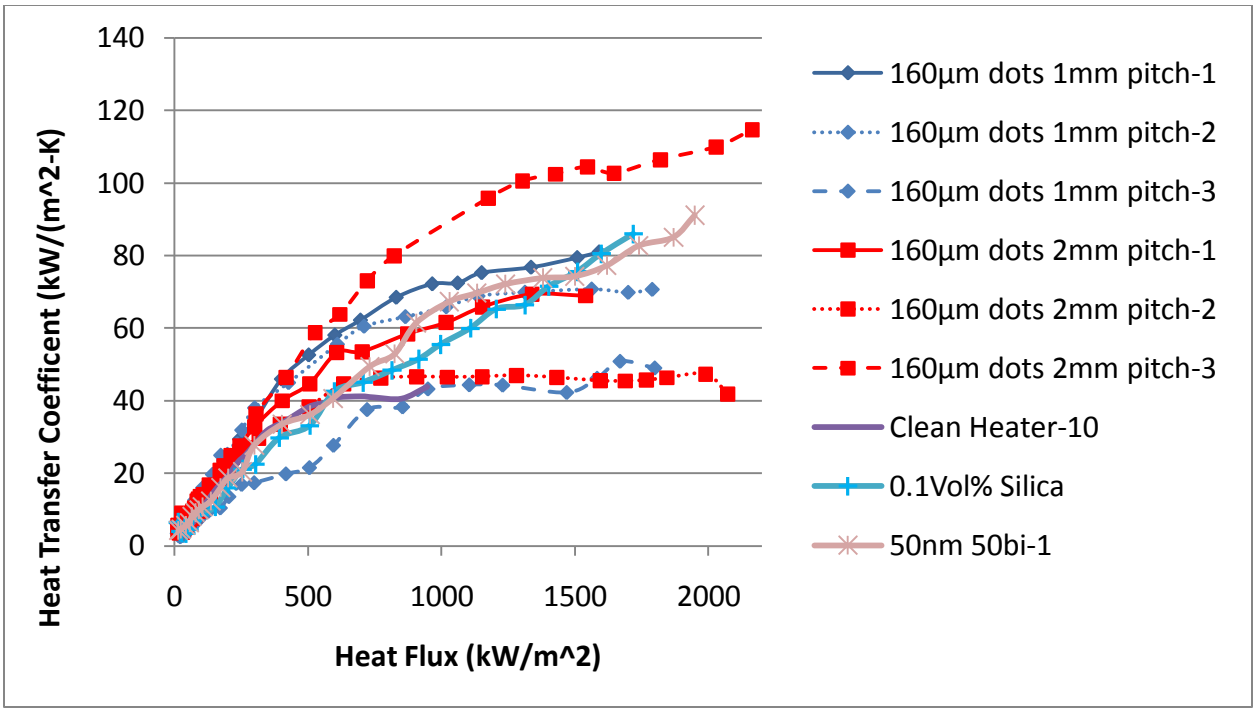

Figure 6-10: Heat transfer coefficients for 160µm hydrophobic "islands" in a hydrophilic "sea" with characteristic 50nm 50 bilayer coating, clean heater, and 0.1Vol% silica as comparisons

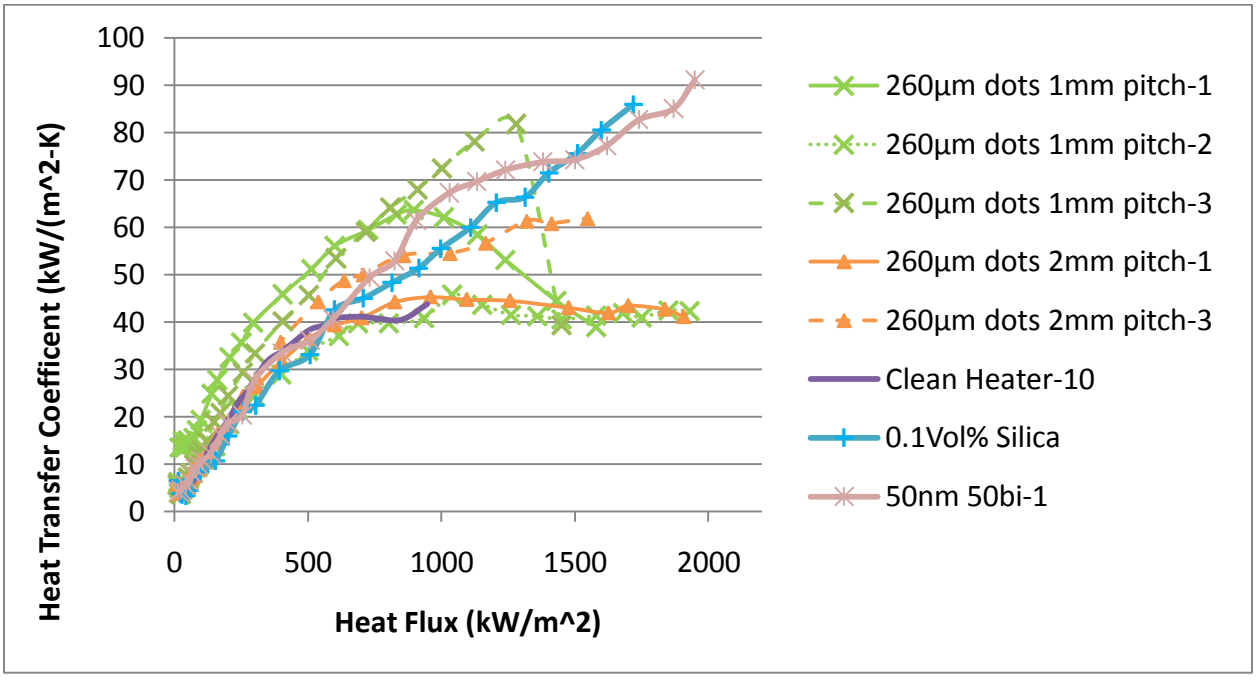

Figure 6-11: Heat transfer coefficients for 260µm hydrophobic "islands" in a hydrophilic "sea" with characteristic 50nm 50 bilayer coating, clean heater, and 0.1Vol% silica as comparisons

Examining Figure 6-8 through Figure 6-11 there appear to be two different regimes for the heat transfer coefficient. The first group is clustered around the improved results from 50nm particles with 50 bilayers, with some having a better heat transfer coefficient than the 50nm 50 bilayer case. The second group is clustered around the results for a clean heater and the heat transfer coefficient saturates at a similar value to that of a clean heater even though the CHF is still enhanced. Some experiments (such as the 260μm dots 1mm tests 1 and 3) even appear to make a transition from one regime to the other within the test. Tests from different island sizes and for different spacing appear in both regimes. The patterned surface does withstand the boiling process as is evidenced by the patterned boiling that takes place on these patterned surfaces throughout the boiling test. This can be seen in the figure below.

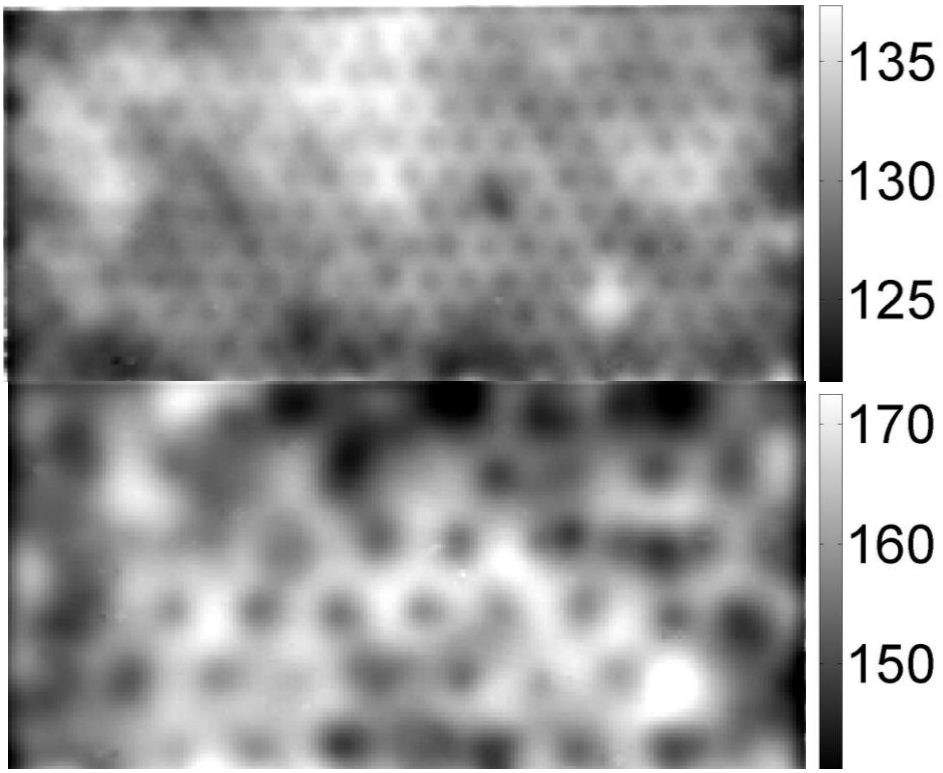

Figure 6-12: IR images of the surface of 260µm hydrophobic dots on a 1mm pitch [Top] and a 2mm pitch [Bottom]. The 1mm pitch photo [Top] is at 1240 kW/m^2 and the 2mm pitch [Bottom] is at 1838 kW/m^2. Temperatures are in degrees C.

In Figure 6-12 nucleation sites can clearly be seen as the dark locations on the IR image. These are the locations where the bubbles are nucleating and the phase change is cooling down the surface. The nucleation sites correspond to the hydrophobic "island" regions. The pattern could only be seen on the 260µm island size tests.

The large spread of the data is most likely due to the random nature of the deposition of the fluorosilane layer, which this process is used to create the hydrophobic areas on all of the patterned surfaces. This large scatter in heat transfer data has been observed when using this method to deposit the fluorosilane layer [24]. The patterned surfaces show similar critical heat fluxes and heat transfer coefficients to those of the underlying surface. However, 1mm very

close to a typical bubble departure diameter for water boiling at atmospheric pressure. This can be seen in the figure below.

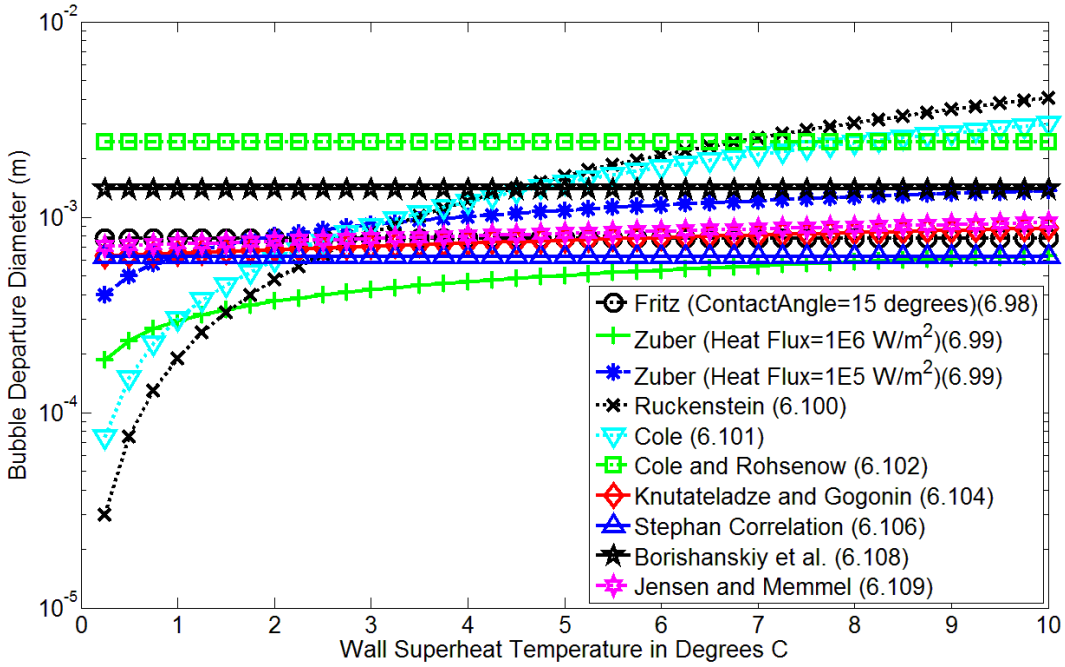

Figure 6-13: Bubble departure diameter vs. wall superheat at atmospheric pressure for various correlations. The numbers in parenthesis represent the equation number from reference[3].

At a few degrees of superheat, the bubble departure diameter is around 1mm at atmospheric pressure as can be seen in the above figure. There is a large scatter in the various correlations, and the value is somewhere between 0.5mm and 2mm. The actual value depends on heat flux, contact angle, and other surface characteristics that most of the correlations do not account for. However, this raises the question of whether the heat transfer coefficient could be improved with a patterned surface beyond what was tested here by decreasing the pitch of the hydrophobic "islands" to slightly less than 1mm to increase the nucleation site density and potentially increasing the heat transfer coefficient.

6.5 Nucleation Site Density

The nucleation site density expresses the number of active nucleation sites (such as shown in Figure 2-1) on a surface per unit area. As the wall superheat increases, which increases with the heat flux, the number of nucleation sites will increase as more sites are activated. The number of sites also influences the rate of heat removal from the surface since much of the heat is transferred through vaporization of water. Other bubble parameters also influence the heat transfer coefficient such as the bubble departure diameter and the bubble departure frequency since these also affect the rate at which water is vaporized. There are various methods to predict nucleation site density. However, most methods make predictions without knowing the distribution of the size and shape of cavities on the heat transfer surface, because these parameters are very difficult to measure on an engineering surface. Wang and Dhir proposed the following correlation for nucleation site density as a function of contact angle, and the critical diameter [52].

$$N_{SD}\left(\frac{\#sites}{cm^2}\right) = \frac{5x10^5(1-cos\theta)}{{D_c}^6} \qquad \textbf{Eq. 6-1}$$

Where N_{SD} is the nucleation site density (sites/cm^2), θ is the static contact angle (degrees), and D_c is the critical diameter (μm) (twice the critical radius that is given in Eq. 2-4).

Using infrared thermography, nucleation site density is a straight forward parameter to measure since each nucleation location can be seen from the video. However, because the heater is utilized with the ITO on the back surface of the heater, and thus some image definition is lost (discussed in section 4.2.7), it becomes difficult to accurately count the sites when the density rises above ~90 sites/cm^2. The sites are manually selected using a MATLAB code written for the purpose of counting nucleation sites. Example images of the site counting process are shown

below. The error associated with this type of measurement has been estimated by Gerardi to be ~2% [34], and should be true for this work up to the nucleation site density limit mentioned above. In the figure below not all sites that are marked are evident in the IR image because this is just one image out of a sequence of 2000, and not all sites were active in a given frame. Also, some sites appear to not be marked, but instead are bubbles that have shifted from a previously marked site during their growth cycle. For the patterned surface, the hexagonal pattern is beginning to emerge, this can be best seen in the upper right hand corner of the bottom image.

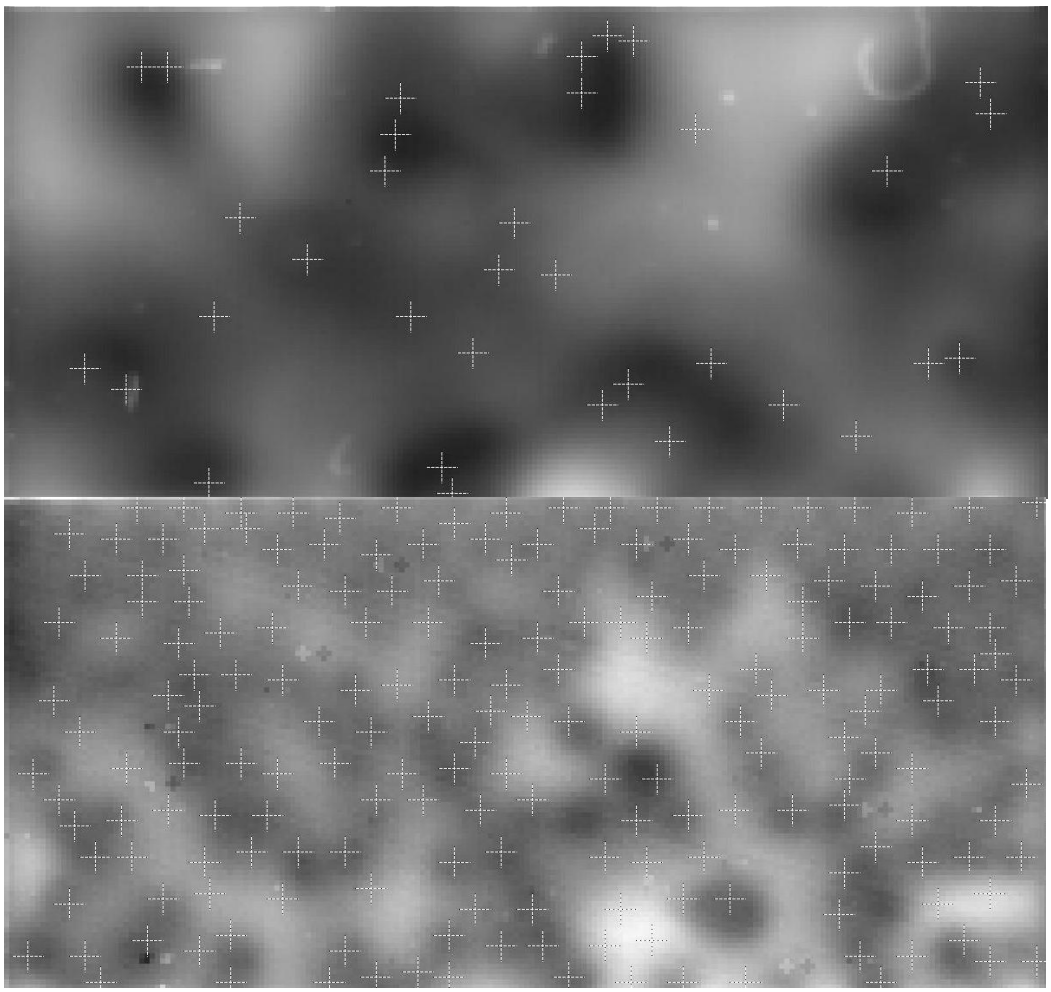

Figure 6-14: Nucleation site counting for a clean heater at 503kW/m^2 (Top) and for one patterned with 260μm hydrophobic dots on 1mm pitch at 512KW/m^2 (Bottom). The black and white crosses represent nucleation sites.

The nucleation site density for characteristic tests for each boiling sample is shown below. Each curve starts at a heat flux of ~100kW/m^2, and each data point is separated by ~100-150kW/m^2. The nucleation site density was determined for up to ~1000 kW/m^2 or until the site density of ~90sites/cm^2 was reached, where accurate counting was not longer possible. Eq. 6-1 was plotted for a contact angle of 25°, which is representative of the 50nm 50 bilayer coating that is underneath the patterned surfaces.

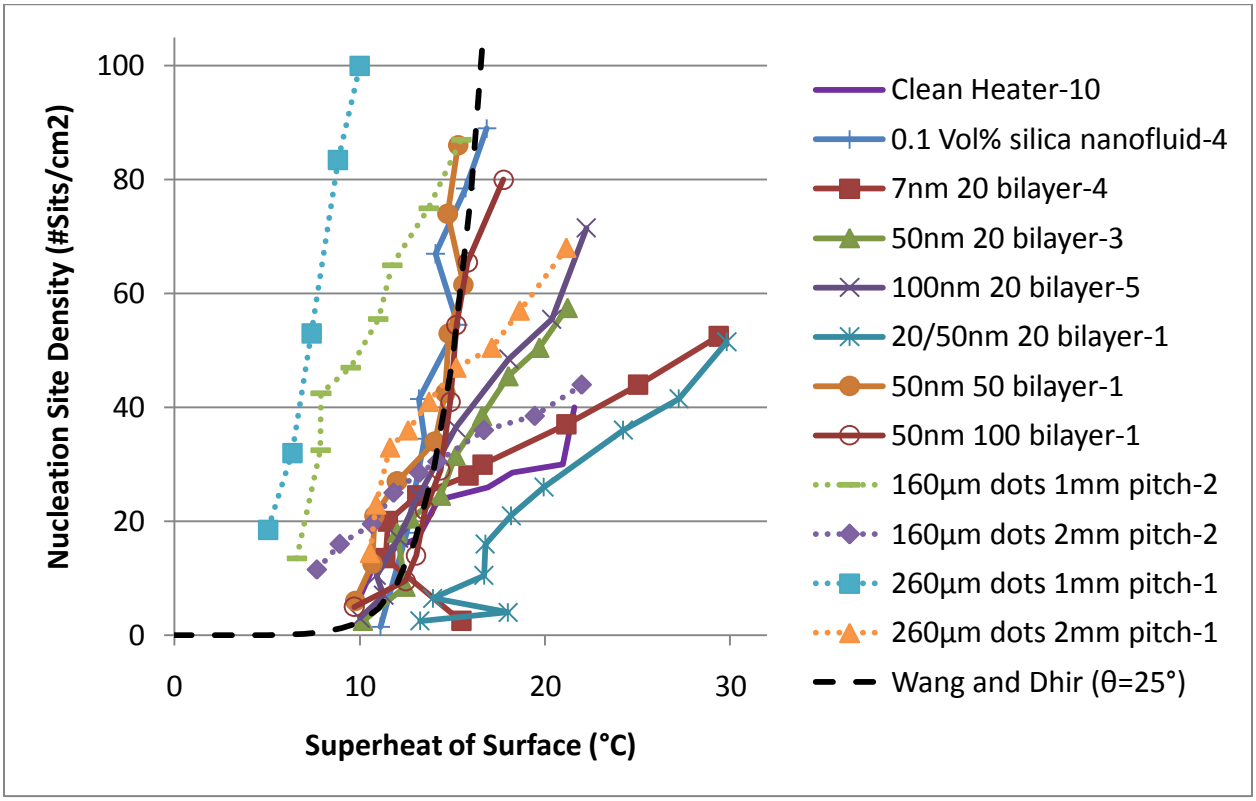

Figure 6-15: Nucleation site density plotted vs. wall superheat for characteristic tests for each surface of interest.

The nucleation site density correlation by Wang and Dhir follows the trend for the coatings which have near a 25° contact angle (50nm and 100nm particle coatings). The surfaces that were patterned on a 2mm pitch have similar to lower nucleation site densities compared to that of the

underlying coating of 50nm 50 bilayers. However, both of the 1mm pitch surfaces have nucleation site densities that are higher than for the underlying coating.

The 7nm 20 bilayer coating and the 20/50nm 20 bilayer coating had significantly lower nucleation site densities for a given superheat than for the other samples. This is an expected result based on the contact angle being very low for these coatings, and thus requiring a larger superheat to achieve bubble nucleation (this phenomenon is discussed in section 2.1).

The 2mm pitch pattern places approximately 70 hydrophobic "islands" on the active heater area, which is equivalent to a nucleation site density of 35 sites/cm^2. This value is less than the nucleation site density of the underlying coating for higher superheats. During the nucleation site counting process it was also observed that for the 2mm pitch cases, there was significant nucleation off of the pattern because the departure diameter of the bubbles was significantly less than the pitch of the pattern, and thus temperatures on the heater surface between the hydrophobic sites would reach a sufficient temperature to nucleate.

The 1mm pitch pattern places approximately 280 hydrophobic "islands" on the heater surface, which is equivalent to a nucleation site density of 140 sites/cm^2. This value is higher than any of the nucleation site densities for the heat fluxes where nucleation site density was counted. Both of these 1mm pitch patterned surfaces, had higher nucleation site densities for a given superheat than for any of the unpatterned surfaces.

6.6 Patterned Surface Expected Results vs. Observed Results

The purpose of patterning the surface was to attempt to increase the heat transfer coefficient of the boiling surface by controlling specific nucleation sites. These were spaced apart by spacing close to the bubble departure diameter for water at atmospheric pressure.

Ideally this would have allowed for a higher heat transfer coefficient because nucleation would be evenly spaced over the surface, while still maintaining a high CHF since bubble interaction would be minimized.

The nucleation events did follow the pattern of the hydrophobic islands that were placed on the surface. However, the heat transfer coefficient was not significantly altered. The nucleation site density was higher than for the surfaces with hydrophobic islands on a 1mm pitch, but the heat transfer coefficient was not significantly affected.

6.7 Future Work

Only two different pitches of the hydrophobic islands were tested of 1mm and 2mm. The 2mm pitch was further apart than what was necessary to fully control the boiling on the surface since there were bubble nucleations that occurred between the hydrophobic islands, and there were large spaces between the departing bubbles on this pattern. The 1mm pitch is close to the bubble departure diameter of water at atmospheric pressure, and the CHF is likely sensitive to the spacing of the hydrophobic islands near this pitch. Therefore, more experimentation with a test matrix of pitches near and below 1mm could potentially yield an enhanced heat transfer coefficient by packing bubbles together as close as possible, while still preventing bubble interaction and a premature CHF.

The locations of the hydrophobic islands in this testing were of the same morphology of the rest of the heater surface, only the chemistry in these regions were modified. Creating a surface where the hydrophobic regions were cavities could potentially improve control of the specific location of the nucleation. With the patterned surfaces used, the hydrophobic regions were as large as 180μm, by creating specific cavities on the surface, the location of the nucleation could

potentially be more precisely controlled, and yield more closely packed bubbles that do not interact.

All of the coatings tested were silica nanoparticles that were near spherical. Different nanoparticle materials and geometries (such as ellipsoids, rods, etc.) could be tested in conjunction with the patterned surfaces to see the effects on CHF and the heat transfer coefficient.

7 Conclusions

A heater was designed for use with a high speed IR camera that would provide a clean surface for boiling throughout the boiling process. Layer-by-layer deposition of silica nanoparticles was used to create boiling surfaces with increased roughness, porosity, and wettability to enhance CHF and the heat transfer coefficient. The effect of parameters such as nanoparticle size and the number of bilayers was explored. The wettability on the surface was further modified by patterning the surface with various "islands" of hydrophobicity to promote bubble nucleation at specific sites, while maintaining a hydrophilic "sea" to maximize the rewetting of the surface to improve CHF. These techniques provide better control of the surface than from boiling nanofluids where the deposition is random, and the characteristics of the nanoparticle coating are nearly impossible to control.

The basic findings of this work are below:

- The heater design chosen for this work provided a very clean surface that would not be fouled during the boiling process, and thus maintain the surface characteristics. However, the heater produced degraded IR images that made nucleation site density impossible to measure at high heat fluxes.
- The particle size has a significant effect on CHF for LbL coatings even though the wettability and surface roughness may not appreciably change. This is presumably from the pore size created by the different particles.
- The bilayer thickness has the effect of increasing CHF as the bilayer thickness increases until the effect saturates, and the thermal resistance of the coating begins to degrade the heat transfer coefficient.

- The CHF can be increased by over 105% by using hydrophilic LbL coatings and selecting the appropriate particle size, and bilayer thickness. This enhancement is as good if not superior to what was found from coating a surface by boiling in a nanofluid.
- The heat transfer coefficient can also be increased by over 100% by selecting the appropriate bilayer characteristics.
- Hydrophobic smooth surfaces hit a CHF at a very low heat flux (~50kW/m^2) due to the inability of the surface to rewet as can be seen through IR imaging. This gives credence to the hot spot CHF theory.
- Patterned boiling can be achieved on a surface by creating selective "islands" of hydrophobicity in a "sea" of hydrophilicity. These patterned surfaces show larger ranges of CHF and heat transfer coefficients, but may have potential to increase the heat transfer coefficient even more by properly tuning the distance between the hydrophobic islands. Based on the results gathered, even though there was a wide scatter in the data some cases had a superior heat transfer coefficient and CHF compared to the underlying nanoparticle coating.
- Patterning the surface with hydrophobic islands can increase the nucleation site density of a surface for a given superheat. There is the potential to increase the heat transfer coefficient with increased nucleation site density. Although, the results for the patterned surfaces tested here were mixed with both enhancement and degradation of the heat transfer coefficient compared to the underlying coating.

8 References

1. Collier, J.G. and J.R. Thome. *Convective Boiling and Condensation, Third Ed.* Oxford University Press, 1994.

2. Kim, S.J., I.C. Bang, J. Buongiorno, L.W. Hu. "Surface wettability change during pool boiling of nanofluids and its effect on critical heat flux." *Int J. Heat and Mass Transfer*, 50 (2007): 4105-4116.

3. Carey, V. *Liquid-Vapor Phase-Change Phenomena, Second Ed.*, Taylor & Francis, 2008.

4. Todreas, N.E., Mujid S. Kazimi. *Nuclear Systems I: Thermal Hydraulic Fundamentals*, Taylor & Francis 1993.

5. Novak, B.R., E.J. Maginn, M.J. McCready. "An Atomistic Simulation Study of the Role of Asperities and Indentations on Heterogeneous Bubble Nucleation." *Journal of Heat Transfer*, 130 (April 2008).

6. Incropera, Frank P., David P. Dewitt, Theodore L. Bergman, and Adrienne S. Lavine. *Fundamentals of Heat and Mass Transfer. 6th ed.* United States: John Wiley & Sons, 2007.

7. Theofanous, T.G., T.N. Dinh, J.P. Tu, A.T. Dinh. "The Boiling Crisis Phenomenon Part II: Dryout Dynamics and Burnout." *Experimental Thermal and Fluid Science*, 26: 793-810.

8. Ahn, H.S., V. Sathyamurthi, N. Sinha, S. Lau and D. Bannerjee. "Boiling Experiments on Vertically Aligned Carbon Nanotubes and Using Surface Micromachined Thin Film Thermocouple (TFT)." 9th AIAA/ASME Joint Thermophysics and Heat Transfer Conference. 8 June 2006. San Francisco, California.

9. Ahn, H.S., V. Sathyamurthi, and D. Banerjee. "Pool Boiling Experiments on a Nano-Structured Surface." *IEEE Transactions on Components and Packaging Technologies*, 32 (1), March 2009.

10. Chen, R., M. Lu, V. Srinivasan, Z. Wang, H. Cho, and A. Majumdar. "Nanowires for Enhanced Boiling Heat Transfer." *Nano Letters*, 9 (2009): 548-553.

11. Ujereh, S., I. Mudawar, T. Fisher. "Effects of Carbon Nanotube Arrays on Nucleate Pool Boiling." *Int. J. Heat Mass Transfer*, 50 (2007): 4023-4038.

12. Furberg, R., B. Palm, S. Li, M. Muhammed, and M. Torprak, "Porous Layer." World Intellectual Property Organization, WO 2007/100297 A1, 7 September 2007.

13. Vemuri, S., K.J. Kim. "Pool boiling of saturated FC-72 on nano-porous surface." *International Communications in Heat and Mass Transfer*, 32 (2005): 27-31.

14. Kunugi, T., K. Muko and M. Shibahara. "Ultrahigh Heat Transfer Enhancement Using Nano-porous Layer." *Superlattices and Microstructures*, 35 (2004): 531-542.

15. You, S.M., J.P. O'Connor, "Boiling Enhancement Coating." United States Patent, 29 Sep 1998.

16. O'Conner, J.P. , S.M. You, "A Painting Technique to Enhance Pool Boiling Heat Transfer in Saturated FC-72." *ASME Journal of Heat Transfer*, 117 (2) (1995): 387.

17. Nam, Y., Y. S. Ju. "Bubble nucleation on hydrophobic islands provides evidence to anomalously high contact angles of nanobubbles." *Applied Physics Letters* 93, (2008):103115.

18. Kim, S., et al. "Experimental Investigation of Critical Heat Flux Enhancement by Micro/Nanoscale Surface Modification in Pool Boiling." Paper 62289, Proc. Sixth International ASME Conference on Nanochannels, Microchannels and Minichannels (ICNMM2008). June 23-25, 2008 Damstadt, Germany.

19. Iler, R.K. "Multilayers of Colloidal Particles." *Journal of Colloid and Interface Science*, 21 (1966): 569-594.

20. Lee, Daeyeon, Damali Omolade, Robert E. Cohen, and Michael F. Rubner. "pH-Dependent Structure and Properties of TiO2/SiO2 Nanoparticle Multilayer Thin Films." *Chemical Materials*, American Chemical Society, 19 (2007): 1427-1433.

21. Lee, Daeyeon, Michael F. Rubner, and Robert E. Cohen. "All-Nanoparticle Thin-Film Coatings." *Nano Letters*, American Chemical Society, 6.10 (2006): 2305-2312.

22. Lee, Daeyeon, Zekeriyya Gemici, Michael F. Rubner, and Robert E. Cohen. "Multilayers of Oppositely Charged SiO2 Nanoparticles: Effect of Surface Charge on Multilayer Assembly." *Langmuir*, 23 (2007): 8833-8837.

23. Cebeci, Fevzi Ç., Zhizhong Wu, Lei Zhai, Robert E. Cohen, and Michael F. Rubner. "Nanoporosity-Driven Superhydrophilicity: a Means to Create Multifunctional Antifogging Coatings." *Langmuir*, 22 (2006): 2856-2862.

24. Forrest, E., E. Williamson, J. Buongiorno, L.W. Hu, M. Rubner, R. Cohen, "Augmentation of Nucleate Boiling Heat Transfer and Critical Heat Flux Using Nanoparticle Thin-Film Coatings", *International Journal of Heat and Mass Transfer*, 53 (2010): 58-67.

25. Bravo, J. , L. Zhai, Z. Wu, R. Cohen, M. Rubner. "Transparent Superhydrophobic Films Based on Silica Nanoparticles." *Langmuir*, 23 (13) (2007): 7293-7298.

26. Baunack, S. and A. Zehe. "A Study UV/Ozone Cleaning Procedure for Siilicon Surfaces." *Phys. sat sol.*, 115 (1989): 223-227.

27. Efimenko, Kirill, William E. Wallace, and Jan Genzer. "Surface Modification of Sylgard-184 Poly(dimethyl siloxane) Networks by Ultraviolet and Ultraviolet/Ozone Treatment." *Journal of Colloid and Interface Science*, 254 (2002): 306-315.

28. Jelight Company. "UVO Cleaner - Ozone Cleaning Device, " (2009) [Online] Available: http://www.jelight.com/uvo-ozone-cleaning.php, Accessed: 12 December 2010.

29. Osten, H.J., G. Lippert. "In situe cleaning of Si surfaces by UV/ozone." *Journal of Crystal Growth*, 127 (1993): 476-478.

30. Sun, Yugang, Won Mook Choi, Hanqing Jiang, Yonggang Y Huang, and John A. Rogers. "Controlled buckling of semiconductor nanoribbons for stretchable electronics." *Nature Nanotechnology*, 1 (December 2006): 202-207.

31. Childs, William R., Michael J. Motala, Keon Jae Lee, and Ralph G. Nuzzo. "Masterless Soft Lithography: Patterning UV/Ozone-Induced Adhesion on Poly(dimethylsiloxane) Surfaces." *Langmuir*, 21 (2005): 10096-10105.

32. Han, Joong Tark, Sangcheol Kim, and Alamgir Karim. "UVO-Tunable Superhydrophobic to Superhydrophilic Wetting Transition on Biomimetic Nanostructured Surfaces." *Langmuir*, 23 (2007): 2608-2614.

33. Nanofilm. "Nanofilm - Our Products." Nanofilm Microcircuit Technology. [Online] Available: http://www.nanofilm.com/global/pdf/substrate-material.pdf, Accessed: April 1, 2010.

34. Gerardi, C. "Investigation of the Pool Boiling Heat Transfer Enhancement of Nano-Engineered Fluids by means of High-Speed Infrared Thermography." PhD Thesis, Department of Nuclear Science and Engineering, Massachusetts Institute of Technology, 2009.

35. Chemical Rubber Company. *Handbook of Chemistry and Physics* 41st Ed., 1959.

36. ASM International. *Metals Handbook, Vol.2* - Properties and Selection: Nonferrous Alloys and Special-Purpose Materials, 10th Ed. 1990.

37. Pollack, J.B. and W.M Irvine. "Infrared optical properties of water and Ice spheres." *ICARUS*, 8 (1968): 324-360.

38. Coursey, J.S. and J. Kim. "Nanofluid boiling: The effect of surface wettability." *Int. J. Heat Fluid Flow*, 29 (December 2008): 1577-1585.

39. Moreno, G. Jr., S. Oldenburg, S. M. You, and J. H. Kim. "Pool Boiling Heat Transfer of Alumina-Water, Zinc Oxide-Water and Alumina-Water Ethylene Glycol Nanofluids." Proceedings of HT2005, July 17-22 2005. San Francisco, CA.

40. Arik, M., A. Bar-Cohen. "Effusivity-based correlation of surface property effects in pool boiling CHF of dielectric liquids." *Int. J. Heat Mass Transfer*, 46 (2003): 3755–3764.

41. Omega. "Revised Thermocouple Reference Tables." [Online], Available: http://www.omega.com/temperature/Z/pdf/z218-220.pdf, Accessed: 12/31/2010.

42. FLIR Systems. ThermoVision(R) SC4000/SC6000 User's Guide, Version 200. September 26, 2007.

43. Almaz Optics. "Sapphire, Al2O3." [Online] Available: http://www.almazoptics.com/sapphire.htm, Accessed: 12/31/10.

44. Tsoulfanidis, Nicholas. *Measurement and Detection of Radiation 2nd Ed.* Taylor & Francis 1995.

45. Peirce, B. “Criterion for the Rejection of Doubtful Observations.” *The Astronomical Journal*, No. 45, Vol. 2 (1852): 161-163.

46. Ross, S.M. “Peirce’s Criterion for the Elimination of Suspect Experimental Data.” *Journal of Engineering Technology* (Fall 2003).

47. Tompkins, H.G. and E.A. Irene, Eds. *Hanbook of Ellipsometry*. William Andrew Publishing, 2005. p.569.

48. Kaviany, M. *Principles of Heat Transfer in Porous Media, 2nd Ed.* Springer, 1995. p.144.

49. Haramura, Y., Y. Katto. “A New Hydrodynamic Model of CHF Applicable Widely to Both Pool and Forced Convection Boiling on Submerged Bodies in Saturated Liquids.” *International Journal of Heat and Mass Transfer*, 26 (1983) 389-399.

50. Sadasivan, P., P.R. Chappidi, C. Unal, R.A. Nelson. “Possible Mechanisms of Macrolayer Formation.” *Pool and External Flow Boiling*, ASME (1992): 135.

51. Theofanous, T.G., T.N. Dinh. “High Heat Flux Boiling and Burnout as Microphysical Phenomena: Mounting Evidence and Opportunities.” *Multiphase Science and Technology*, 18 (2006): 1-26.

52. Wang, C.H., V.K. Dhir. “Effect of surface wettability on active nucleation site density during pool boiling of water on a vertical surface.” *ASME Journal of Heat Transfer*, 115 (1993) 659-669.

53. Gemici, Zekeriyya, Hiroomi Shimomura, Robert E. Cohen, and Michael F. Rubner. "Hydrothermal Treatment of Nanoparticle Thin Films for Enhanced Mechanical Durability." *Langmuir*, 24 (5) (2008): 2168-2177.

54. Gerardi, C., J. Buongiorno, L. W. Hu, T. McKrell. "Experimental Observation of the Dynamic macro- and micro- layer during pool boiling." Proceedings of HTFESN, 2008.

55. Wang, C.H., V.K. Dhir. “On the gas entrapment and nucleation site density during pool boiling of saturated water.” *ASME Journal of Heat Transfer*, 115 (1993): 670-679.

56. Kocamustafaogullari, G., M. Ishii. “Interfacial area and nucleation site density in boiling systems.” *Int. J. Heat Mass Transfer* 26 (1983):1377–1387.